Analysis of Electrical and Thermal Stresses in the Stress Relief System of Inverter Fed Medium Voltage Induction Motors

by

Emad Sharifi-Ghazvini

A thesis
presented to the University of Waterloo
in fulfillment of the
thesis requirement for the degree of
Doctor of Philosophy
in
Electrical and Computer Engineering

Waterloo, Ontario, Canada, 2010

AUTHOR'S DECLARATION

I hereby declare that I am the sole author of this thesis. This is a true copy of the thesis, including any required final revisions, as accepted by my examiners.

I understand that my thesis may be made electronically available to the public.

Abstract

Pulse width modulation (PWM) voltage source converters (VSC) are one type of motor drives that have become popular because they enable precise control of speed and torque in medium voltage motors. However, these drives are known to have adverse effects on the insulation system particularly on conductive armour tape (CAT) and semi-conductive stress grading tape (SGT). These tapes, which are crucial components of the insulation system, control the surface electrical stresses in the stator slot and in the end portion of the form-wound coils outside the grounded stator. The material properties of CAT and SGT and the methods by which they are applied on form-wound motor coils are traditionally designed for power frequency, or a 60 Hz sinusoidal voltage. However, because of the high frequencies associated with the repetition rate and the fast rise time of the PWM pulses, elevated electrical and thermal stresses develop in these tapes, which can lead to premature insulation failure. Little research has been conducted with respect to understanding the mechanism of dielectric heating as a function of frequency and repetitive pulse characteristics.

The material characterization of CAT and SGT is a vital part of an investigation of the performance of the stress relief system at high frequencies. In this study, the anisotropic dielectric properties of CAT and SGT have been measured in dc and ac and in low and high electric fields. The laboratory experiments for determining the material characteristics are discussed and the results analyzed.

According to the ac space charge limited field (SCLF) theory, the maximum ac tangential component of the electric field in a nonlinear resistive SGT on medium voltage form-wound motor coils can be predicted from the field dependent electrical conductivity and the frequency. However, the SCLF theory cannot predict the total electric field (vector sum of the tangential and normal components) in the air adjacent to the surface of the tapes. Simulations of the electric field using a finite element method (FEM), is one of the best ways of finding the resultant electric field distribution in the air space adjacent to the SGT. However, prior to this study, researchers simplified the modelling of the stress relief system to avoid the convergence problems that develop due to the nonlinearity of the SGT conductivity as a function of the electric field, and also because of the geometry and dimensions of the tapes when their depths are orders of magnitude smaller than the other dimensions associated with form-wound coils. For modelling the stress grading (SG) system at power frequency and at the rated voltage, the dc isotropic conductivity of the SGT and CAT has also been extensively investigated. However, relatively

little work has been done with respect to the ac electrical behaviour of these materials and dc modelling cannot reflect the effects of high-frequency stresses on the machine insulation.

In this study, comprehensive transient FEM modelling has been developed in order to simulate the insulation system with nonlinear field dependent materials. The actual dimensions of the components are applied in the model, and the appropriate material parameters for the FEM simulations are extracted from the experimental test results. One crucial point that has not been considered in previous studies is the effect of the component of the electric field that is normal to the surface of the coil. In most studies, only the tangential component of the electric field is considered; however, in this study, both components and the resultant electric field are computed.

The surface tangential field is calculated with reference to the gradient of the surface potential as measured with an electrostatic voltmeter. It is shown that this technique can provide a reasonable estimate for the tangential field along the SG system, but not without limitations, which are discussed in detail.

Based on laboratory work and analytical analysis, this research has successfully determined the relationship between the thermal effect of the PWM voltage and the other repetitive fast pulses, such as square wave and impulse voltages. The influence of the pulse characteristics on the development of stresses has also thoroughly investigated, and the results are presented.

A coupled electric and thermal model that incorporates the finite element method (FEM) is used as a means of studying thermal stresses and determining appropriate remedies. However, using transient analysis as an approach for finding the temperature profile associated with high repetitive impulses (1-10 kHz) and fast rise times (~200 ns) is both difficult and impractical. According to these considerations, an alternative method has been developed from stationary analyses based on two sinusoidal voltages of different frequencies. The frequency and amplitude of these sinusoids are measured relative to the switching frequency, signal power, and nonlinearity of the system, and the results of the simulation are then verified experimentally, thus showing the efficacy of this method.

This research also concluded that a capacitive SG system with conductive foil embedded in the groundwall insulation can be a practical alternative to a conventional SGT of form-wound coils in inverter fed motors. The performance of the capacitive SG scheme is independent of frequency and can therefore provide the required mitigation of the stress caused by repetitive fast pulses. The results of the evaluation of this system with respect to qualification tests demonstrate the effectiveness of the system.

Acknowledgements

First and foremost, I wish to thank my supervisors, Dr. Shesha Jayaram and Dr. Edward Cherney for their assistance, support, and guidance throughout the duration of this work. I also wish to express my appreciation to my PhD Committee (Dr. Richard Culham, Dr. Gian Carlo Montanari, Dr. Omar Ramahi, Dr. Siva Sivoththaman, and my supervisors) for their valuable suggestions and constructive comments.

I would like to thank my friends in the high voltage engineering laboratory at the University of Waterloo: Ahmed, Alex, Ali, Ayman, Chitral, Isaias, Michael, Omar, Rafat, Rina, Saeed, Saleh, Sarajit, Susan, and Utkarsh, made it a convivial place to work. In particular, I would like to say a special thank you to Chitral not only for being a valuable friend and roommate, but also for his patience and dignity.

I am grateful to my dear friend Rasoul Keshavarzi for his kind attention and for helping me settle in when I arrived in Canada.

My thanks go to Dave Messervey, Ramtin Omranipour, and Saeed Ul Haq from GE Peterborough for providing test samples and for their valuable comments during this work.

I also acknowledge all my friends and colleagues in the electric machine group and power system research centre at the Niroo Research Institute (NRI) in Iran for the professional opportunity and valuable experience that enabled me to complete my PhD program.

My deepest gratitude goes to all the members of my family and to my friends, for the wonderful support they all provided.

The financial support provided by NSERC of Canada and the Fellowship from the IEEE-DEIS Society are also greatly appreciated.

Last but not least, I would like to thank Mrs. Barbara Trotter for proofreading this thesis.

To my lovely son Mahan

To my dear wife, parents, sister, and brothers

.

Table of Contents

List of Tables

List of Figures

Chapter 1
Introduction

1.1 Introduction

Highly efficient motor drive systems are fast becoming a standard in industrial applications, because of today's impending global climate crisis. Variable speed and torque ac drives are used in ever increasing numbers because of their well known benefits: energy efficiency and flexible control of processes and machinery using low cost readily available maintenance free ac induction motors. In western industrialized countries such as Canada, over 50 % of the electrical energy produced is utilized by electric motors and more than 90 % of these motors are induction motors [1].

As voltage source converters (VSC), modern solid state motor drives are based on a pulse width modulation (PWM) technique in order to produce variable frequency and amplitude ac voltage. For medium voltage (MV) motors, the industry is also focusing on devising drives that have faster switching devices in order to reduce switching losses. The application of this type of drive for motor speed and torque control provides significantly greater benefit than the former techniques; however, from the outset, many kinds of motor failures and motor side challenges have been reported. The main disadvantage of these fast drives is their adverse effect on the machine insulation system. In PWM-VSC drive applications, fast switching produces complex transients that severely stress the motor insulation, which is designed to operate at 50 or 60 Hz.

A MV insulation system is, in fact, a complex and multi-dielectric system. Due to the transition between the high voltage and the ground potential at the interface of the insulation, the grounded stator body, and the air, the surface stress relief system plays a crucial role in the reliability of the machine insulation system. Conventional surface electrical stress relief control includes a slot conductive armour coating and an endwinding nonlinear resistive stress grading (SG) system, which are susceptible to fast degradation under repetitive fast pulses. Any malfunction in the SG system eventually leads to the breakdown of the main insulation and a forced machine outage.

Developing electrical and thermal stress is generally manifested by surface discharges in the vicinity or hot spots in the SG system and/or in the slot conductive armour coating. These problems are found crucially in a resistive SG system because they are greatly affected by high dV/dt and switching frequency associated with PWM-VSC.

The mechanism that causes these problems is not totally understood. Analyzing the root causes and finding effective remedies require a determination of properties of the materials and their behaviour at high electric field, high temperatures, and at high frequencies and repetitive pulses. In addition, a powerful computer simulation software tool for modelling and analyzing a system that is similar to actual conditions is considered vital. Other methods of mitigating the stresses associated with PWM-VSC must also be evaluated for their feasibility as alternatives to the conventional system.

The following sections present a detailed explanation of the stress relief system, in particular the SG system. Details are also provided with respect to the specifications and the conduction mechanism of common semiconductive SG materials. The effect of PWM-VSC on the SG system and methods of modelling the system are also discussed, followed by a comprehensive literature survey.

1.2 Medium Voltage Induction Motors and Form Wound Coils

Induction motors are widely used because they are rugged, reliable, easy to manufacture and maintain, and relatively inexpensive. As well their power density ratio (output power to weight) is significantly greater than that of dc motors. They include both single- and poly-phase designs developed to operate from less than one to several thousands of horsepower [2, 3].

MV induction motors have a rated voltage from just above 700 volts up to and including 13,800 volts. These motors are used in heavy industry for applications such as pumps, compressors, mixers, grinders, crushers and cranes. The current carrying conductors or wires on motors rated less than 700 volts are randomly wound in the slots of the stator: the stationary part of a motor. The insulation on these conductors is referred to as Type I as defined by IEC 60034-18-42 [4]. On motors rated above 700 volts, the windings are made from insulated form wound coils that have been preformed and are then inserted into the slots of the motor stator during its manufacture. A form wound coil consists of a continuous loop of strands into a coil, with additional insulation applied over the coil loops. Machines that contain form wound coils work at a higher rated voltage and, because they may experience partial discharge (PD) within their lifetime, are defined as Type II as opposed to Type I, which denotes random wound coils [4, 5].

Conventional Type II insulation systems have the following basic insulation components: strand insulation, turn insulation, and groundwall (main insulation). For electric motors with voltage ratings above 6 kV, a conductive armour coating (in the form of paint or tape), and an endwinding stress grading system are also used in order to protect the groundwall insulation from

high electrical stresses. A configuration of form wound coils with Type II insulation in the stator slots is illustrated in Figure 1-1.

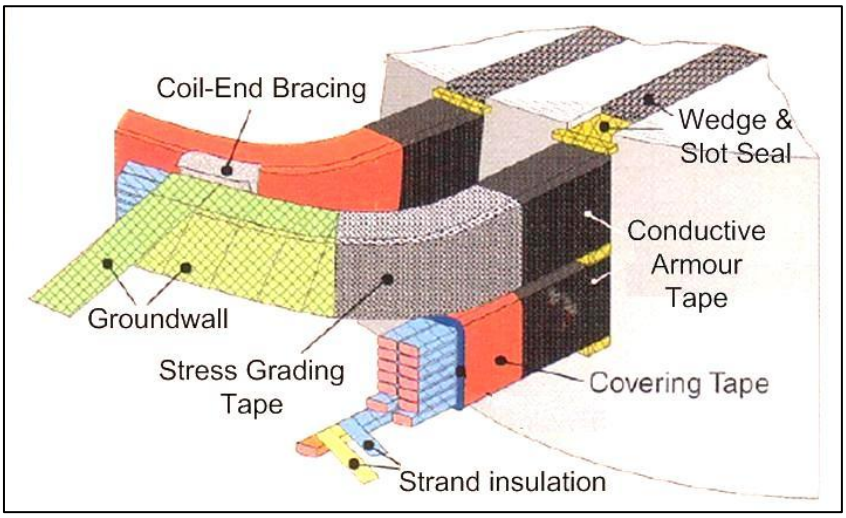

Figure 1-1: Configuration of form wound coils with a Type II insulation system in the stator slots.

To facilitate forming and manufacturing and to reduce the Joule loss due to the skin effect and eddy current, the form wound coils are made from strands or magnet wires, which must be insulated from one another. These wires are coated with either enamel or a polymer film with filler, such as alumina, to protect from partial discharge (PD) [5]. The turn insulation can be separately wrapped resin rich mica tape insulation to prevent shorts between the turns in multi-turn form wound coils. However, this step can be eliminated if the strand insulation is upgraded to individual strands machine taped with a thin mica flake tape, supported with a polyethylene terephthalate (PET) or amide polymer film [6, 7].

Groundwall insulation is the main component of an insulation system that isolates the copper conductors from the grounded stator core. Any failure of the groundwall insulation usually triggers a ground fault relay that takes the motor offline. Thus, the stator groundwall is extremely important for the reliable operation and long service life of a motor, and it must therefore be able to withstand the rigours of the electrical, thermal, and mechanical stresses that it is subjected to [5]. Electrical solid insulation systems are classified into 9 groups; however 5 common modern electrical insulation thermal classes are: Class A (105 ˚C); Class B (130 ˚C); Class F (155 ˚C); Class H (180 ˚C); and class N (200 ˚C) [8, 9]. Class F groundwall insulation, the common thermal class for form wound coils in the motor industry, consists of small mica flakes that are deposited onto a glass fibre backing tape. Once the tape has been wrapped around the conductors, the synthetic resin is cured at an elevated temperature and pressure. Two methods of dispersing and

curing the resins are used: resin rich technique or vacuum pressure impregnation (VPI). The VPI process provides much better void free impregnation than the resin rich technique [10] and it can be used in two ways. Either individual coils (individual VPI) can be made, or the coils can be placed into the stator in the dry or resin poor stage and then the entire stator can be VPI treated (global VPI). The latter process, or global treatment, has a significant advantage: the VPI resin locks the coils in the stator slot and fills the felt blocking materials and ropes in order to provide bracing for the endwindings [7].

1.3 Stress Relief Systems

To prevent PD on the surface of the stator coils, stress relief is a crucial insulation system component for form wound coils that operate at 6 kV or above [5]. As mentioned, to electrically isolate the copper conductors from the grounded stator core, groundwall insulation is applied to coils that are at a high voltage. However, due to the laminated core construction, the contact between the coil and the stator slot is not perfect. A conductive layer, referred to as the conductive armour, is applied to the groundwall insulation in order to avoid PD within the air space between the coil and the stator slot. Such PD can erode the groundwall insulation in the vicinity, leading to failure.

As a grounded screen, the conductive armour extends a few centimetres outside of the slot in order to minimize the stress over the end portions of the coils (overhang). However, it cannot end abruptly because discontinuity at the end of the screen can result in a high electric field along the surface of the insulation beyond the screen. This region, commonly referred to as the triple point, normally occurs at any interface where a grounded concentric screen, a solid insulation, and a gaseous (or liquid) insulation merge. When a voltage is applied between the conductor and ground, nearly all of the voltage drops between the conductor and the grounded screen, which results a high voltage gradient along the surface. If the localized stress at a triple point exceeds the breakdown strength of one of the media, normally the gaseous one, it gives rise to partial/surface discharges. These discharges can erode the groundwall insulation in MV motors and thereby shorten the life of the machine. To control the divergent field and avoid PD in this area, an SG system must be applied [5, 11, 12, 13, 14].

Using the finite element method (FEM), explained in section 2-5, to examine the electrical stress at the triple point of a form wound coil without SG, as illustrated in Figure 1-2, the local electric field is beyond the discharge threshold.

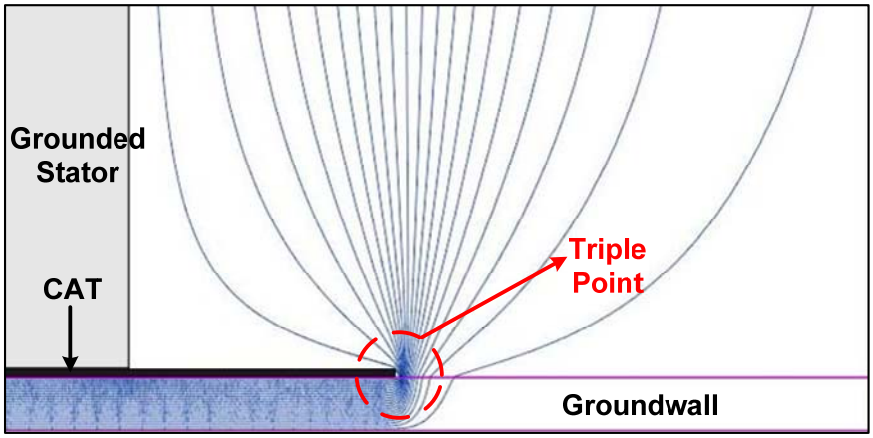

(a)

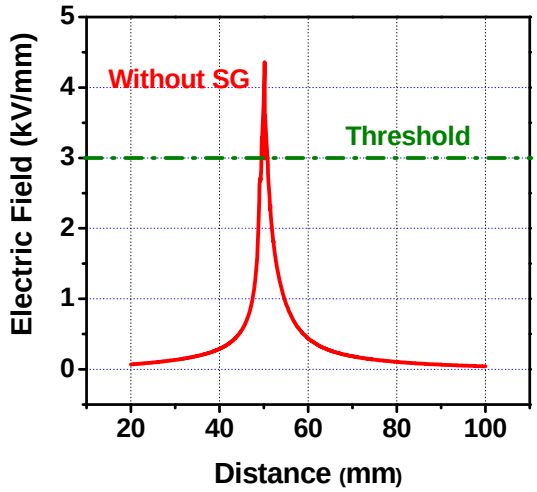

(b)

Figure 1-2: (a) Triple point and equipotential lines, and (b) electric field profile along the overhang of a typical form wound coil.

1.3.1 Conductive Armour

The conductive armour is commonly made of composite materials whose resistance is not field dependent, and combined with conductive fillers such as carbon black (CB) and/or graphitic carbon [12]. These fillers are added to a solvent base to form a conductive paint or to a polyester fleece or/and woven glass tape with a suitable binder to form a conductive tape [15]. The tape is preferred due to its durability and is referred to as conductive armour tape (CAT). The most popular materials currently used for CAT are polyester fleece (non-woven) impregnated with a graphite loaded resin binder, with a resistivity typically in the range of 200 to 3000 Ω/sq, which is low enough to form an equipotential surface on the groundwall within the slot but not so low as to short out the stator core laminations [15, 16, 17]. However, the disadvantage of polyester fleece is its lack of robustness with respect to the effects of oxidation from the products of electrical discharges [18].

New conductive tape based on Nomex® technology has recently been introduced. The tape has a thermal performance class of 220 ˚C and contains no binder resin. Instead, conductive particles are fixed in the non-woven structure of the Nomex® paper, which provide significant advantages [16].

1.3.2 Stress Grading Systems

SG systems for MV motors can be classified into two main methods: resistive and capacitive. Each method controls the localized stress to a level that is lower than the breakdown strength of the surrounding gaseous media, or of the air, in air cooled motors.

1.3.2.1 Resistive SG

To relieve the stress at the end of the CAT, at a short distance along the groundwall insulation, a nonlinear resistive SG tape (SGT) is commonly used in order to modify the surface impedance of the main insulation. This effect is normally achieved by using a composite filled with silicon carbide (SiC) or a zinc oxide-varistor material (ZnO-VM) that exhibits a voltage/electric field dependent resistivity. These composites are commonly percolated, thus establishing conductive paths through the insulating matrix. The polymeric matrix includes different options for the material, depending on how and where it will be applied. Varnishes, epoxy resins, polyester resins, and silicone rubber are some of the materials used in SG composites [14]. The typical current voltage characteristics of SiC and ZnO are depicted in Figure 1-3. As shown, ZnO has significantly distinctive nonlinearity compared to the SiC currently applied as SGT [19].

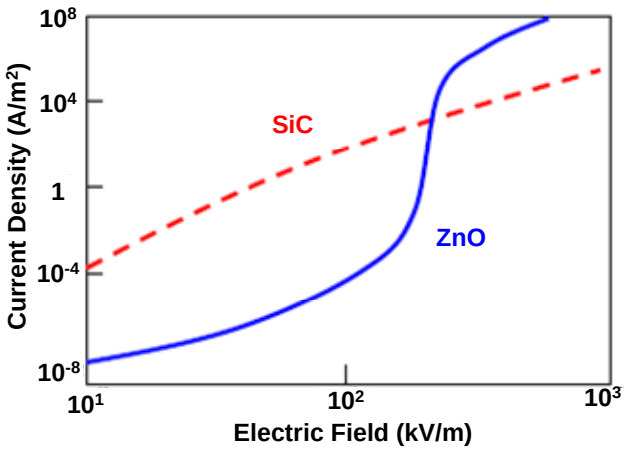

Figure 1-3: Typical current-voltage characteristics of composites filled with SiC and ZnO [19].

A nonlinear resistive field dependent SGT has the following advantages [14]:

- High electrical conductivity only in areas where the electric field is high
- Limiting field property for controlling the electric field during over-voltages

- Easy application on the coil
- Reproducibility

The effect of the nonlinear SG at 60 Hz on (a) the equipotentials and on (b) the potential and electric field profiles along the end portion of a 13.8 kV motor coil are illustrated in Figure 1-4.

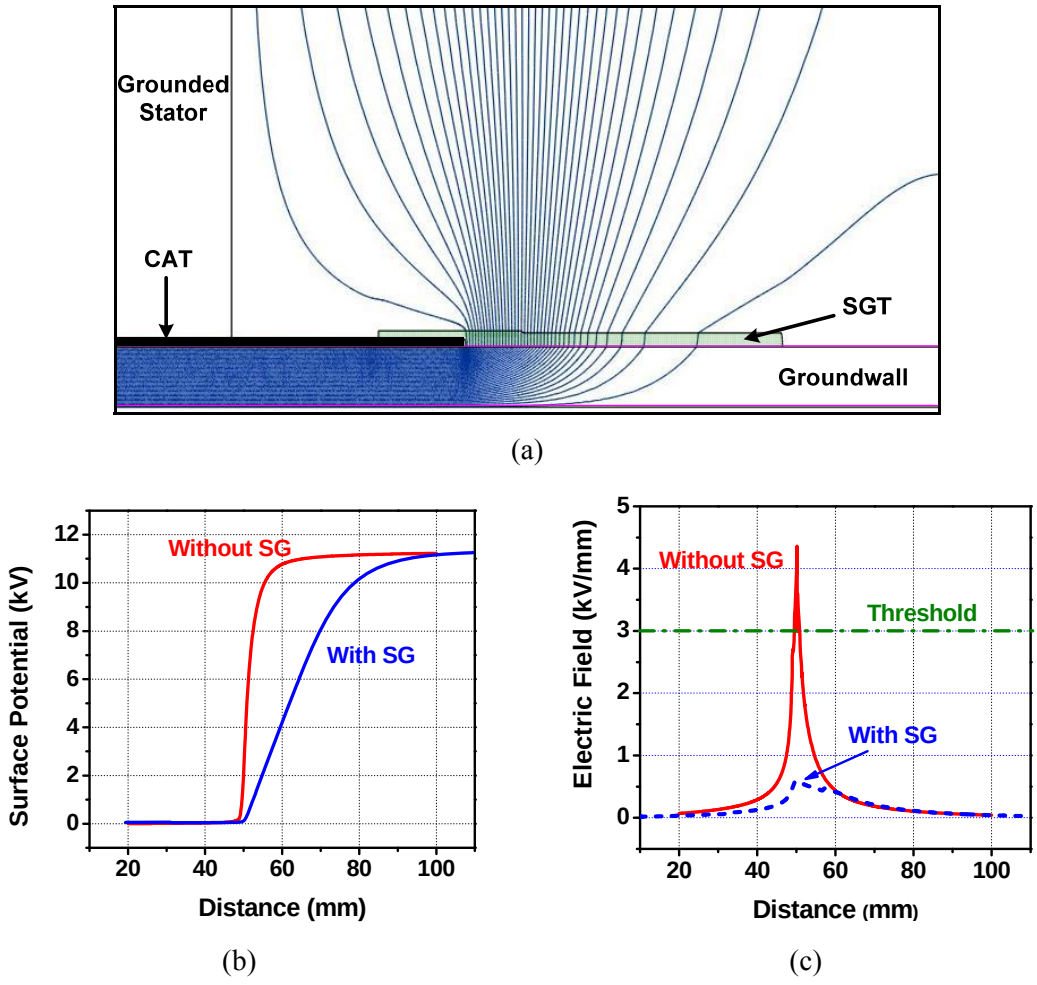

Figure 1-4: Effect of the nonlinear SG at 60 Hz on (a) the equipotential lines, (b) surface potential profile, and (c) electric field profile along the end portion of a 13.8 kV motor coil.

In spite of the advantages evident in Figure 1-4, SGT also has the following disadvantages:

- Under a high electric field, the SGT has high conductivity which results in high power loss and leads to increased surface temperature and a hot spot. As well, since the SGT loss represents the greatest proportion of the total insulation losses, the power factor and tip-up tests can no longer be used to accurately assess the condition of the groundwall insulation [20].
- The VPI processes for manufacturing the insulation system cause a significant change in the electrical and thermal characteristics of the SGT.

- For simplicity of modelling, it is assumed that the SGT is homogeneous and isotropic, which is far from reality. However, no comprehensive models exist for representing all of the characteristics of the materials and analyzing their response to different operational conditions such as repetitive fast pulse voltages and high temperatures [14, 21].
- The overlap of the SGT and the CAT may get damaged. If the SGT no longer has a connection to the ground and therefore floats; hence the voltage will then rise close to the level of the conductor voltage, giving rise to partial discharges [5].
- Because the dielectric SG material properties are nonlinearly dependent on electric field, temperature, and frequency, modelling of the SG system is not straightforward.
- Due to a high displacement current during the rising of the fast pulses/surges, the nonlinear resistive SGT may act capacitively and may not properly grade the electric field [22].

1.3.2.2 Capacitive SG

Electrical stress may be controlled by the application of a high permittivity layer of insulation in place of the conductive armour at the overhang or by capacitive grading using floating conductive foils inserted within the groundwall insulation. These two methods are discussed below.

- **High permittivity layer**

In this technique, widely used in power cable terminations, the cable end is prepared by removing the insulation shield, thus exposing the insulation. A sleeve of high permittivity material is slipped onto the end of the cable, replacing the insulation shield that has been removed and making electrical contact with the insulation shield. The electrical stress is controlled by dielectric refraction, which occurs because of the difference in the dielectric constants between the two materials. This effect is analogous to the refraction of light that results from the difference in the index of refraction of two media, normally air and glass. To achieve a large refraction of the equipotentials and therefore good stress control requires a material with a dielectric constant that is very large relative to that of the underlying insulation. Typically, a sleeve with a dielectric constant of 15 is used with cable insulation that has a dielectric constant of about 2.5. Material with a dielectric constant greater than about 15 is difficult to manufacture because above that value the loading of the filler into the sleeve material begins to affect the mechanical properties of the sleeve. For form-wound motor coils which have a dielectric constant of about 4.5, effective stress control necessitates a dielectric constant greater than 25 [11, 23].

- **Floating conductive screens**

This technique is widely used in HV bushings. A bushing is a device that insulates a high voltage conductor when it passes through a barrier or enclosure at ground potential. Figure 1.5 (a) shows

the construction of both a simple bushing and a capacitor bushing. The simple bushing has insulation formed onto the high voltage conductor, while the capacitor bushing is similar but has foils embedded within the insulation. Figure 1.5 (b) illustrates the equipotential profiles for both. It is evident that the foil arrangement distributes the equipotentials more uniformly over the length of the bushing, thereby grading the electrical stress along the surface of the bushing. The simple bushing is analogous to the form wound motor coil exiting from the stator slot without conductive armour and stress grading whereas the bushing with foils illustrates the effect of having floating foils inserted into the insulation [11, 23, 24].

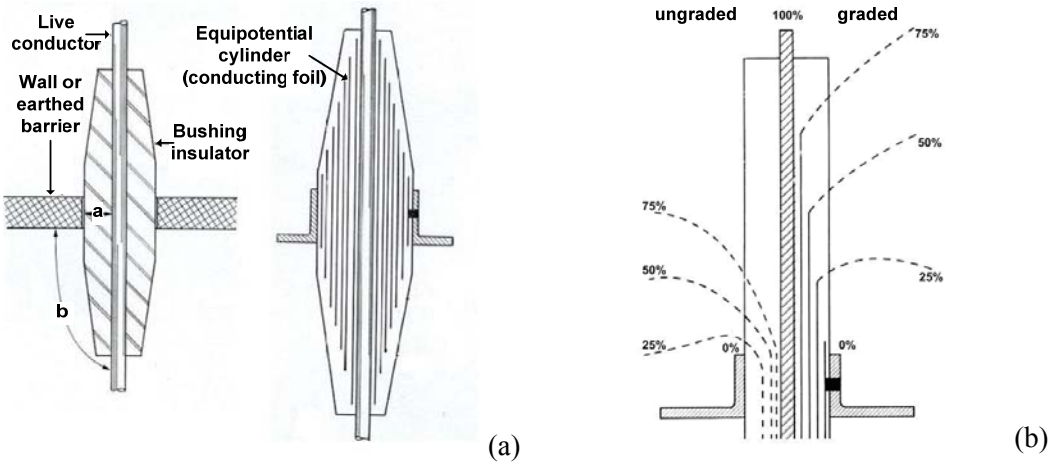

Figure 1-5: (a) Construction of a simple ungraded bushing and a capacitor foil bushing, (b) equipotential profiles for both [25].

Even today, no standard has been established for the design of stress relief systems, and even nonlinear conduction phenomena that occur in both high electric field and high temperature applications are still under scrutiny. Nevertheless, because of the adequate performance of nonlinear resistive SG for 50 or 60 Hz power frequency as well as the easy manufacturing process, most motor coil manufacturers prefer to apply this kind of SG system to conventional motor coils rather than to use capacitive stress grading techniques.

1.4 PWM Motor Drives and Their Effects on Stress Relief

The introduction of adjustable speed drives (ASDs) in 1983 revolutionized the operation and control of MV induction motors. Whether for retrofitting of installed motors or new motors, these solid state drives have replaced devices such as gearboxes and eddy current clutches that had been used for decades [26]. According to one survey, the use of MV drives as variable frequency converters has grown 20 % since 2003 and even today continues to increase rapidly [27]. A

general block diagram of motor drives based on variable frequency converters is shown in Figure 1-6.

The newer solid state drives provide obvious advantages over older methods of speed control. The most important advantages include increased reliability, reduced downtime, improved overall system efficiency, an improved power factor, soft starting and over speed capabilities, and improved process precision and product quality [26, 28].

Furthermore, the rapid development of technology and manufacturing in the electronics industry has resulted in the creation of semiconductor switches with ever increasing current and voltage ratings. These improvements have permitted the development of higher voltage solid state drives. Current solid state-based MV drives have operating voltages from 2.3 to 13.8 kV [29].

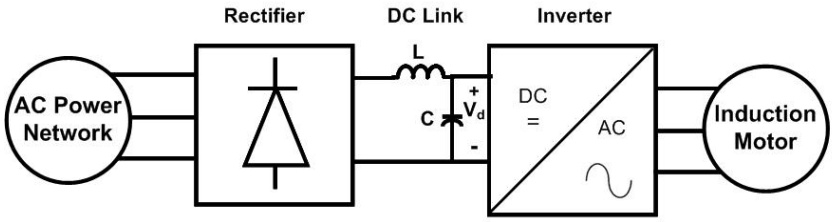

Figure 1-6: Block diagram of a motor drive, rectifier and inverter.

1.4.1 Classification of Variable Frequency Converter

Variable frequency converters for MV induction motors are classified as either voltage source (VSC) or current source (CSC) converters, depending on their mode of operation. In VSCs, the dc link is a dc voltage while in CSCs the dc link is a dc current [30].

For Industrial applications, VSCs are preferred over CSCs because of their many advantages which include better efficiency, faster transient response, lighter weight, lower price, and greater flexibility of operation with either closed loop or open-loop control, a feature that is not possible with CSCs [31, 32, 33, 34]. For both types of converter, a PWM technique is widely used for controlling the magnitude, phase, and frequency of the output voltage.

1.4.2 Sinusoidal Pulse Width Modulation Technique

To produce a sinusoidal output voltage waveform with a controllable magnitude and frequency, a sinusoidal control signal ($v_{control}$) set at the desired frequency (f_1, or the *modulating frequency*) is compared with a triangular waveform (v_{tri}) with frequency f_s , or the *carrier frequency.* As shown in Figure 1-7, the frequency of the fundamental component (V_{o1}) of the output voltage is the same

as the frequency of the control signal, the magnitude is linearly dependent on the dc link voltage (V_d) [35].

The PWM technique permits a higher quality of waveform with a higher switching frequency. PWM techniques can also be used with both bipolar and unipolar voltage switching. Figure 1-7 shows the bipolar and unipolar output voltage waveforms. Unipolar PWM voltage switching is a more popular choice for electric motors due to the better power quality it provides.

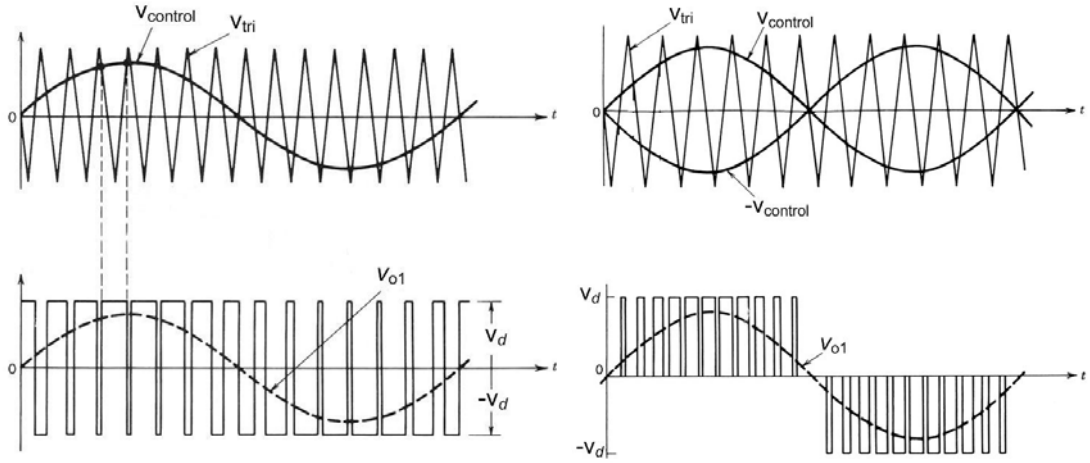

Figure 1-7: PWM voltage waveforms Left: Bipolar, Right: Unipolar [35]**.**

1.4.3 Problems with PWM-VSC Drives

Although the use of PWM-VSCs for motor speed control has far greater benefits than the former techniques, from the early stages of using these drives, a variety of motor failure as well as motor side challenges have been reported. These problems include premature insulation and mechanical (bearing) failure, electromagnetic interference, acoustic noise, and torsion vibration. The main disadvantage of these fast drives is the adverse effects on the insulation system due to the high frequency components of the PWM pulses, which lead to elevated electrical and thermal stresses and thus faster aging. Because the insulation systems of these motors were mostly designed in the same way as for operation at 50 or 60 Hz, the fast repetitive PWM pulses give rise to extra stresses and therefore reduced life [4, 6, 13, 36, 37, 38, 39, 40, 41].

The major problems associated with these drives come from their three inherent features: the fast rise time of the pulses (or high dV/dt), the pulse repetition frequency, and the overvoltage (overshoots). Figure 1-8 depicts an actual PWM-VSC pulse. [4, 37]

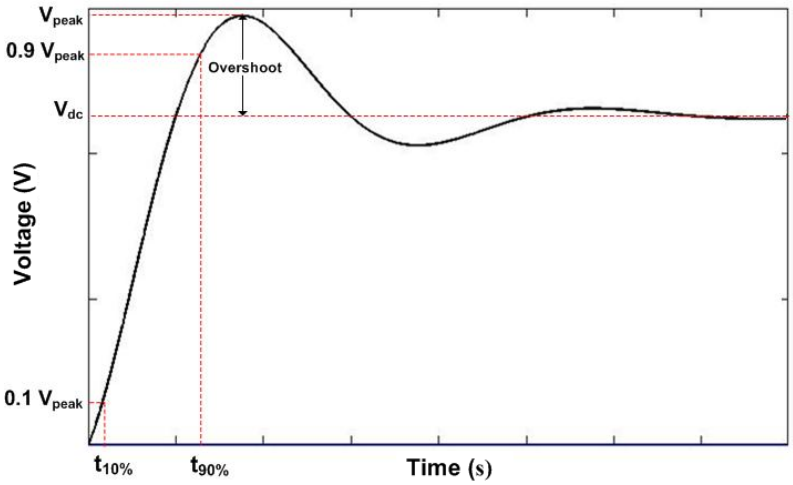

Figure 1-8: Typical single PWM pulse waveform (rise time= 1.25 × (t90% - t10%)) [4].

The dominant approach to developing these converters are to use faster switching devices such as insulated gate bipolar transistors (IGBT), and to increase the repetition frequency in order to enhance the efficiency and power quality. As discussed later in this chapter, both of these methods have adverse effects on the insulation system. In addition, because the PWM inverter and motor are commonly installed in different locations which creates impedance mismatch, the reflected waves at the interface between the feeding cable and the motor terminal create an overshoot that can reach 2 pu or more at the motor terminal, particularly for small motors (<50 hp). Motor surge impedance has a range of about 5000 to 30 Ω in motors from 0.1 hp to 1000 hp; the larger the motor, the smaller the surge impedance. However, it should be noted that for larger motors (> 50 hp) the motor surge impedance decreases significantly and the voltage reflection phenomenon may therefore not be as pronounced. Thus, with a cable surge impedance between 40 and 70 Ω, the reflected voltage decays as the hp increases, and an overvoltage approaching 2 pu often occurs with a small motor load. In other words, the smaller the motor, the larger the reflected voltage [4, 42, 43, 44]. Numerous methods have been developed with the goal of suppressing this transient overvoltage. One method is to use motor terminal filters and another is to use passive filters at the inverter side to decrease or control the rise time of the voltage pulses. These filters are imperfect, and their performance depends on the operating conditions, such as the length of the connecting cable. They normally slow down the rise time and the overshoot; however, have no effect on the repetition frequency of the fast pulses. In addition, these devices cause extra expense, weight, and space that are not viewed positively by users [44].

In general, the repetitive fast pulses of PWM-VSC drives add extra stresses on the insulation systems, which are indicated by Joule and dielectric heating, space charge accumulation, partial

discharge, and surface discharge activities, all of which lead to accelerated insulation degradation [45]. It has been shown that the life of polymeric electrical insulation is highly influenced by temperature [6]. Therefore, to enhance the lifetime of a motor under a power frequency, the maximum operating temperature is specified according to the thermal class of the insulation and motor operating conditions. However, for PWM-VSC fed motors, both the repetition frequency and the high frequency associated with the rise time of the leading edge of the PWM pulses create additional Joule and dielectric power losses in the insulation system, which manifest as hot spots in the CAT and the SGT. In addition, the magnitude of the voltage overshoot can influence the performance of both the CAT and the SGT by increasing surface discharge activity [4, 6, 36].

Therefore, although CAT and SGT work well at a power frequency, they exhibit poor performance in the presence of highly repetitive steep-front PWM pulses which can lead to early failure of the coatings. Since the lifetime of the main insulation of a motor depends significantly on the reliability of the stress relief system, these components of the insulation are therefore of great importance with respect to drive fed MV motor insulation. The high repetition rate of PWM pulses also has other negative effects on the groundwall, strand, and turn insulation that are outside the scope of this project [6].

1.5 Literature Review

This section contains review of previous studies and research with respect to the stress grading systems. Based on importance, the work is classified into four main categories: material properties, SG systems of MV motor coils energized by power frequency voltage and the coils fed by PWM-VSC, and the modelling and simulation of SG systems.

1.5.1 Material Properties

Due to the wide range for industrial applications for conductive and semiconductive composites, their conduction mechanisms and their dielectric properties have been the subject of numerous theoretical and experimental studies. Several theories have been proposed as explanation of the conduction mechanisms and the nature of the contacts between the clusters in a conductive or semiconductive composite [46].

Strumpler and Galtz-Reichenbach [47] discussed the conductivity of these polymer composites has a critical dependence on the content of the filler by volume, which vary from 10^{-13} S/m for low filler fractions to very high values for high loading of the filler. The conductivity of the filler itself can vary from 10^{7} S/m for metals such as Ni and 10 to 10^{3} S/m for intermediate conductive

materials such as carbon black and to about 10^{-8} S/m at low electric field for nonlinear fillers such as doped silicon carbide (SiC) or zinc oxide (ZnO). They also showed that the arrangement of the filler particles and the resulting conductivity can be described either by percolation or by effective medium theories. In filled composites four different conduction aspects must be taken into account: the conduction in the polymer matrix, that in the filler material(s), that between adjacent filler particles, and that from the filler into the matrix and vice versa. The process of charge carrier transport can be divided into two steps: the injection of charge carriers into the material (e.g., Fowler-Nordheim or Richardson-Schottky transmission types) and the motion of charge carriers through the material via hopping, tunnelling, ballistic transport, diffusion, or metallic conduction.

1.5.1.1 Properties of Nonlinear SG Materials

Nonlinear field dependent composites are materials widely used for the SG system of machine coils and cable terminations. These composites are obtained by incorporating a nonlinear semiconductive powder as filler into a polymeric matrix that can be cured in the same way as the main insulation over which the SG is applied. Many researchers have explored this area with the goal of improving the electrical and thermal characteristics of the materials [11, 48, 49]. SiC and ZnO varistor material (ZnO-VM) are widely used as fillers in composites that have nonlinear conductivity. A composite that has a matrix filled with more than one powder, e.g., SiC and carbon black (CB) particles or SiC and ZnO, is also a possible option [48, 50]. Espino-Cortes et al. [51] studied the electrical and thermal performance of these materials for applications with PWM-VSCs. In the case of a polymeric matrix, different options are available, depending on how and where it will be applied. Varnishes, epoxy resins, polyester resins, and silicone rubber are some of the materials used in stress grading composites [14].

- Conduction Mechanism

The conduction mechanism in the nonlinear SG materials for a high electric-field, high temperatures, and high frequencies is a crucial research area where the goal is to enhance the material properties for specific applications. Studying the response of the SG material during actual operating conditions, when it is exposed to all these parameters, is very complicated and only a few articles that deal with this subject have been published [22, 67]. However, a great deal of research has been conducted in order to study the basic conduction mechanism of these composites in simpler conditions.

As is known, concentration of the filler strongly affects the conductivity and the nonlinearity of the composite. At a level well below the percolation threshold, electrical behaviour is dominated by the polymeric matrices, while well above this region, the electrical behaviour is dominated by the filler [52]. Nonlinear composites can be made by filling a polymeric dielectric with conductive particles below the percolation threshold in order to avoid building any conducting path and to raise the electric field in the dielectric between the particles [22, 53]. Alternatively, a dielectric can be filled with a nonlinear material like SiC or ZnO [54]. Hagen [55] and Martensson, et al. [56] have shown that when the filler consists of SiC, tunnelling mechanisms related to potential barriers are formed at the grain boundaries, which is the dominating conduction mechanism in the major part of the field range, due to the field emission, which is amplified by pre-avalanche multiplication. Contact between adjacent grains in the SiC powder can be modelled by two Schottky-like barriers connected back to back, which is the commonly accepted model for charge transport through semiconducting particle contacts, giving rise to its well known nonlinear I-V behaviour (the nonlinear loss is determined by the conduction current at the contacts). Unlike the ordinary Schottky barrier formed between a metal and a semiconductor due to the difference in their Fermi levels, however, this double Schottky-like SiC/SiC contact barrier is essentially a space charge barrier. It is shown that the I-V characteristics and their temperature dependence can be explained by the thermionic-field and field emissions through these barriers. In addition, the authors mentioned that further nonlinearity can be expected from the electrostatic attraction of adjacent particles in a high-field situation, thus enhancing the contact pressure. Consequently, in SiC composites, the conduction mechanisms can be considered to be dependent only on grain-to-grain contact properties. SiC itself presents a field dependent conductivity, the Schottky-like barrier model is commonly used to model grain-to-grain contacts, and the conduction is considered to be tunnelling through the potential barriers between grains [56].

In contrast to the characteristics of nonlinear composites filled with conductive particles (e.g. carbon black), the electrical properties of ones with nonlinear semiconducting fillers (e.g. SiC or ZnO) are reproducible, since the resistivity of the composite depends on the intrinsic (bulk) properties of the filler particle [47, 57]. Moreover, nonlinear behaviour is a strong function of filler nonlinearity if particle/particle contact occurs. However, Espino-Cortes et al. [14, 50] concluded that with SiC not much control of the grain-to-grain properties is possible, and the only way to modify the conductivity is to change the number of particle-to-particle contacts, either by changing the volume of the filler in the matrix or by changing the size of the particles. SiC also has a high hardness value, and it is difficult to reduce the particles to very small sizes.

It must be noted that in most cases, the field dependency of the composites is the same as that of the powder (filler), and the conductivity of the composite is lower than that of the powder due to the interface resistance between the particles caused by the polymer. However, higher nonlinearity exponents for some composites, e.g., those filled with ZnO, than for the powders have been observed [58]. This change in the charge transport mechanism occurs for very high fields and is called Fowler-Nordheim tunnelling. Hopping conduction is another mechanism that operates in these nonlinear composites. In addition, Martensson [59] discussed that frequency dependent properties are governed both by the interfacial barrier regions and by the surrounding polymer.

Both Strumpler et al. [60] and Varlow and Li [61] examined SG composites with nonlinear permittivity characteristics for cable terminations. Ferroelectric fillers with a linear dielectric can create a composite that allows permittivity to increase with the electric field. Any attempt to increase the permittivity through the use of different layers of coating or even through nonlinear permittivity requires an increase in the thickness of the coating: a major limitation for form wound coils.

- Measurement of Dielectric Properties

Appropriate modelling is imperative for the study of the electrical and thermal performance of SG materials exposed to a variety of stresses. The main parameters required for the modelling of the SG materials that are incorporated into a multi-dielectric system are electrical and thermal conductivities and permittivity.

Numerous studies have been published about I-V characteristics and the dc conductivity of the nonlinear materials that are applied in electrical apparatuses, such as cable termination, SG in machine insulation systems, and lightning arresters [48, 50, 62, 63 ,64, 65, 66]. The effects of the electric field, the temperature, the percentage of fillers, and the size of the particles on the conductivity of the materials are the common aspects that have been examined. However, few studies have considered ac dielectric properties, particularly at high frequency voltages.

Rivenc et al. [53] and Donnelly and Varlow [67] studied the ac I-V characteristics of nonlinear materials loaded with SiC and/or ZnO at 50 Hz and compared them with those of dc. However, they failed to extract ac conductivity and permittivity from the data measured. Martensson et al. [49, 56] measured the electrical properties of nonlinear composites filled with SiC at a low voltage in the frequency domain, giving the permittivity and the loss, and at a high voltage in the time domain, giving the dc-resistivity. A similar method [68] has been carried out in order to

measure the dc conductivity and the permittivity (at 100 kHz, 1 V) of a composite filled with SiC and black iron oxide (Fe_3O_4) as potential grading for high-voltage rotating machine coils.

Jiang et al. [69] suggested a theoretical base for measuring the dielectric parameters of nonlinear materials. Due to thermal breakdown, dc testing is usually effective in a relatively low electric field. They thus adopted a pulse test according to the following computational method in order to measure the conductivity and the permittivity of the ZnO ceramic materials in a higher electric field. Generally, in the time domain, the current density in a material is the sum of a resistive *(J_R)* and a capacitive *(J_C)* current, as follows:

$$J(E,t) = J_R(E,t) + J_C(E,t) = \sigma(E,t).E(t) + \varepsilon(E,t).\frac{dE(t)}{dt} \tag{1-1}$$

where σ and ε are the conductivity and the permittivity of the material.

Because the dielectric constant of the SG materials is often a weak function of the electric field, it can be considered as a constant. In this method, a single pulse is applied, and by monitoring the voltage/electric field and the total current, two different times t_1 and t_2 are selected such that *$E(t_1)$ = $E(t_2)$* but $dE(t_1)/dt_1 \neq dE(t_2)/dt_2$ (for example at the middle of the rising and falling times). Thus, from (1-1) the permittivity can be extracted as (1-2):

$$\varepsilon = \frac{J(t_1) - J(t_2)}{\frac{dE(t_1)}{dt} - \frac{dE(t_2)}{dt}} \tag{1-2}$$

The conductivity at field *$E(t_1)$* is derived from a combination of (1-1) and (1-2):

$$\sigma_1 = \frac{J(t_2)\frac{dE(t_1)}{dt} - J(t_1)\frac{dE(t_2)}{dt}}{E(t_1)\left[\frac{dE(t_1)}{dt} - \frac{dE(t_2)}{dt}\right]} \tag{1-3}$$

Although this method of calculating conductivity and permittivity is straightforward, however, it should be noted that the calculated parameters, particularly permittivity, are valid only under the applied single pulse voltage. In other words, due to different polarization mechanisms and frequency dependencies, the permittivity of a material at a sinusoidal voltage with frequency *f* can differ significantly from the permittivity determined by the use of this method. In addition, the maximum electric field applied in the experiments [69] was about 0.6 kV/mm, which is not greater than the electric field that was applied in the dc or ac conductivity measurement tests for

the same or similar nonlinear materials in [48, 50, 63]. However, the parameters calculated using this method are relatively appropriate for modelling materials that are subjected to a single fast pulse, such as a switching or lightning surge.

Boggs and Zhou [22] determined that either a ramp dc voltage with a small superimposed ac voltage or a combination of a lightning surge or a switching surge voltage can also be used to measure resistive and capacitive currents accurately to find conductivity and permittivity. They showed that the latter method is beneficial for measuring over a wide range of electric fields, particularly very high electric fields, e.g., 5 kV/mm, which surge arresters or cable termination are normally exposed to.

Tokoro et al. [70,71] investigated the high-field dielectric properties of low density polyethylene (LDPE) films at frequencies from 50 to 400 Hz at room and high temperature (100 °C). These materials are widely used for insulating materials in such products as power cables. The researchers showed the effects of temperature, the electric field, and the frequencies on the dissipation factor (tan δ) and the ac conductivity of the materials. They concluded that the ac conductivity becomes independent of the frequency of the applied field in a region of strong fields and high temperatures. In addition, for high temperatures and strong fields, tan δ tends to have a large field dependency and to be almost inversely proportional to the frequency.

The homogeneity of the material is another important aspect that has not been adequately studied. Since the composites are produced by the random dispersion of conductive particles in the resin matrix, an uneven distribution of filler clusters occurs during the manufacturing process. Thus, inhomogeneous and anisotropic formation will result which was discussed by Tucci and Vitelli [72]. Hong et al. [73] also studied the non-isotropic property of the epoxy composite materials used for the insulation of rotating machines subjected to water diffusion, i.e., leaking cooling system.

1.5.1.2 Properties of Conductive Armour Tape (CAT)

As mentioned earlier, CAT is normally made of a polyester fleece or glass tape impregnated with a CB or graphite loaded resin binder. Composites filled with CB/graphite are usually linear conductive materials, which means that the conductivity remains reasonably constant with variation of electric field over a wide range of frequencies. In composites that have CB, the nonlinearity in conductivity is not present if the composite is percolated [49], in that case the conductivity is due only to the ohmic conduction through the clusters formed by the particles. Near the percolation threshold, a weak and non-reproducible nonlinearity can be found in CB

composites, the conduction process in this case can be attributed to electrons tunnelling through thin layers of the insulating matrix between particles [14, 46, 74].

The influence on conductivity of the properties of the fillers, such as size, hardness, shape, and distribution was extensively investigated by Strumpler and Galtz-Reichenbach [47]. Zois et al. [46] studied the frequency dependency of the ac and dc conductivities in polypropylene/carbon black (PP/CB) composite. As with the SG materials, little work has been reported with respect to studying the effect of anisotropy in the CAT. Malamud [75] suggested that, for specific applications, the anisotropy of the coating can be used to limit the current induced by magnetic fields.

- Influence of Coil Manufacturing and Aging on Material Properties

Although the resistivity of the CAT is not voltage dependent, the final resistivity is affected by several parameters, the most important of which is related to the processing of the coil, which is commonly VPI. The volume and surface conductivities are strongly influenced by the extent to which VPI resin coats the conductive particles and by the degree of overlapping in the application of the CAT. The CAT may be applied in a catch-lapped or half lapped configuration. Because the principal path of the current in the CAT is along the tape's longitudinal axis, the overlap of the tape leads to a secondary mechanism for conduction [76].

No specific value is assigned for an increase in resistivity following VPI, but an increase between 5 and 20 times could be a reasonable value for conductive fleece tapes [15, 16, 18]. However, Brandes et al. [16] stated that the surface resistance of polyester fleece conductive tape from 200 to 3000 Ω/sq will demonstrate a 0.5 to 10 kΩ/sq final resistance after application. This range is equivalent to volume conductivity from about 0.25 to 5 S/m with a finished average thickness of 0.4 mm. Brütsch and Hillmer [77] also showed that, after a temporary increase due to resin impregnation, the surface resistivity of the CAT changes to the correct value and stays constant during long term aging.

In the above context, Emery [15] suggested that because the resistance of the CAT decreases over its lifetime due to thermal aging, e.g., by three times, minimum surface resistivities about 375 Ω/sq for air-cooled machines and 1800 Ω/sq for hydrogen-cooled machines are often specified in order to avoid high power dissipation and carbonization of the tape over its expected lifetime. However, one of the controversies is the minimum surface resistance that Liese and Brown [78] have suggested for CAT. They showed that a minimum surface resistance of 5 kΩ/sq is recommended for the CAT in order to prevent vibration sparking (VS) or spark erosion in large

air-cooled generators. The root cause of VS is slot conductive coating that is too-conductive, together with at least some bar vibration in the slot. However, Stone et al. [79] pointed out that the minimum surface resistance of 5 kΩ/sq seems to be not a reasonable value because many stators with loose bars and a surface resistance lower than 5 kΩ/sq apparently do not have VS.

1.5.2 Performance of Conventional Stress Relief System at Power Frequency

Numerous articles have been published that are related to two principal research topics with respect to SG systems: design and the performance evaluation.

1.5.2.1 Design and optimization of SG Systems

A number of considerations are required for the design and optimization of an effective SG system. The threshold stress or maximum acceptable field, the maximum voltage at the end of the SGT, and maximum available length and thickness are usually the important constraints. Minimizing power loss in the SG system can also be the main objective function for any optimization activity [11, 16, 24, 80, 81], which means that the conduction characteristics, the length, and the thickness of the SG coating are the variable parameters. Genetic algorithms are one of the techniques that have been recently used for the optimization of the SG system [14, 82]. These designs have been produced for conventional SG, based on nonlinear resistive composite materials, under a power frequency.

1.5.2.2 Surface Potential and Electric Field Profiles

For many years, the measurement of surface potential has been a popular method of evaluating the electrical performance of an SG system at 50 or 60 Hz [12, 14, 17, 83, 84, 85, 86]. The measurement has been performed mostly by using an electrostatic voltmeter (ESV) as a non-contact measurement method [14, 84, 85, 86]. According to the distribution of the potential, the average gradient surface potential, or electric field, is calculated based on the distance required for the surface potential to rise from the ground to the maximum applied voltage. Because the ESV can be used only for dc and low frequencies, e.g., less than 100 Hz, in some studies, the surface potential was measured directly using a contact method at high frequencies or with repetitive fast pulses [66, 87, 88]. With the contact measurement method, the impedance of the high voltage probe (as a voltage divider) highly influences the results, and therefore, for each point of measurement, a separate calculation must be performed in order to calibrate the data measured.

A new method has recently been developed for measuring the surface electric field directly using an optical miniature field sensor based on the linear Pockels effect [89, 90]. Using a Pockels' crystal as an electro-optical power sensing system to measure an electric field has several advantages over electrical methods, such as lack of interference from electromagnetic radiation, high sensitivity and wide frequency bandwidth [91]. Kempen et al. [92] compared the surface potential profiles along the SGT of a sample obtained using three techniques; ESV, compensated bridge circuits, and an optical miniature field sensor based on the linear Pockels effect. They showed that the latter is the most robust measurement method. In this method, the profile of the surface potential is calculated by the integration of the surface electric field measured. It must be noted that the problem mentioned in [92] with respect to measuring the surface potential using ESV (reduced surface potential due to the interaction with the test object) has not been observed by Sharifi et al. [93] or in other work. The accuracy of the ESV measurement strongly depends on its field sensing method; e.g., ESV with a vibrating Kelvin probe, which vibrates sinusoidally in the direction perpendicular to the surface tested, combined with a field nulling technique produces reasonable results. The accuracy of this method for the measurement of a divergent field, such as that along an SG system is analyzed in Chapter 4.

1.5.2.3 Performance of Slot Conductive Armour Coating

Many studies have investigated the surface resistance of conductive armour coatings using different materials and constructions with a variety of thermal and electrical stresses during an aging or voltage endurance test at a power frequency [15, 17, 18]. A number of factors that may be responsible for damage to this coating, both paint and tape, were discussed and analyzed in [94] and [95]. Stone et al. [79] showed that slot discharge and vibration sparking are the main causes of deterioration of conductive armour coating.

Cargill and Edwards [96] presented theoretical and experimental results in order to show that the high capacitive charging current at high frequencies, which is associated with fast transients or power supply harmonics, can build up a large voltage across the gaps between the coil surface and the stator slot. This voltage may be sufficient not only to generate sparks but also to maintain an arc for a significant period of time following the initial spark. Large and old machines with high values of coil capacitance and some degree of damage to the conductive armour coating are at the greatest risk of developing these high energy surface discharges. Hence, a surface resistance below 1000 Ω/sq is suggested for the conductive armour coating of coils in machines intended for operation with inverter supplies or in systems where significant waveform distortion is caused by converter equipment. However, this maximum surface resistance is in conflict with

the minimum resistance that Liese and Brown [78] suggested (5 kΩ/sq) for large air-cooled generators in order to prevent vibration sparking (VS) as discussed in section 1.5.1.2. Although VS is most likely to occur in generators rather than motors, because the likelihood of VS increases with the dimensions of the machine, it has been noted on some motors in the UK. In addition, in a global VPI stator, the coils are effectively glued to the stator core so that loose coils would not normally be expected. However, if there is a large clearance between the coil and the slot, and the coils are subjected to load cycling, then loose coils and slot discharge may occur in some designs [97].

1.5.3 Repetitive Fast Pulses and Conventional SG System

From the early 1990s and following the development of power electronic inverters and converters, serious consideration has been given to the effects of repetitive fast pulses on the insulation system of MV cables and drive duty motors [98, 99, 100]. However, in 2003 for the first time, Baker et al. [101] conducted a preliminary investigation of the performance of conventional SG system for Type II insulation systems in inverter fed motors. Wheeler [37] then calculated the surface potential and field along the SGT on samples energized by high frequencies and determined that, the level at which surface discharge can occur may be as low as 450 V/mm. In another study [102], 600 V/mm was taken as an empirical value for the inception of surface flashover. However, it seems that this value is an average surface field along the SG system and is not the maximum gradient voltage, because even with 1 kV/mm local stress, no discharge was observed [66, 88].

Espino-Cortes et al. [51, 103] analyzed the effectiveness of conventional SG systems on form-wound coils under fast rise time pulses and showed that thermal stress can be developed at the slot exit on the CAT. They suggested that both the SG system and the CAT must be designed together in order to ensure effective relief of the stress on drive duty motor coils.

Ming et al. [104] presented laboratory results that showed a local temperature increase in the SGT region of a 13.8 kV test bar, energized by 1 kHz bipolar square pulse voltage with different rise times of 0.7, 5, and 60 μs. They also compared their results with those obtained with 50 Hz and 1 kHz sinusoidal voltages. They showed that a hot spot occurs only in the SGT area near the end of the CAT, which means that they overlooked the hot spot on CAT at the slot exit because of the test bar configuration used in the study. In addition, the applied pulse peak was only 8.5 kV, which was much lower than the peak of the phase-to-ground voltage that a 13.8 kV coil is subjected to in actual inverter driven motors. Moreover, the effects of the other parameters of the

pulse waveform on the temperature rise, such as the pulse width and the fall time, were not investigated. Because the slot was not properly simulated in the test bar, not only was the localized thermal stress at the slot exit missed, but the influence of the rise time on the temperature rise of the SGT was also overestimated.

Further studies were conducted by Ming and his group [88] in order to measure the surface potential along the SGT and to calculate the surface electric field when the sample was energized by a high frequency sinusoidal voltage or a bipolar square pulse voltage. To find the surface electrical stress, four electrodes (copper wire) 20 mm apart were formed on the SGT area, and the potential at each electrode was measured directly and then calibrated. Using a computer simulation, the surface potential for each case was calculated, and the surface field was extracted. The researchers concluded that the electrical stress increases with faster pulses and higher voltage levels. The method of extracting the field was not presented. However, the measured and calculated potential were not well matched. Because the distance between the electrodes cannot decrease due to surface sparking, this method has poor accuracy for electric field calculations. In addition, forming copper wire to be the electrodes around the SGT can influence the surface electric field particularly for the method used to determine the inception of surface discharge.

In another work [105], researchers studied the effect of pulse polarity on the distribution of the surface potential and the temperature rise on a SGT region of a 13.8 kV test bar energized by a square pulse voltage. The temperature rise due to a 1 kHz bipolar square wave pulse voltage of ± 8.5 kV was much higher than that due to a unipolar pulse voltage of +8.5 kV and slightly lower than that due to a unipolar pulse voltage of +17 kV. Larger value of dV/dt for ± 8.5 kV pulse voltage compared to +8.5 kV pulse voltage is the reason that a higher temperature rise was produced. However, the reason for a higher temperature rise produced by a +17 kV pulse voltage than a ± 8.5 kV pulse voltage was not fully investigated. Moreover, most of commercial PWM-VSC generates waveforms like that shown in Figure 1-7 as two or multi-level unipolar PWM pulses. Thus, if the peak of the phase-to-ground voltage for actual two level unipolar PWM pulses is 8.5 kV, the equivalent waveform is a unipolar square pulse with the same amplitude, and applying a ± 8.5 kV bipolar square pulse imposes higher stresses that may be appropriate only for an aging test.

The effects of the rise time and repetition frequency of the repetitive pulses on the electrical and thermal stresses along the SGT have been studied by Speck et al. [66]. Using a direct measurement of the surface potential and temperature and a computer-aided model, they showed that the surface potential profile along the SGT of the specimen varies only negligibly with the

rise time of 0.3 and 3 μs and is independent of the 1, 5, 20 kHz pulse frequencies of a three level converter. In addition, the power loss and temperature rise on the SGT strongly depends on the repetition frequency and is independent of the rise time. For the test samples, copper tubes wrapped with mica tape, CAT, and SGT, which were used for voltage rating 6 kV. As mentioned, this sample configuration cannot represent all the stresses associated with actual coils subjected to repetitive pulses, particularly at the CAT and the bar corner sides. Another conclusion of their work is that a higher conductive SGT is preferable for pulse application because it decreases the electrical stress and prevents surface discharge although the loss and thermal stress increase. However, all the results presented need to be investigated in more detail.

The performance of conventional SGT and CAT during long-term aging has been investigated by Chen, Gao, and Mouton [106]. In their study, the researchers evaluated the impacts of repetitive fast pulses on all insulation components: turn insulation, ground wall insulation, and the SG system in the MV motor stator windings. There is little and somehow confusing information about the pulse test procedure for SG evaluation. The same test procedures seem to have been adopted for both the groundwall insulation and the SG system pulse test. The tests were performed on 6.6 kV coils energized by 20 kV peak repetitive pulses. In the paper, the term “high frequency voltage” has been alternatively used to indicate the voltage generated from a spark gap oscillator (SGO), which is not a correct expression for a repetitive impulse voltage. The pulse generator used in their study is similar to the one recommended by IEC TS 60034-18-42 [4]. However, this technical specification, recommends different qualification tests for the insulation components. For example, according to the qualification test procedure for the SG system, the samples must be subjected to a 100 h impulse voltage test, and the voltage impulse should be at least 1.3 times the magnitude of the voltages to be withstood in service. Hence, 250 h and 20 kV impulse peak seems to be considerably beyond the requirements. Furthermore, the test-pass criteria have not been taken into account, at least in the work presented. Moreover, because the entire emphasis in this study was for CAT and also because no hot spot can be observed at the end of the CAT, the implication is that the 6.6 kV coils had no SGT. If this is true, the term “SG system” is another confusing expression to use in this study. Nevertheless, developing hot spots at the slot exit and examining their relationship to the surface resistance of the CAT is one of the notable findings of this work. Four different armour coatings were investigated with respect to pulse tests: the one with the lowest surface resistance (after VPI) had the best performance, and no hot spot at the slot exit was observed. However, some of the given surface resistance values of the tape after VPI treatment need to be checked; e.g., in one case, the surface resistance decreased after VPI. In addition, because the coils probably had no SGT, the maximum electrical stress at

the end of the CAT was overlooked. If low resistance CAT is used, the electrical stress can move to the end of the CAT and in the case of a high electric field in that area, no hot spot can develop there in the absence of any resistive coating.

1.5.4 Repetitive Fast Pulses and Unconventional SG Systems

A sectionalized conductive stress grading system was proposed by Espino-Cortes et al. [51]. With this method, the conventional resistive stress grading system is sectionalized into two parts, and the electrical conductivity of the armour coating in the sectionalized system is increased. Hence, the stress that can be possibly concentrated at slot exit, and therefore the Joule heating from repetitive fast pulses at that region, are both distributed over a larger area. However, the effectiveness of the method is somewhat dependent on the electrical conductivities of the highly conductive and of the semiconductive tapes. In addition, the stress that can be developed on SG tape was not studied. As well, the performance of this method after long-term aging has not yet been evaluated.

Wheeler et al. [87] suggested a method that they refer to as a "sleeved system." In this method, two layers of nonlinear resistive stress grading tape are applied, separated by a layer of groundwall insulation. Although this method shows promise, the results published are not sufficient to enable the evaluation of long-term performance. In addition, the surface temperature profile along the SG system is not studied, and this aspect is important for fast repetitive pulse applications. According to the previous study as well as recent research [106], during the rise-time of the pulses, at slot exit, there can be high electrical and thermal stresses on the conductive armour tape; however, this issue is ignored in the design of the sleeved system.

No research has yet been conducted with respect to utilizing a capacitive SG system based on conductive foils for PWM-VSCs drive-fed motors. Comprehensive research must be undertaken in order to design and evaluate this SG concept over the long term, which is one of the objectives of this work.

1.5.5 Modelling of SG System

For many years, programming the finite element method (FEM) to compute electric field for nonlinear materials and thin layer problems has proven difficult, because the conductive armour and stress grading materials are typically a fraction of a millimeter thick, and the depth of the SG is orders of magnitude smaller than the other dimensions associated with form-wound coils.

Baker et al. [107] discussed the programming problems involved in cases that have large differences in the thickness of layers. They explain how a normal finite element formulation leads to elements in the mesh that have poor aspect ratios, which can lead to numerical instability, particularly in a nonlinear regime. For this reason, they introduced a surface element formulation for the SG layer that represents the material properties with no physical thickness in the model. This formulation assumes no voltage drop across the thickness of the tape but only along its length and width. Although this simplicity seemed reasonable at that time, the results obtained were not accurate. In addition, the method can be used only for steady state ac frequencies and cannot be applied to transient analysis in time dependent problems.

Although Kishky et al. [108] introduced a method for the time-domain analysis of nonlinear SG, their modelling is based on a number of simplifications. They introduced a lumped circuit model of nonlinear resistive SG system in which the SG and main insulation are represented by series impedance (resistance) and the shunt admittance (capacitance). The main insulation capacitance must be computed from the winding design specifications. In the recent work, Kishky et al. [109, 110] developed a MATLAB® program for solving the nonlinear field dependent conductivity of the SGT at each time step that is incorporated into the lumped circuit model, depicted in Figure 1-9, in order to simulate a system with a non-sinusoidal voltage.

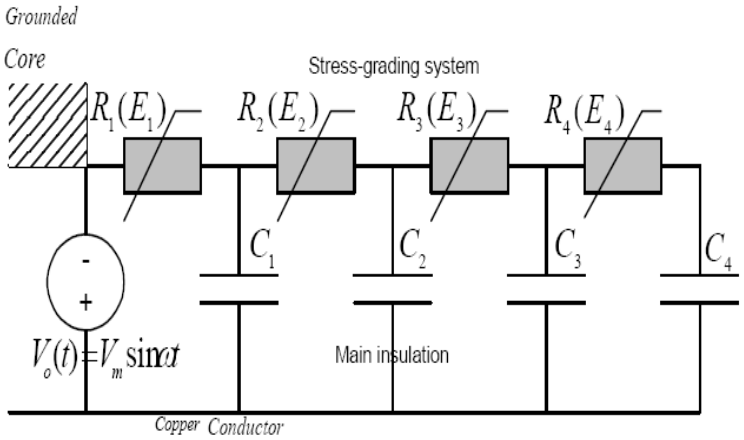

Figure 1-9: One-dimensional lumped circuit model of the end portion of a typical form wound coil [110].

Although, these studies represent progress in adapting network and lattice models for time dependent simulation and non-sinusoidal voltage applications, the results have not been verified through experimental work, and they still include many simplifications that prevent their use for accurate modelling and complicated studies. For example, the actual geometry of the system, such as layer thickness, layer overlap, and edge effect, cannot be considered due to the one

dimensional modelling, and the radial electric field (perpendicular to the surface) can also not be calculated; the nonlinearity and coupling of the material properties to electric field and temperature are normally ignored or simplified; and last but not least, the influences of heat generation in the context of a thermal analysis are entirely disregarded in all existing approaches.

The advantages of modelling and simulation based on the FEM include the detailed simulation of an existing configuration; the implementation of nonlinear field- and temperature dependent material properties; coupled electric, thermal, and fluid dynamic analysis; and the possibility of immediately investigating the influences of design modifications and their impact.

Zheng and Boggs [111] discussed the difficulties of using the FEM to compute field parameters for transient nonlinear field problems. However, they developed a one-dimensional FEM software for their case studies.

Espino-Cortez et al. [14], by means of COMSOL-Multiphysics®, created 2D-transient FEM simulations for an electro quasi-static model of SG systems, either conventional for a power frequency or sectionalized for PWM-VSCs. In this modelling, for a sinusoidal steady state condition, resistive heating was used to indicate the Joule heating of the materials. However, to determine the temperature profile that interacts with all heat sources, coupled electro-thermal modelling is required. Moreover, only the dc conductivity of the SGT was used for material modelling for dc, ac, and pulse applications, and the effect of the frequency dependency of the material was ignored. However, as mentioned, in nonlinear SG materials, both the resistive and capacitive current are strongly frequency dependent. Thus, the frequency dependency of the material properties must be taken into account for high-frequency and pulse simulations; otherwise inaccurate modelling and analysis result.

The actual geometry of the machine coils is much more complicated than can be used in 2D modelling. Sharp corners or the non-perfect contact between the stator slot and the coil's outer surface can significantly change the electrical and thermal field profile and intensity. To produce precise modelling with respect to actual coil geometry requires 3D modelling.

In a very recent work [90], an initial attempt has been made to adopt 3D modelling in order to study the electric and thermal fields along an SG system. In the study, the actual geometry was simplified and treated as a tube in order to prevent singularities and divergence in the FEM calculation. The algorithm for the coupled electric and thermal field calculation was developed through two nested recursion loops. The case study was conducted only for a 50 Hz power

frequency. At this stage, the developed 3D modelling provides no advantage over the 2D because the actual geometry of the coils is simplified to an unrealistic form.

Transient coupled electro-thermal field analysis with highly nonlinear elements and complex geometry and with a non-sinusoidal voltage is generally associated with convergence problems. Adopting a method of overcoming this problem is thus always necessary. For a capacitive SG system based on conductive foils, even in steady state analysis, special attention must also be paid to eliminating convergence problems and achieving precise results. The high transition in conductivity between the foils and the groundwall insulation can lead to unrealistic results that must be resolved through more study.

In most previous work, the anisotropy and frequency dependency of the materials in the SG system modelling have been ignored. In addition, only the tangential electric field has been accounted for, and other directional components of the electric field have been overlooked. The effect of all of these factors can be pronounced at high frequencies and pulse applications and must be studied comprehensively.

1.6 Aim of the Present Work

Recent studies of Type II machine insulation systems have underscored the importance of evaluating and improving the performance of conventional SG systems under PWM pulses. These highly repetitive fast pulses create extra electrical and thermal stresses that have adverse effects on the performance and reliability of the resistive stress control systems, which can significantly reduce the lifetime of an insulation system.

Nonlinear resistive SGT and slot conductive armour coating are conventional methods of controlling the surface electrical stress on form-wound motor coils that are normally designed for 50 or 60 Hz power frequency. The performance of these components under repetitive fast pulses is not well understood. Only a few studies have been conducted in this area in order to study the general performance of an SG system and the behaviour of the materials. Most have been conducted under unrealistic conditions, as discussed in section 1-5. The incomplete understanding of the behaviour of these materials, and the consequent inadequate modelling and design of SG systems are the motivation for this study.

This research was therefore focused on gaining a comprehensive understanding of the problems associated with existing, conventional SG systems in PWM-VSC drive-fed motors and on proposing an effective and reliable solution. To achieve these goals required material characterization and modelling of an SG system with respect to actual manufacturing and

operation conditions, and the introduction of a new stress grading system based on foils, either metallic or partially conductive, that is embedded into the groundwall insulation as a type of capacitive SG system.

The capacitive grading scheme, through a system of foils, is independent of frequency and therefore can provide the required mitigation of the stress caused by steep front voltage pulses. This technique has the advantage of not being affected by the variability in the conductivity of the SG coating that occurs during the manufacturing process. To evaluate the performance of the developed method and to determine possible problems associated with this technique, computer modelling and experimental tests including performance and qualification tests were carried out.

The following were the main objectives of this research:

- To perform a systematic study in order to identify the behaviour of an SG system that is subjected to repetitive fast pulse voltages.
- To find the correlation between the electrical and thermal stresses that develop on an SG system and the voltage parameters, the manufacturing process, and the machine design configuration.
- To characterize the materials in a conventional SG system as a function of electric field, temperature, and frequency.
- To develop comprehensive electrical and thermal system modelling in order to identify and analyze the main problems in conventional SG systems when they are operating under repetitive fast pulses.
- To develop a capacitive SG system suitable for working under PWM-VSC that can help improve the electric and thermal performance of SG systems.
- To qualify the proposed SG system through standard qualification tests.

Chapter 2
Samples, Experimental Setup, and Modelling

2.1 Introduction

This chapter describes the methods of preparing the samples used in this research. The samples are made from the identical materials used in MV motor insulation systems. The procedures for the characterizations of the materials are detailed, and the test setups and procedures for evaluating the complete insulation system under electrical and thermal stresses are outlined for power frequency and fast repetitive pulses. The computational methods for modelling of electric and thermal fields using FEM and for the analytical modelling of the repetitive pulses in numerical simulations are discussed.

2.2 Sample Preparation

The dielectric properties and thermal conductivity of the SGT and the CAT change drastically as a result of the VPI treatment and the overlapping of the tapes during the construction of the coils. To model and analyze an actual SG system, the parameters of the materials must therefore be measured on assembled motor coils or on samples prepared in accordance with Type II insulation design and VPI manufacturing standards.

Figure 2-1 illustrates the sample configurations for the measurement of the dielectric characteristics. Three different tapes were used to build these samples: glass fibre reinforced mica tape, carbon loaded polyester fleece (non-woven) conducting tape as CAT, and SiC grading tape or SGT. To measure the parameters in the longitudinal direction, a 686 mm × 38 mm × 9.5 mm copper bar was first wrapped with mica tape. Then a 1/2 lapped layer of CAT or a 2/3 lapped layer of SGT was applied over the mica tape. For the parameters in the thickness direction, a 300 mm length of 50 mm diameter copper pipe was wrapped with a 1/2 lapped layer of CAT or a 2/3 lapped layer of SGT. The bar and the pipe assemblies were then pre-baked and impregnated according to the standard process for a VPI form wound stator coil. In this study, solventless aromatic epoxy impregnating resin was used for the VPI process.

Figure 2-2 shows the second group of samples that were used for performance, qualification, and acceptance testing of the conventional and proposed SG systems. These samples are short sections of copper bars with taping identical to that of VPI 13.8 kV form wound motor coils with either the conventional SGT or the proposed capacitive SG system. To build the conventional

13.8 kV bar samples, four different tapes were applied: mica tape, CAT, and SGT, which were also used for the previous samples, plus an additional treated glass armour tape as a protective layer. Although the application of a protective layer has an adverse effect on heat dissipation, it assists with both resin retention and the creation of a more uniform surface [86]. For the samples with a capacitive SG system, 4 mils, or 0.1 mm, aluminum tape was embedded in the groundwall insulation. However, the possibility of using highly conductive tapes such as CAT instead of metal foils was also investigated.

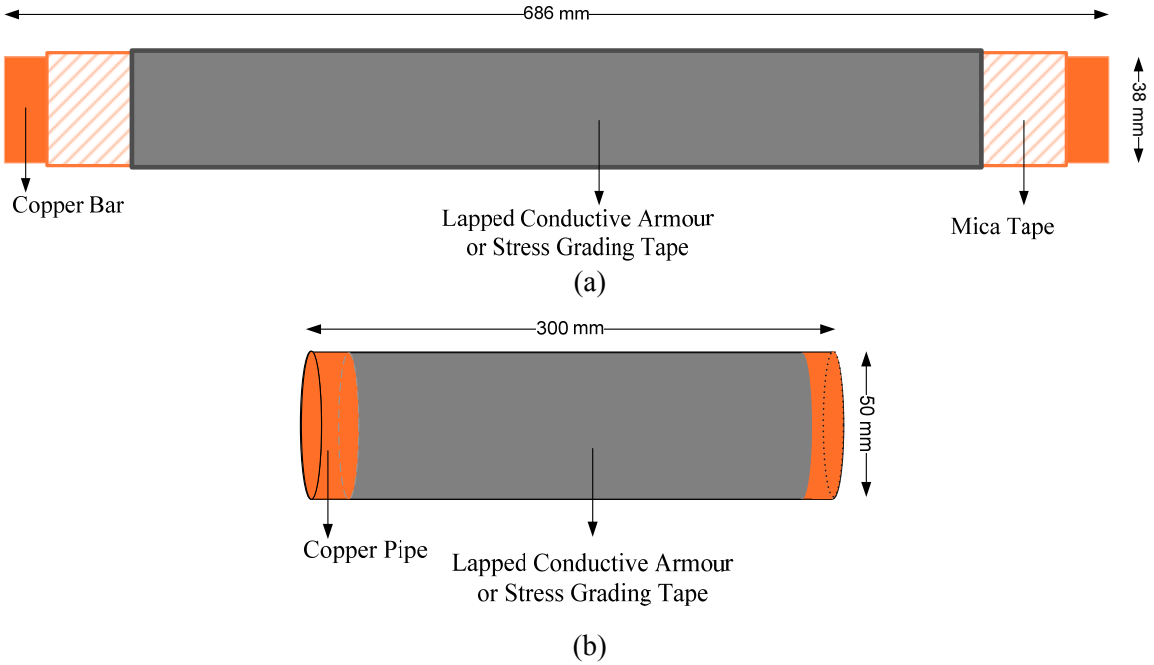

Figure 2-1: Illustrations of SGT and CAT samples for volume dielectric parameters along the (a) longitudinal and (b) thickness directions.

For the entire second group of the samples, two voltage endurance (VE) plates were used to simulate the motor grounded slot. The dimensions of the type C110 copper flat bars are 686 mm × 38 mm × 9.5 mm, with 1.6 mm radius edges. The edge radius has a significant effect on the maximum stress at the edges [112], and for the VE test, the appropriate edge radius must be selected.

The test samples were prepared in accordance with the specifications for Type II insulation systems and the manufacturing requirements for a medium voltage motor at GE Canada Peterborough.

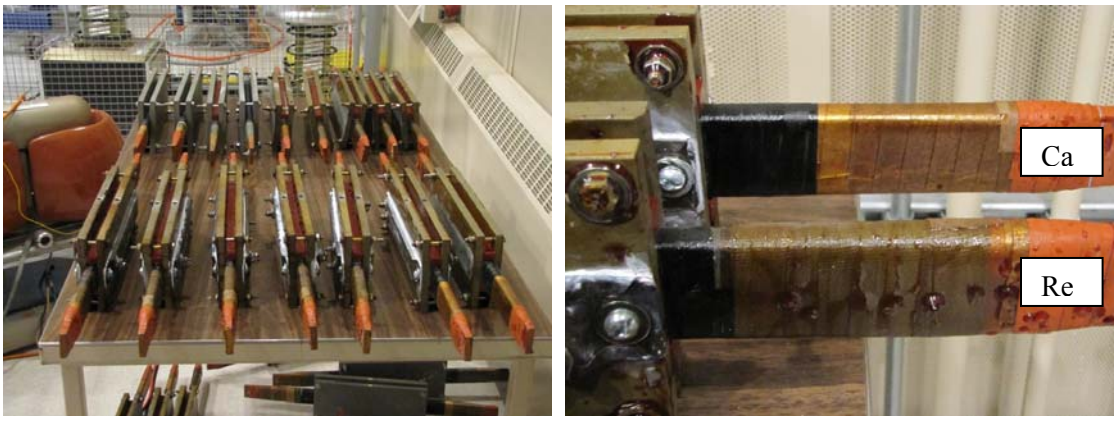

(a) (b)

Figure 2-2: (a) Collection of the samples; (b) Two samples with different SG systems; conventional nonlinear resistive-Re, and capacitive- Ca.

2.3 Dielectric Parameter Measurement Techniques

This section introduces the methods used for measuring the dielectric parameters of the CAT and SGT.

2.3.1 Volume Conductivity

The conductivity, or resistivity, of the CAT and SGT is one of the most important parameters for studying the stress on the endwinding of form wound motor coils. Suppliers provide the surface resistivity of the tapes for comparative purposes, and these values are obtained by standard measurements. However, these values are not actual physical material properties and cannot be used directly in the modelling because of the way the tapes are applied to a coil and because the VPI process drastically modifies the characteristics of the lapped tape construction. For accuracy in modelling, the volume conductivity of the coatings must be determined from measurements of the samples prepared in accordance with Type II insulation design and VPI manufacturing standards.

In the common methods of measuring volume resistivity that are specified in ASTM standards D257-99 [113] and D4496-04e1 [114], three electrodes are used. The sample is placed between the electrodes, one of which acts as a guard. This method is not appropriate for measuring the conductivity of conductive armour or SGTs in actual conditions. With the standard method, the lapping of the tapes influences the radial current. Since, in actual conditions, the surface current flows in the axial direction of these tapes, the conduction characteristics in this direction are much

closer to reality. A detail configuration of the samples illustrated in Figure 2-1 (a), used for measurement of the volume resistivity in the longitudinal direction is provided in Figure 2.3.

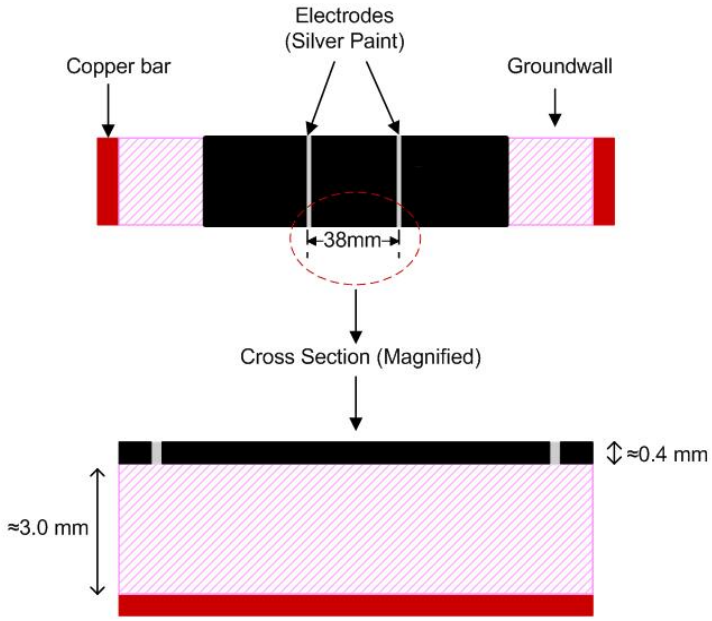

Figure 2-3: Sample configuration for the volume conductivity measurement. The black layer represents the conductive armour or SG tape.

On the outer surface of the manufactured samples, two narrow cuts separated by 38 mm were made through the tapes down to the groundwall insulation. The cuts were filled with silver paint, which then act as the two electrodes for the measurements.

The sample shown in Figure 2-1(b) was used to measure the volume conductivity of the materials along the thickness dimension. The copper pipe was used as the internal electrode, and aluminum tape acted as the external electrode.

2.3.2 AC Dielectric Parameters

The characterization of the nonlinear materials in actual operating conditions is vital for studying their performance when subjected to high frequencies and PWM pulse voltages. The methods used by previous researchers have been discussed in section 1.5.1.1. This section presents the theory of the method, used in this study in order to measure the ac dielectric parameters of the nonlinear SG materials.

In the frequency domain, the dielectric response of a linear material can be defined by its complex relative permittivity (ε^*), which is a function of angular frequency (ω), and is given by

$$\varepsilon^*(\omega) = \varepsilon'(\omega) - j\,\varepsilon''(\omega) \tag{2-1}$$

where ε' and ε" denote the real and imaginary part of the permittivity.

When measurements in the frequency domain are performed, the total loss, including a possible contribution from dc conduction, is

$$\varepsilon''_{total}(\omega) = \varepsilon''_{ac}(\omega) + \frac{\sigma_{dc}}{\varepsilon_0\,\omega} \tag{2-2}$$

This loss expression can be described by an equivalent total conductivity:

$$\sigma_{total}(\omega) = \varepsilon_0\,\omega\,\varepsilon''_{total}(\omega) = \varepsilon_0\,\omega\,\varepsilon''_{ac}(\omega) + \sigma_{dc} = \sigma_{ac}(\omega) + \sigma_{dc} \tag{2-3}$$

Therefore, the dissipation (dielectric loss) factor at each frequency is:

$$\tan\delta = \frac{\sigma_{total}}{\varepsilon_0\,\varepsilon'\,\omega} = \frac{\varepsilon_0\,\varepsilon''_{ac}\,\omega + \sigma_{dc}}{\varepsilon_0\,\varepsilon'\,\omega} \tag{2-4}$$

For dielectric materials classified as electrical insulation, σ_{dc} is negligible, and the dissipation factor can be represented by (ε"/ε'). However, for conductive and semiconductive materials and at low frequencies, it is assumed that in a non-static field, the dielectric loss due to the static (dc) resistance dominates the ac loss due to friction in the polarization processes. Thus, for simplicity, the frequency dependent dielectric loss can be neglected in most of the formulations at low frequencies. In this case, the conductivity (σ) can be represented only by either a static value or a function of the electric field and the temperature, as measured from dc tests [53]. The dissipation factor thus becomes $\sigma_{dc}/(\varepsilon_0\varepsilon'\omega)$. Although this approximation is reasonable for conductive materials at low frequencies, the frequency dependent component of the dielectric loss must be taken into account at high frequencies.

It must be noted that the formulations in (2-3) and (2-4) are appropriate only for modelling because in reality, at any frequency, the conductivity or the total loss cannot be expressed as separated components as defined. It is better to state that both the conductivity and the loss factor are functions of the frequency and temperature. In addition, for nonlinear field dependent dielectric materials such as SGT, the dc conductivity itself is a nonlinear function of the electric field and the temperature [93]. Both ε′ and ε′′ are also frequency and field dependent, resulting in the following:

$$\sigma_{total} = f_1(\omega, E, T) \tag{2-5}$$

$$\tan\delta = f_2(\omega, E, T) \tag{2-6}$$

For a nonlinear material, the concept of a complex permittivity is no longer straightforward. The following explains the practical methods of measuring the dielectric parameters. Dielectric materials can normally be modelled in two widely used equivalent forms as shown in Figure 2-4.

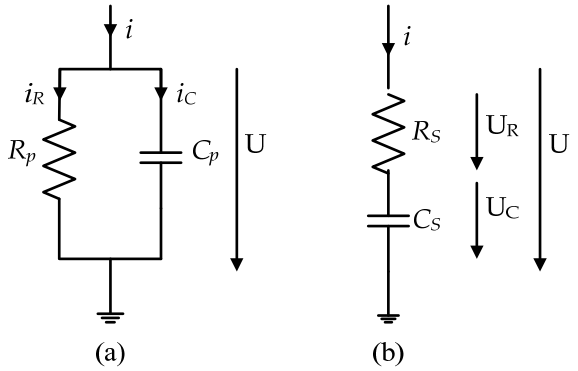

Figure 2-4: Lumped equivalent component models of dielectric materials: (a) parallel circuit; (b) series circuit.

In these models, at arbitrary frequency *f*, the dissipation factor, *tan δ*, is defined as the ratio of the resistive current to the capacitive current in a parallel model or of the resistive voltage to the capacitive voltage in a series model. These ratios can be expressed as:

$$\tan\delta = \frac{I_R}{I_C} = \frac{1}{R_p C_p \omega} \tag{2-7}$$

$$\tan\delta = \frac{V_R}{V_C} = R_s C_s \omega \tag{2-8}$$

It is normally assumed that the input voltage is purely sinusoidal at the fundamental frequency *f* or at the angular frequency *ω* as

$$v(t) = \sqrt{2}\, V \sin(\omega t) \tag{2-9}$$

Due to the nonlinearity of the material or load, the current can be written as a Fourier series:

$$i(t) = i_{dc} + \sqrt{2}\, I_1 \sin(\omega t - \theta_1) + \sum_{k=2}^{\infty} \sqrt{2} I_k \sin(k\omega t - \theta_k) \tag{2-10}$$

where I_k and θ_k are calculated from a Fourier series formulation.

Under this condition, it can be shown that the total active power becomes [35]

$$P = P_1 = V\, I_1 \cos\theta_1 \tag{2-11}$$

In other words, the dc and the harmonics of the current do not contribute to the active power drawn from the sinusoidal source. According to this expression, the effective resistance, e.g., R_p, and consequently the ac conductivity, can be extracted at any frequency. In these circumstances, the formulation for the total active power is straightforward; however, the calculation of the reactive power, displacement current, and dissipation factor is challenging due to the imprecise interpretation of these parameters in the presence of the harmonics. According to one definition, the apparent power *S* is the product of the rms voltage *(V)* and the rms current *(I)*. In terms of (2-9) and (2-10), the apparent power is thus

$$S = V\,I = V.\left(\sum_{k=1}^{\infty} I_k^2\right)^{1/2} \tag{2-12}$$

and the total reactive power *Q* can be defined as:

$$Q = \sqrt{\left(S^2 - P^2\right)} \tag{2-13}$$

Referring to (2-7) and (2-8), the dissipation factor can also be calculated as the ratio of the active power to the reactive power ($tan\delta = P/Q$). It is evident that after *Q* is determined, the displacement current and therefore the dielectric constant can then be extracted.

Another method of calculating the dissipation factor is a decoupling algorithm [115]. In this algorithm, the input voltage can have any periodical waveform. The detection of the zero-crossing point of the voltage triggers the data acquisition of the current. The voltage signal *v(t)* can then be extended to the negative coordinate axis in the time domain. Mathematically, this signal is a periodic odd function that can be expressed in the form of a Fourier series:

$$v(t) = \sum_{k=1}^{\infty} V_k \sin(k\omega t) \tag{2-14}$$

The measured current signal *i(t)* can also be transformed to its Fourier series:

$$i(t) = \sum_{k=1}^{\infty} \left(a_k \cos(k\omega t) + b_k \sin(k\omega t)\right) \tag{2-15}$$

Here, V_k, a_k, and b_k represent Fourier coefficients. According to the dielectric parallel model shown in Figure 2-4, the total current *i(t)* is

$$i(t) = i_R(t) + i_C(t) = \frac{v(t)}{R_p} + C_p \frac{dv(t)}{dt} = \frac{1}{R_p}\sum_{k=1}^{\infty} V_k \sin(k\omega t) + C_p \omega \sum_{k=1}^{\infty} k V_n \cos(k\omega t) \tag{2-16}$$

A comparison of (2-15) and (2-16) reveals that the resistive and capacitive currents can be shown as

$$i_R(t)=\frac{1}{R_p}\sum_{k=1}^{\infty}V_k\ sin(k\omega t)=\sum_{k=1}^{\infty}b_k\ sin(k\omega t) \tag{2-17}$$

$$i_C(t)=C_p\ \omega\sum_{k=1}^{\infty}kV_k\ cos(k\omega t)=\sum_{k=1}^{\infty}a_k\ cos(k\omega t) \tag{2-18}$$

The rms value of each current component can be calculated from (2-19) and (2-20):

$$I_R=\sqrt{\sum_{k=1}^{\infty}\frac{b_k^2}{2}} \tag{2-19}$$

$$I_C=\sqrt{\sum_{k=1}^{\infty}\frac{a_k^2}{2}} \tag{2-20}$$

With respect to (2-7), the dissipation factor can be defined as

$$tan\,\delta=\frac{I_R}{I_C}=\sqrt{\frac{\sum_{k=1}^{\infty}b_k^2}{\sum_{k=1}^{\infty}a_k^2}} \tag{2-21}$$

One of the benefits of this digital algorithm is that calculating dissipation factor requires only sampling the current signal. However, to calculate the equivalent resistance *(R_p)* from (2-17) and to extract the equivalent conductivity, both the voltage and the current must be recorded at the same time.

Using this technique, the real time displays of the load voltage and current signals were monitored and recorded as numerical data. The data files were imported to Matlab® for signal analysis in order to extract the conductivity and *tan (δ)* of the SGT and CAT samples.

Furthermore, as discussed earlier, the CAT and the SGT are not homogenous and not isotropic due to the construction process and tape lapping. In other words, the induced current is not in the same direction as the applied electric field [72, 116]. For anisotropic materials σ is a tensor that can be represented in a general form by a 3×3 matrix, as shown in (2-22), which is then reduced to a 2×2 matrix for two dimensional (2D) analysis.

$$\sigma=\begin{pmatrix}\sigma_x & \sigma_{xy} & \sigma_{xz}\\ \sigma_{yx} & \sigma_y & \sigma_{yz}\\ \sigma_{zx} & \sigma_{zy} & \sigma_z\end{pmatrix} \tag{2-22}$$

2.4 Experimental Setup

This section presents a brief description of the setups for the experimental work. The arrangements for the dielectric and thermal characterization of the materials and the setups for the measurement of the surface potential, the electric field, and the temperature profiles along the end portions of the bar samples are described. The procedure and test setups used for the qualification, acceptance, and diagnostic tests are also introduced.

2.4.1 DC Measurements

To measure the dc conductivity in the longitudinal or thickness direction, a variable high voltage dc power supply (0-20 kV), a highly sensitive ammeter (electrometer 6514 Keithley with a minimum ampere range of 20 pA and a 10^{-4} pA resolution), and an environmental chamber (for elevated temperature tests) were used.

The measurement of the surface (according to ASTM D257-99 requirements) and volume dc conductivity of the tapes as a function of temperature were conducted in a temperature controlled oven and the temperature was limited to 155 °C, corresponding to the class F thermal insulation.

2.4.2 AC and High Frequency Measurements

The setup presented here was used for ac dielectric parameter measurement at high frequencies and high electric field. It is also used for thermal analysis of the surface along the end portions of the bar samples.

As has been established, for conductive dielectric materials, the electrical conductivity and dissipation factors are two important parameters that reflect dielectric behaviour. Measuring these parameters in a low electric field can be accomplished with the use of a digital impedance analyzer; however, for a high electric field and high frequencies, these measurements usually are accompanied with difficulties. Most conventional *tan (δ)* measurement setups are designed for 50 or 60 Hz and cannot be used at high frequencies. As well, the dissipation factor of nonlinear conductive materials under high frequencies and high electric field is too large and exceeds the rating of many *tan (δ)* measurement setups. In this study, therefore, an alternative method of measuring ac dielectric parameters has been used, based on digital signal processing algorithm presented in section 2.3.2 [117].

A number of techniques can be adopted for generating high voltage (HV) at high frequency (HF). The resonant circuit is one of the most popular [118], but the circuit can generate high voltage only in a narrow band around the resonant frequency, and the output is highly attenuated

below or above the defined band. Generating a HF voltage over a wide band therefore requires variable HV inductors and HV capacitors.

In this study, the setup depicted in Figure 2-5 has been used in order to provide a variable HF and HV power supply for measuring both the ac dielectric parameter and the surface temperature along the end portions of the bar samples.

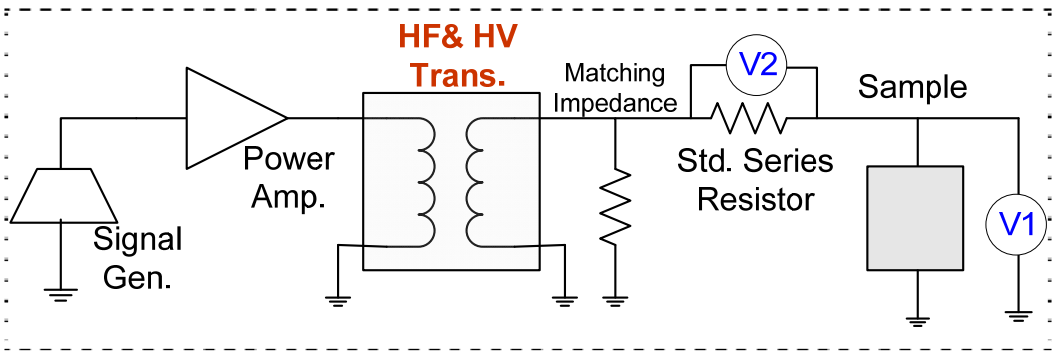

Figure 2-5: Experimental circuit for V-I measurements of SGT at high voltages and frequencies.

The setup is comprised of a HF and HV transformer fed by a signal generator (Agilent 33220A) through a low voltage power amplifier (Bryston 7B SST). The power and frequency responses of the amplifier and the transformer are appropriately matched. As the SGT sample is the load which is highly field dependent, the maximum power must be determined according to the load characteristics at both a HF and a high electric field. The series resistor must have a known frequency response so that the load current can be sampled accurately at the testing frequency. A HV resistor is also used in order to match the impedance at the power amplifier output. For signal processing purposes, both V1 and V2 are recorded and stored as data files by a digital storage oscilloscope (DSO).

To cover a wide frequency band from 1 to 100 kHz, two HF transformers from MagCap were used (1-20 kHz, 100 V/20 kV, 1A and 30-100 kHz, 100 V/4 kV, 1 A).

2.4.3 Thermal Conductivity Measurement

Thermal conductivity (TC) is a property of materials that relates heat flow to the temperature gradient. At a steady state condition and in an isotropic material, the heat flow is described by the following equation:

$$\frac{Q}{A} = -k\frac{dT}{dx} \tag{2-23}$$

where Q is the heat flowing through the cross-sectional area A, dT/dx is the temperature gradient across the material, and k is the thermal conductivity.

According to ASTM D5470 [119], thermal conductivity is measured with a thermal interface material tester [120], in which the thermal joint resistance is obtained by dividing the temperature drop at the interface by the heat flow rate at the joint. For this study, bond-line thickness measurements were performed using a Mitutoyo laser scan micrometer, LSM 503H. Figure 2-6 shows the setup and a close-up of the joint during the operation of the laser.

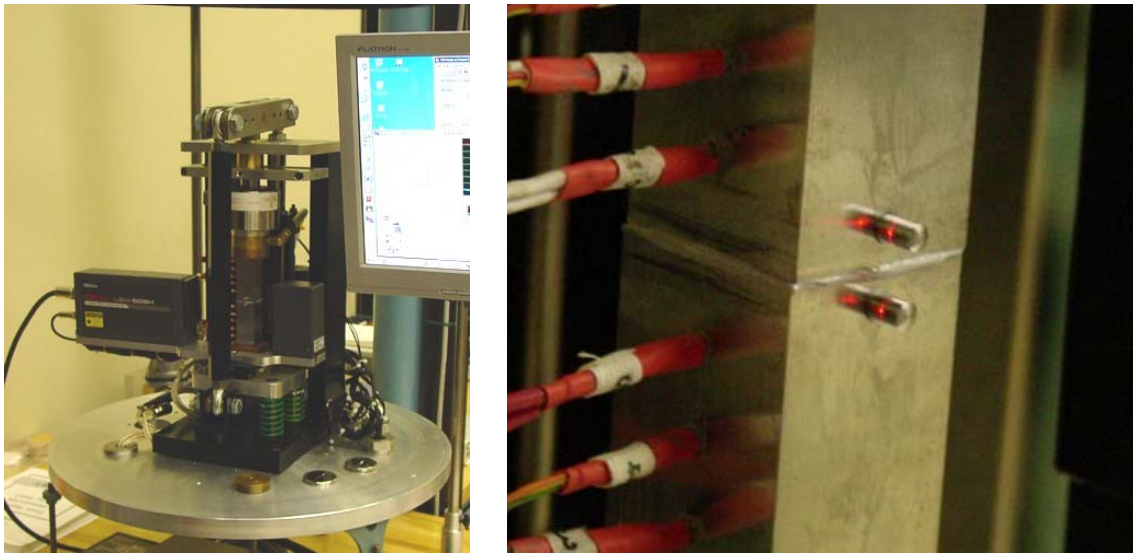

(a) (b)

Figure 2-6: Thermal interface material test apparatus in the Microelectronics Heat Transfer Laboratory at the University of Waterloo: (a) general apparatus; (b) close-up of the joint, including the laser-based measurement of the thickness.

The tests were performed under atmospheric conditions at a mean joint temperature of 50 ˚C. Temperature readings from the resistance detectors in the heat flux meters were used in order to calculate two quantities: the total heat flow rate through the joint, Q, and the temperature drop across the joint, ΔT. From these two quantities, the joint resistance can be calculated:

$$R_j = \frac{\Delta T}{Q} \tag{2-24}$$

Thermal conductivity was then calculated from the overall joint resistance using the following relationship:

$$k = \frac{t_{BLT}}{R_j \, A_j} \tag{2-25}$$

where $A_j = 645\,mm^2$ and t_{BLT} is the measured bond-line thickness from the laser micrometer.

Based on this method, the tolerance of the TC measurement is ± (0.05-0.1). To eliminate the effect of contact resistance, at least three different sample thicknesses must be tested. In a homogeneous material, thermal resistance varies linearly with the thickness. Thus, by fitting a line on the measured thermal resistance values plotted against the thickness, the contact resistance can be separated.

2.4.4 Surface Potential Measurements

As discussed in Chapter 1, measuring the surface potential has been a popular method of examining the effectiveness of SG systems [51, 54]. However, SG performance cannot be effectively evaluated according to the surface potential distribution alone, and a better evaluation must be obtained by extracting the corresponding electric field from the potentials measured. The simplest method is to measure the potential in very small steps and to calculate the surface electrical stress [93, 121]. Using an electrostatic voltmeter to measure surface potential is a reliable method that can be used to evaluate SG performance [122].

In this research, in order to measure the surface potential along the end portion of both the conventional and the proposed SG systems, an advanced electrostatic voltmeter (TREK 341A) was used. Figure 2-7 is a schematic of the experimental setup for the measurements at room or elevated temperatures. The electrostatic voltmeter uses a vibrating Kelvin probe that vibrates sinusoidally in the direction perpendicular to the surface to be tested, along with a field-nulling technique for noncontacting measurements at dc or low frequencies. The probe was mounted on a linear actuator that runs over the surface of the test sample so that the probe is kept between 2 and 4 mm above the surface, within the specifications recommended for the instrument [123]. The linear actuator was controlled by a PLC with steps of 1.0 mm. The test samples were the ones introduced in section 2.2. To bring the temperature up to 90 °C, the bars were heated using both a circulating current and strip heaters that were bolted to steel plates on either side of the bar sample. The sample was energized at 8 kV_{rms}, corresponding to a 13.8 kV coil. Figure 2-8 shows the actual laboratory setup in the high voltage laboratory at the University of Waterloo.

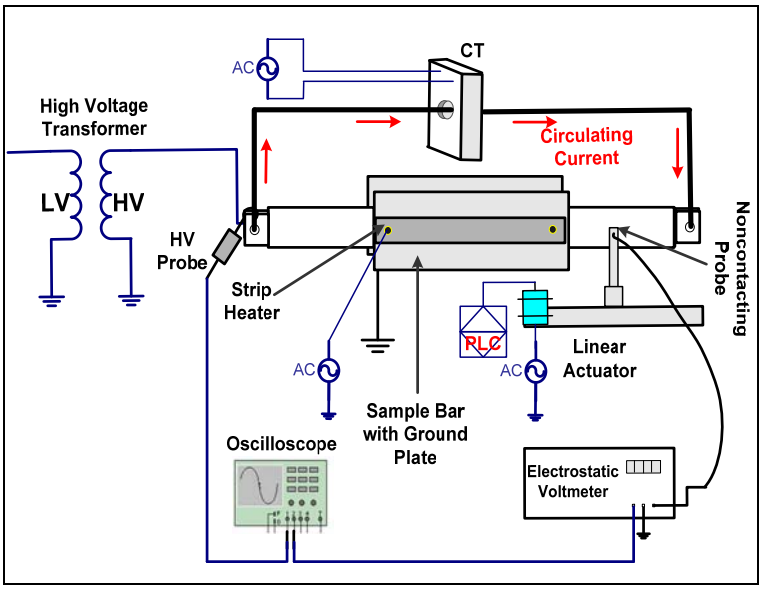

Figure 2-7: Experimental arrangement for measuring the surface potential at elevated temperatures.

A: Bar Sample with Grounded Plates
B: CT
C: Linear Actuator
D: Electrocstatic Voltmeter Probe
E: HV Transformer
F: Infrared Camera

Figure 2-8: Laboratory setup for measuring the surface potential illustrated in Figure 2-7.

2.4.5 Temperature Measurement Using an Infrared Camera

The surface temperature measurements were conducted with a FLIR SC500 infrared camera and with thermovision acquisition software. The spectral range of the detector is between 7.5 and 13 μm, and the temperature image is displayed in a 320 × 240 pixel array. The thermal sensitivity of the detector is 0.07 °C at 30 °C, and the accuracy of measurement is ± 2 °C [124]. The acquisition software, ThermaCAM™ Researcher 2.8 Pro SR-3, allows different types of post-processing of the temperature distribution in the infrared image. The emissivity was determined by comparing

two temperatures, namely the camera temperature of the sample heated to 50 °C in an oven and the temperature of the thermocouple as a reference. According to this calibration, the emissivity of the CAT and SGT were adjusted to 0.98 and 0.94, respectively. Figure 2-9 depicts one of the setups used for measuring the surface temperature along the bar sample when it is energized by repetitive fast pulses.

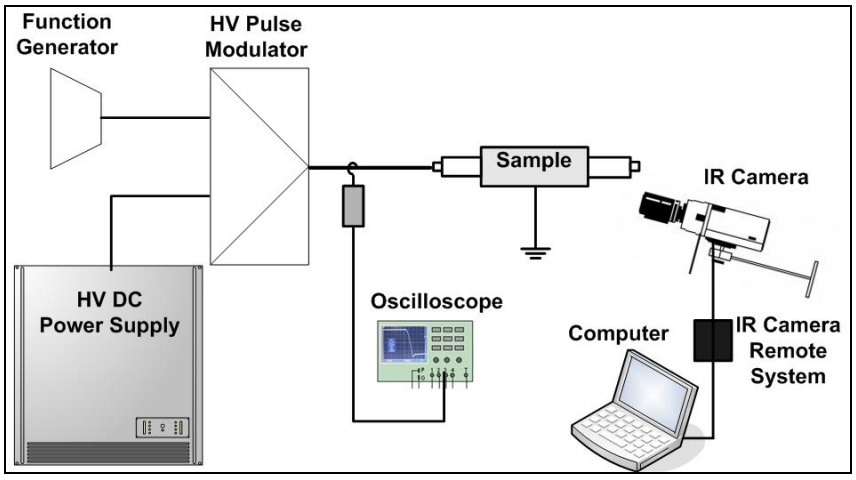

Figure 2-9: Experimental setup for infrared thermography of the bar sample when it is energized by repetitive fast pulses.

2.4.6 Qualification and Acceptance Tests

According to IEC/TS 60034-18-42 [4], Type II electrical insulation systems for machines fed from converter drives must be evaluated in two stages. The first stage is the qualification of the groundwall insulation, the turn insulation, and the SG systems. Qualification testing is performed in order to qualify the materials, design rules, and processing of an insulation system with respect to its effectiveness in resisting PD or surface discharge in a winding under a given set of stresses resulting from repetitive fast pulses.

The second stage is an acceptance test of a specific design. This test, which is basically decided by commercial agreement between the purchaser and the motor manufacturer, consists of evaluating the 50 Hz or 60 Hz voltage endurance [125].

2.4.6.1 Pulse Aging Test

Qualification testing has been divided into separate test procedures in order to simulate the interactions between the various insulation components of Type II electrical insulation systems when they are exposed to repetitive fast pulses. One series of tests are to establish the life curves of the main and turn insulation of the windings of the drive duty motors. Another series of tests

are to establish that the stress grading and slot corona protection systems are suitable for service [4]. The latter series is within the scope of this research and, for the purpose of this study, is called the pulse aging test. Figure 2-10 depicts the pulse aging setup.

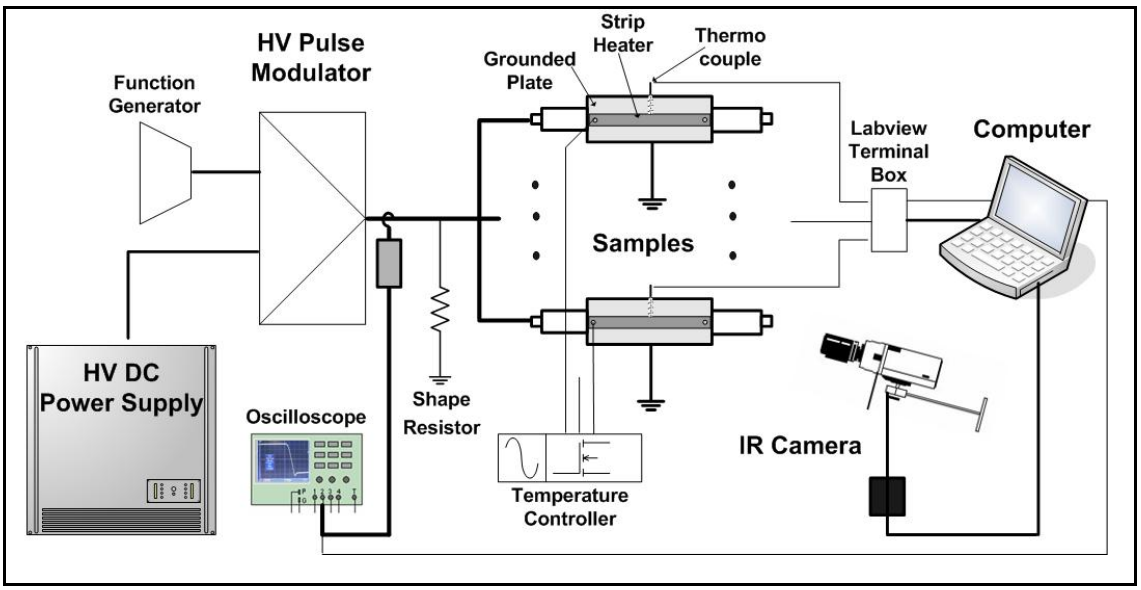

Figure 2-10: Schematic representation of the setup employed for the pulse aging test.

Pulse Generator

The pulse generator used was a high voltage pulse modulator (HVPM), developed by DTI [126]. This 30kV-30A voltage source modulator is built with solid-state switches in series, thus providing a high peak power and constant voltage during each pulse. Figure 2-11 illustrates the internal circuit of this modulator. A negative dc power supply and a function generator supply the pulse modulator. A dc source with a variable voltage of 0 to -30 kV was provided by a Glassman SH30R540 dc power supply with a limit for continuous operation of 540 mA. The voltage is varied by a dial indicator on the front panel. An Agilent 33220A function generator generated the gate signals for the IGBT switch module through the pulse trigger input (TTL). The pulse repetition frequency (PRF) of the output voltage could be varied up to 10 kHz by using the function generator. However, the maximum pulse width of the pulses is limited to 10 μs.

To prevent overheating of the modulator and possible damage, the operating voltage, load current, PRF, and duty cycle must fall within all the safe operating area graphs provided by the manufacturer. In addition, the PRF, the duty cycle, the rise time, and the fall time all are highly influenced and limited by the load characteristics.

Since the loads used in this study were inherently capacitive, the decay time for discharging ($\cong RC$) was too long compared to the pulse period. Thus, to shape the output voltage, suitable

external high voltage pull down resistors were required. However, because the maximum pulse width of the HVPM is 10 μs, independent of function generator pulse widths, the switches go off after 10 μs. In other words, for pulse repetition frequency up to 10 kHz (the modulator rating), the pulse shape is degraded to impulse shape (exponential decaying), as shown in Figure 2-12.

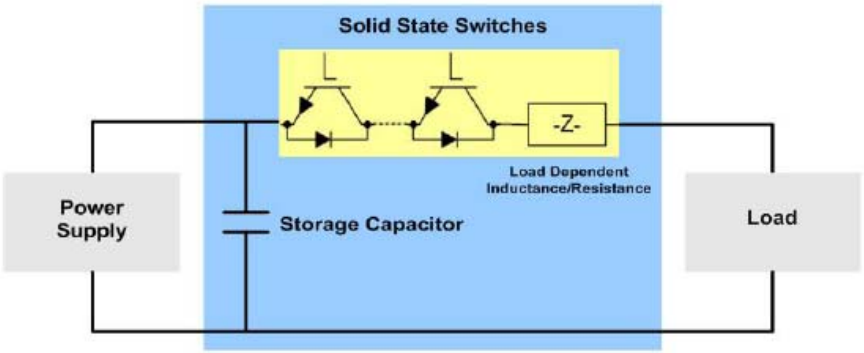

Figure 2-11: Internal circuit diagram of the HVPM used for the pulse aging test [126].

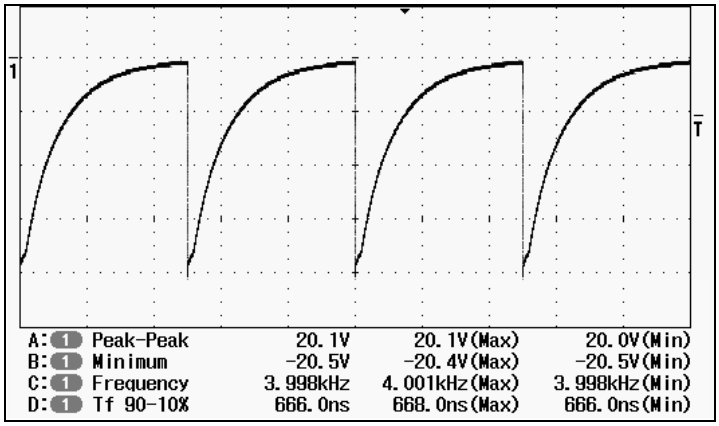

Figure 2-12: Voltage waveforms at the pulse generator output.

The pulse rise time, $1.25 \times (t_{90} - t_{10})$ [4, 93], depends on the modulator design and the load characteristics and is, on average, 625 ns, which is a reasonable value for most modern converter output voltage rise times [4, 127]. In addition, the pulse fall time depends strongly on the load characteristics, i.e., the impedance of samples and the shape resistor. In the setup used in this study, the fall time is about 100 μs. The polarity is negative and fixed (unipolar), and the effect of changes in polarity is outside the scope of this study.

Because the voltage rating of the samples, as introduced in section 2.2, is 13.8 kV (phase-to-phase), the peak and peak-to-peak of the phase-to-ground voltage for the PWM drive duty motors in service were assumed to be 15 kV and 30 kV respectively (Appendix A). To meet the requirements for the pulse aging test in [4], values of 20 kV and 25 kV for the peak of the pulses

and 4 kHz and 5 kHz for the pulse repetition rates were adopted. These values of pulse voltages and pulse repetition rates with pulse rise times averaging 625 ns produce stresses in the moderate category of stress classification for Type II insulation systems [128, 129].

Control and Monitoring

Forced heat was generated by strip heaters mounted on the grounded plates and acting as simulated motor slots. Since the temperature rise due to the application of the repetitive pulses acts as on extra thermal stress, the heaters are controlled to have 155 ˚C on the surface at the middle of the samples at no voltage. This amount of heat was fixed after the samples were energized. The temperature was measured by thermocouples at two points was recorded along with the voltage peak using Labview® software.

Test Procedure

The pulse aging tests were carried out on five samples with each SG system: nonlinear resistive or capacitive. The samples were subjected to at least a 100 h pulse aging test at a fixed 155 ˚C forced heat corresponding to thermal class F, using the setup depicted in Figure 2-10. As shown, the pulse generator is first adjusted for a 20 kV peak and a 4 kHz pulse repetition rate and the test is run for 100 hours. If all samples pass the test, the test is repeated with the same conditions for another 100 h. If failure still does not occur and no damage is observed, severe stresses are applied using 25 kV and 5 kHz pulses. As a diagnostic test, after each aging stage, the level of partial discharge (PD) is measured, and the PD pattern is recorded for further analysis.

During the aging test, the surface corona activity was periodically checked in a dark room and with a corona camera. The surface temperature along the end portions of the samples was scanned for temperature hot spots using infrared thermography, as described in section 2.4.5.

2.4.6.2 Partial Discharge Measurement

Measuring partial discharge (PD) is one the most important tests for the condition assessment of high voltage insulation systems. Although this test is not recommended by IEC TS 60034-18-42 [4] for the evaluation of the SG systems during the pulse aging test, it is used in this study in order to analyze the PD trend due to aging in the insulation system, particularly for the samples with foils embedded within the groundwall.

The PD setup consists of a 0-150 kV/20 kVA ac dielectric test set (Hipotronics 7150-20AM-AX-G) with a PD level < 2 pC and a PD Detector (Hipotronics, DDX 9101). This setup, with low noise background in the laboratory (less than 3 pC) meets all the IEC and ASTM standard

requirements [130, 131]. With respect to very low PD level of the ac dielectric test set, it is used as a power source for the partial discharge setup. The main components of the test system are a test transformer, regulator, calibration capacitor, control unit, and coupling capacitor. The DDX 9101 PD detector is one of the new generation of digital wide-band partial discharge detectors with the basic functions of an analog detector.

It is known that partial discharge causes erosion and treeing in insulation materials. However, for micaceous composites, this erosion is often suppressed by the high discharge resistance of mica crystals. Therefore, large partial discharge levels (>1000 pC) can be allowed in mica based insulation systems, such as groundwall, compared to what is permissible in other high voltage insulation systems [132, 133, 134]. A large number of partial discharges in conjunction with a long decay of the oscillating pulses may lead to a superposition of successive discharges in a narrow band PD measuring system. Wideband measuring systems are therefore typically used for taking partial discharge measurements on rotating machinery [132]. As pointed out earlier, the DDX 9101 is a wideband PD detector with lower and upper cut-off frequency ranges of $20 \leq f_1 \leq$ 80 kHz and $100 \leq f_2 \leq 500$ kHz. In this study, f_1 was adjusted to 30 kHz in order to suppress the main power frequency and its harmonics appropriately, and f_2 was set to 300 kHz. For every sample, the calibration was carried out with a 10 pC calibration level.

The detector has two display modes: PD meter and scope. In scope mode, the positions of the positive and negative zero crossings on the display are indicated. The sine, elliptical, and other scope display modes show the PD activity on a phase resolved display related to a high voltage cycle. The position of the PD pulses can indicate information about the source of the PD activities. However, the instantaneous data provides the information only at the time it is recorded. In other digital PD detectors, other quantities can be derived through pulse height analysis or pulse phase analysis. For example, by counting the pulses in each magnitude window of a pulse height analysis, additional useful quantities such as the normalized quantity number (NQN) can be extracted [135]. In addition, using 2D or 3D scatter plots with Φ-q-n patterns (phase, magnitude, and repetition within each phase/magnitude window), the source of the PD can be identified more accurately than with the traditional phase resolved display [132].

The PD inception voltage (PDIV) and extinction voltage (PDEV) are two other important parameters that are normally used for the condition assessment of insulation. They are related to a specific low threshold value of a PD magnitude that was assumed to be 90 pC for this study [136]. The following procedure was used for the PD measurement, which corresponds to the manufacturer's instructions. The PD level or maximum PD Q_{max} [134] was measured four times

sequentially: immediately after applying the nominal phase-to-ground voltage V_{pn} (8kV), at $1.2V_{pn}$ (9.66 kV), after 5 minutes at $1.2V_{pn}$, and again at V_{pn} [137]. In addition, in scope mode, the sine and elliptical displays of the PD activities were recorded for further analysis.

2.5 Computational Methods and Modelling

This section first introduces the methods for precise modelling of the electric and thermal fields in SG systems under PWM pulse or high frequency voltages either with nonlinear resistive materials or with a capacitive scheme that has conductive foils embedded in the groundwall insulation. Popular numerical methods for solving electromagnetic field equations are first reviewed, and then the truncated forms of Maxwell's equations are introduced. Analytical modelling of repetitive fast pulses for further signal analysis is also presented.

2.5.1 Finite Element Method (FEM) Analysis

In recent decades, the development of computer processors has opened up new possibilities for electromagnetic computation that can show the interaction of electromagnetic and thermal fields with complicated physical objects and the environment. Finite difference (FD) and finite element (FEM) methods are two numerical computational techniques that are widely used for solving partial differential equations (PDE) such as Maxwell's equations. These methods use a differential form of the governing equations and require the discretization (meshing) of the entire domain in which the electromagnetic fields are present. Each method has advantages, but FEM is the generally more attractive choice for complex electric field problems and geometries [23].

Electric fields may be described by truncated versions of Maxwell's equations applied to relatively long time scales and low frequencies (electro-quasi-static, EQS) as opposed to radio and microwave frequencies. In a quasi static condition, the device generally sees only a uniform time varying electric field. A SG system of motor coils may be considered an EQS problem because the physical size of the system is considerably smaller than the wavelength [138]. This multi-dielectric system, with the different insulation characteristics of isotropic or anisotropic conductive and semi-conductive nonlinear materials, is a complex system. In addition, in the case of a capacitive SG system, the floating thin layers of metal or conductive foil or tape embedded in main insulation intensify the complexity of the system. All these issues imply to have a powerful tool for precise modelling and simulation. This type of modelling enables the description or anticipation of the performance of the SG system under specific conditions or with the modification of material characteristics.

For the present work, COMSOL® Multiphysics version 3.5a FE software was used to compute the electric field, the potential, and the temperature along the SG. For this purpose, two main application modes can be used: electric quasi-static and heat transfer (conduction). In electric quasi-static mode, the coupling between the electric and magnetic fields (induced current) is neglected. In mathematical terms, where B is the magnetic field, the implication is

$$\nabla \times E = -\frac{\partial B}{\partial t} = 0 \tag{2-26}$$

which means that the electric field can be expressed only in terms of the electric potential ($\mathrm{E} = -\nabla \mathrm{V}$**).** Maxwell-Ampere equation also applies:

$$\nabla \cdot \nabla \times \mathrm{H} = \nabla .\, J_t = \nabla \cdot [J_c + \frac{\partial \mathrm{D}}{\partial \mathrm{t}}] \tag{2-27}$$

In this equation, J_t, J_c, D, and $\partial \mathrm{D}/\partial \mathrm{t}$ represent the total current density, conduction current density, electric displacement, and displacement current density, respectively. To meet the charge continuity condition, $\nabla .\, J_t = 0$. Based on Gauss' law ($\nabla .D = \rho$) and the constitutive relation ($D = \varepsilon_0 \varepsilon_r E = \varepsilon E$), the program solves (2-28) and (2-29) for the time harmonic and transient analyses, respectively [139]:

$$-\nabla \cdot ((\sigma + j\omega \varepsilon_0 \varepsilon_r) \nabla \mathrm{V} - \mathrm{J}^{\mathrm{e}}) = 0 \tag{2-28}$$

$$-\nabla \cdot \frac{\partial}{\partial t} (\varepsilon_0 \varepsilon_r \nabla \mathrm{V}) - \nabla .(\sigma \nabla \mathrm{V} - \mathrm{J}^{\mathrm{e}}) = 0 \tag{2-29}$$

where J^{e} is the external current density.

In these equations, the conductivity (σ) and relative permittivity (ε_r) can be a linear or nonlinear function of dependent parameters and can be either isotropic or fully anisotropic.

In addition, the thermal field problem can be solved using the same geometry and taking the ohmic losses or resistive heating from the electric solution as a source of heat. The general heat transfer application mode is based on a general energy balance:

$$\rho C_p \frac{\partial T}{\partial t} + \nabla .(-k \nabla T) = Q - \rho C_p u .\nabla T \tag{2-30}$$

where k represents thermal conductivity, C_p is the (temperature dependent) specific heat capacity, Q is the heating power per unit volume, ρ is the mass density, and u is the fluid velocity vector.

During steady state ($\partial T/\partial t = 0$) and if the velocity is set to zero (ignoring the convection), heat transfers through each subdomain to the surroundings through conduction according to

$$\nabla.(-k\nabla T)=Q \tag{2-31}$$

The approach to coupling multiple application modes is to use dependent variables. The coupling between the two physics is the resistive heat of each subdomain in the electric field module as heat source in heat transfer module. The heat source describes heat generation within the domain (W/m^3 in SI units).

After selecting appropriate models and drawing the geometry, meshing is one of the crucial problems associated with complex geometries. In this study, for the most of the simulations, interactive meshing was used to avoid failing to generate mesh in thin sub-domains with sharp edges. The interactive meshing environment provides the means to build a mesh in an incremental fashion where each meshing operation acts on a set of geometry domains. This makes it easier to control the distribution of elements and the size of the mesh [139].

2.5.2 Analytical Modelling of the Pulses

Figure 2-13 shows an expanded view of a single square wave pulse voltage in a train of pulses. The pulse rise time (t_r), overshoot, and fall time (t_f) are functions of the switching devices, the feeder cable, and the load impedance characteristics. Figure 2-14 also shows a single impulse voltage in a train of impulses.

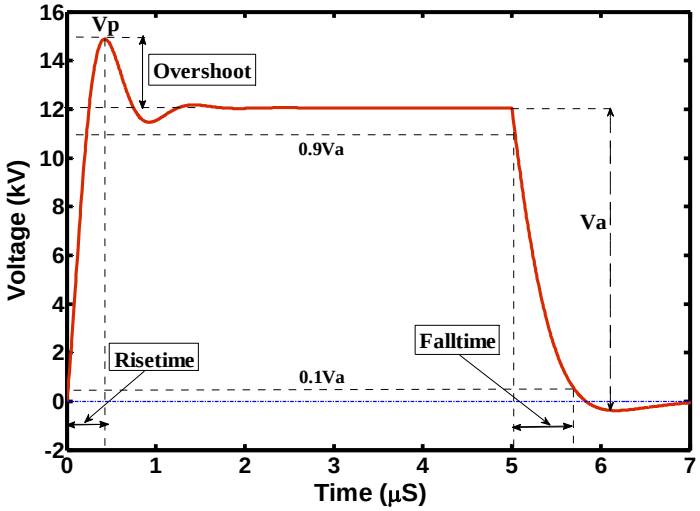

Figure 2-13: Expanded view of a single square wave pulse in a train of pulses: $t_r = (t_{90} - t_{10})_r \times 1.25$ [4], $t_f = (t_{90} - t_{10})_f$

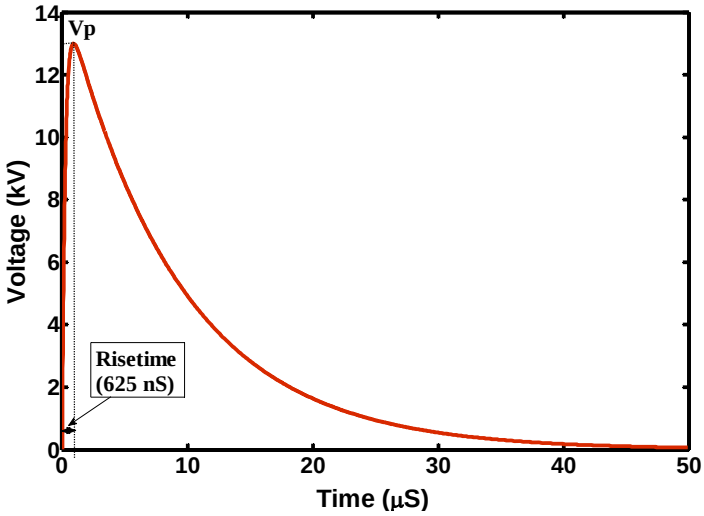

Figure 2-14: A typical impulse in a train of impulses: $t_r = (t_{90} - t_{10})_r * 1.25$, $t_f = (t_{90} - t_{10})_f$

All periodic stationary signals can be represented by a Fourier series expansion. The frequency spectra of the measured impulse and the square wave voltages are shown in Figure 2-15.

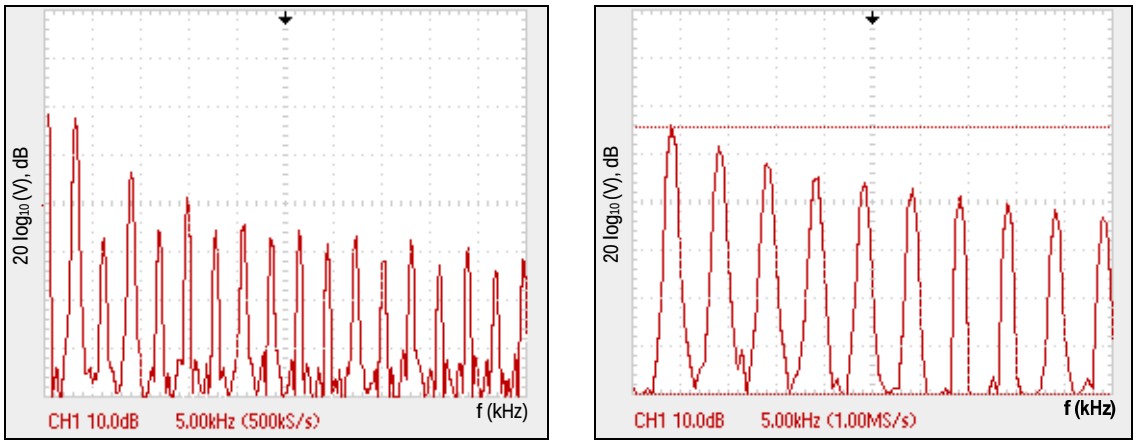

(a) (b)

Figure 2-15: Frequency spectrum of the train of measured (a) unipolar square wave pulses indicated in Figure 2-13 and (b) impulses indicated in Figure 2-14, as captured by the scope.

Due to the periodicity of the signals, all the harmonics are integer multiples of the switching frequency. The Fourier series of a periodic signal $v(t)$ with a period T and $\omega = 2\pi/T$ is as follows:

$$v(t) = V_{dc} + \sum_{k=1}^{\infty} V_k \cos(k\omega t + \varphi_k) = V_{dc} + \sum_{k=1}^{\infty} V_k \sin(k\omega t + \psi_k) \qquad (2\text{-}32)$$

where, $V_{dc} = \frac{1}{T}\int_0^T v(t).dt$, $V_k = \sqrt{(a_k^2 + b_k^2)}$, $\varphi_k = -\tan^{-1}\left(\frac{b_k}{a_k}\right)$, $\psi_k = \varphi_k + \frac{\pi}{2}$

$$a_k = \frac{2}{T}\int_0^T v(t).cos(k\omega t)dt \ , \ b_k = \frac{2}{T}\int_0^T v(t).sin(k\omega t)dt$$

To conduct the analytical studies, the unipolar square wave pulses with the specific rise times, fall times, and overshoots indicated in Figure 2-13 are selected so that they can be formulated mathematically as two exponentially decaying sinusoidal equations:

$$v(t) = \begin{cases} V_0.(1-\exp(-\xi_1.t).\cos(\omega_{d1}.t)) & : 0 \le t \le t_d \ \ (rise-time) \\ V_0.\exp(-\xi_2.(t-t_d)).\cos(\omega_{d2}.(t-t_d)) & : t_d \le t \le T \ \ (fall-time) \end{cases} \quad (2\text{-}33)$$

The damped ratios (ξ_1 *and* ξ_2), damped frequencies (ω_{d1} and ω_{d2}), and time to fall (t_d) are found according to the rise time (t_r), the fall time (t_f), the overshoots, and the duty cycle.

The harmonic component amplitudes of the unipolar square wave pulses can then be found using equations (2-32) and (2-33). The results for one case are shown in Figure 2-16. In this case t_r = 625 ns, t_f = 31µs, (ξ_1 *=2.84e6), (*ξ_2 *=4.00e4), (*ω_{d1}*=4.05e6), and (*ω_{d2} *=4.45e4)*. The frequency spectrum excludes the even harmonics for ideal square wave pulses with a 50 % duty cycle. However, in Figure 2-16, the even harmonics are evident. A comparison of this result with that shown in Figure 2-15 (a) verifies the accuracy of the analytical method developed in this study. These even harmonics nearly disappear in Figure 2-17, which shows the results that are produced when the fall time is much faster.

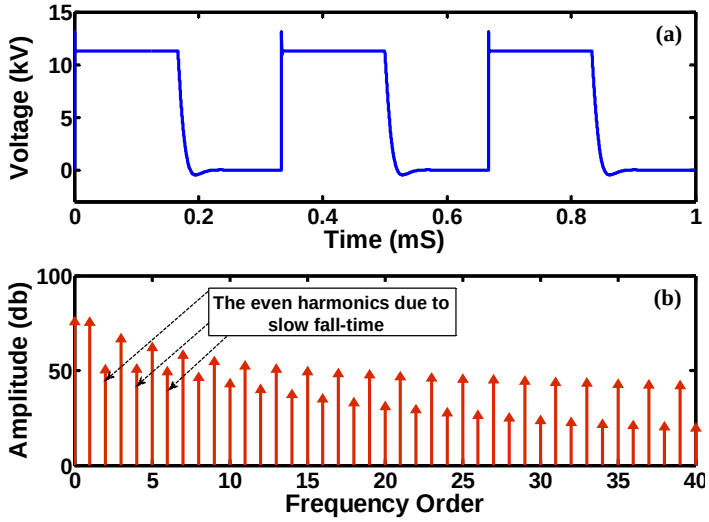

Figure 2-16: Unipolar square wave train (a) and corresponding frequency spectrum (b); simulation with duty cycle = 50 %, t_r = 625 ns, t_f = 31µs.

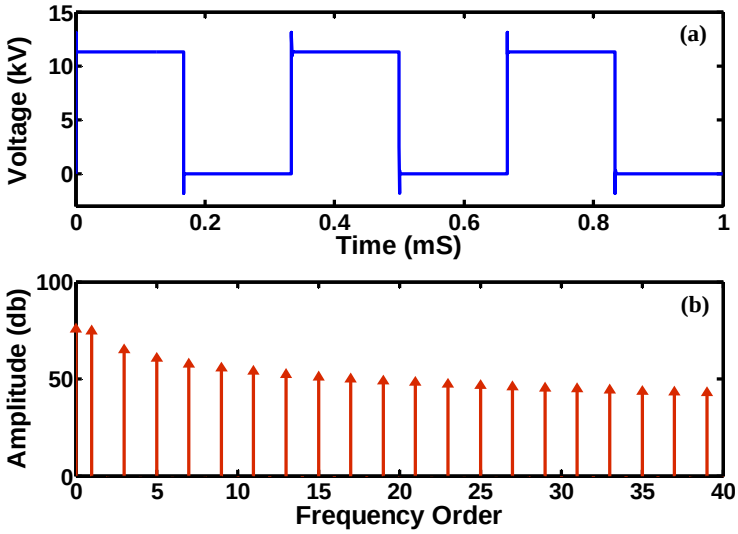

Figure 2-17: Unipolar square wave train (a) and corresponding frequency spectrum (b); simulation with duty cycle = 50 %, t_r = 625 ns, t_f = 0.5 µs.

Similarly, for impulse signals with the specific rise and fall times indicated in Figure 2-14, a double exponential impulse equation can be used:

$$v(t) = V_0 . \left(\exp(-c_1 . t) - \exp(-c_2 . t) \right) \tag{2-34}$$

Figure 2-18 shows the frequency spectrum of this pulse for a sample case that is matched with the spectrum whose measurements are shown in Figure 2-15 (b).

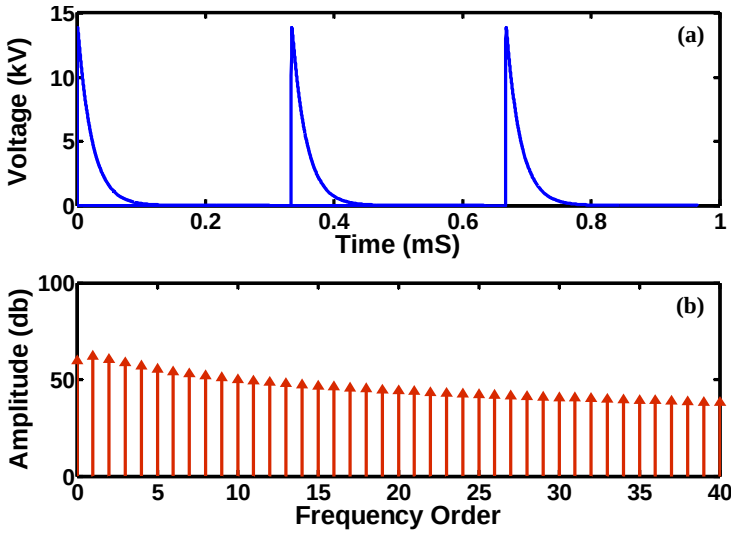

Figure 2-18: Impulse train (a) and corresponding frequency spectrum (b); simulation with t_r = 625 ns, t_f = 100 µs.

Signal Power

The total Joule and dielectric losses in a linear dielectric material exposed to a periodic voltage, as defined in equation (2-32), can be expressed as follows [140]:

$$P = \left(\frac{V_{dc}^2}{R_s} \right) + \sum_{k=1}^{\infty} V_{kr}^2 . k\omega_0 . C_k . \tan \delta_k \qquad (2\text{-}35)$$

where C_k and tan δ_k are the capacitance and the dissipation factor, respectively, at the harmonic n, R_s is the static resistance, and V_{kr} is the rms value of component k ($V_k = \sqrt{2}\ V_{kr}$).

It must be noted that this expression is not valid for materials with nonlinear V-I characteristics, such as SiC- or ZnO-filled composites. In addition, for an actual multi-dielectric insulation system such as form-wound machine insulation, the dielectric materials, particularly the SGT and the CAT, have dielectric parameters that are normally dependent on frequency, electric field, and temperature. In other words, for each harmonic and in each subsystem, the appropriate dielectric parameters regarding the system geometry must be found and used in equation (2-35). This constraint gives rise to an impractical approach to calculating the electrical loss, and to overcome this problem, a novel approach was developed.

According to Parseval's theorem, the power of the signal expressed in equation (2-32) is as follows [141]:

$$P_v = \frac{1}{T} \int_0^T |v(t)|^2 . dt = V_{dc}^2 + \sum_{k=1}^{\infty} V_{kr}^2 \qquad (2\text{-}36)$$

For a conventional form wound insulation system, since the CAT behaves as a high-pass frequency filter [51], and the electric field associated with dc and the low frequency components is concentrated mainly in the SGT, the dielectric heating can be decomposed according to two heat sources. In other words, the signal power can be divided into two sections as follows:

$$P_v = \left(V_{dc}^2 + \sum_{k=1}^{n} V_k^2 \right) + \sum_{k=n+1}^{\infty} V_k^2 = P_{v1} + P_{v2} \qquad (2\text{-}37)$$

where P_{v1} and P_{v2} represent the signal power of lower and higher harmonic orders, respectively, and n is the harmonic order that identifies a threshold frequency (f_t).

In this decomposition, P_{v1} and P_{v2} can be assigned to the power losses in the SGT and the CAT, respectively. The threshold frequency corresponds to the CAT's dielectric characteristics. At this frequency, the dissipation factor of the CAT begins to decline rapidly. For the tape used in this

study, f_t is nearly 12 kHz [142]. Furthermore, two equivalent sinusoidal signals can be assumed, with a frequency and amplitude (f_1 , A_1) and (f_1 , A_2) corresponding to P_{v1} and P_{v2}, respectively, so that the following conditions are fulfilled:

$$A_1 = k_1 \cdot \sqrt{P_{v1}} \quad , \quad A_2 = k_2 \cdot \sqrt{P_{v2}} \tag{2-38}$$

where k_1 and k_2 are two empirical constants that are due to the nonlinearity of the materials and the power of the signal.

The frequency f_1 is equal to the signal repetition rate (switching frequency). However, f_2 can be assumed to be a fixed frequency that represents the high-frequency components. In this study, f_2 = 50 kHz was selected based on the experimental tests.

Chapter 3
Results

3.1 Introduction

Using the test procedures described in Sections 2.2 and 2.3, the experimental setups explained in Section 2.4, and the methodology for modelling presented in Section 2.5, the performance of conventional stress grading (SG) and the proposed capacitive SG systems were evaluated for both power frequency and repetitive fast pulse applications.

The dielectric properties of the SG materials as a function of the electric field at DC, 60 Hz, and high frequency voltages were measured in order to provide an understanding of their behaviour with different applications and also to enable precise modelling of the systems. The results show that some phenomena cannot be represented with traditional modelling using isotropic DC properties.

To evaluate the performance of SG systems at 60 Hz and elevated temperatures, the tangential electric field along the SG system, which is one the most important factors, was calculated through the measurement of surface potential. The components of the electric field were simulated using FEM modelling, and the output was compared with the experimental results. The thermal stress on conventional SG system and the proposed capacitive SG system subjected to repetitive fast pulse and high frequency sinusoidal voltages were studied. The effects of the pulse characteristics on the development of thermal stresses were explored. Two high frequency sinusoidal voltages were determined to be equivalent to the repetitive fast pulses that produce the same thermal stress on a conventional SG system. Using this equivalency, 2D and 3D coupled electro-thermal FEM simulations were performed. The quality of the conventional SG and the proposed capacitive grading were evaluated through qualification tests according to the recently published IEC technical specification [4].

3.2 Material Properties

For many years, either the dc volume conductivity in the thickness direction only or the surface conductivity of conductive armour tape (CAT) and stress grading tape (SGT) has been used for analysis of an SG system. However, in this study both the dc and the ac dielectric parameters were measured in different directions: both longitudinal and thickness. The configurations of the samples and the composition of the tapes are described in Section 2.2.

3.2.1 DC Resistivity

The dc resistivity of the CAT and the SGT at both room and elevated temperatures and with an I-V measurement were obtained using the setup described in Section 2.4.1. Since the tapes were thermal class F, the maximum temperature was set to 155 °C. All measurements at elevated temperatures were taken following a thermal cycle procedure. The thermal cycle scenario used for these tests is shown in Figure 3-1. To obtain stabilized data, the samples were kept at each temperature for at least 2 hours. The data were collected during both rising and falling temperatures. The latter showed consistent trends and were used as the final data for each temperature.

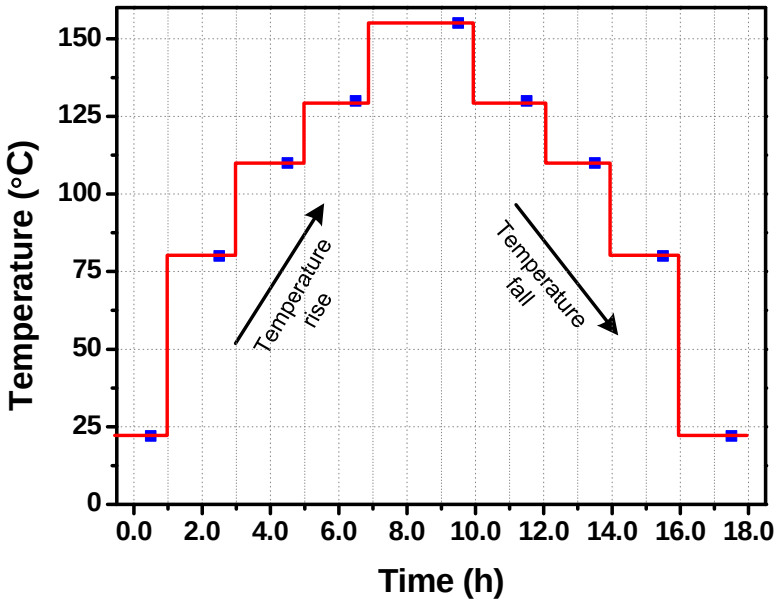

Figure 3-1: Thermal cycle scenario used for measuring the surface and volume resistivities.

Figure 3-2 shows the variation in the volume resistivity of the CAT as a function of the voltage and temperature. Due to the low resistivity of the tape, the measurements were taken at a low voltage. As expected, the resistivity of the coating did not change significantly with the voltage, and a constant value at each temperature can be assumed. For example, at 22 °C, the volume resistivity varies in a range of 0.63 - 0.68 Ω.m that is equivalent to an average volume conductivity of 1.53 S/m. In addition, since the thickness of the coating after taping and VPI process is about 0.4 mm, an average of 1640 Ω/sq can be assumed for the surface resistivity of the CAT after manufacturing at room temperature.

The dc volume resistivity of the CAT in the thickness direction at different temperatures was also measured separately and found to be about 320 Ω.m, which is much higher than the resistivity in the longitudinal direction.

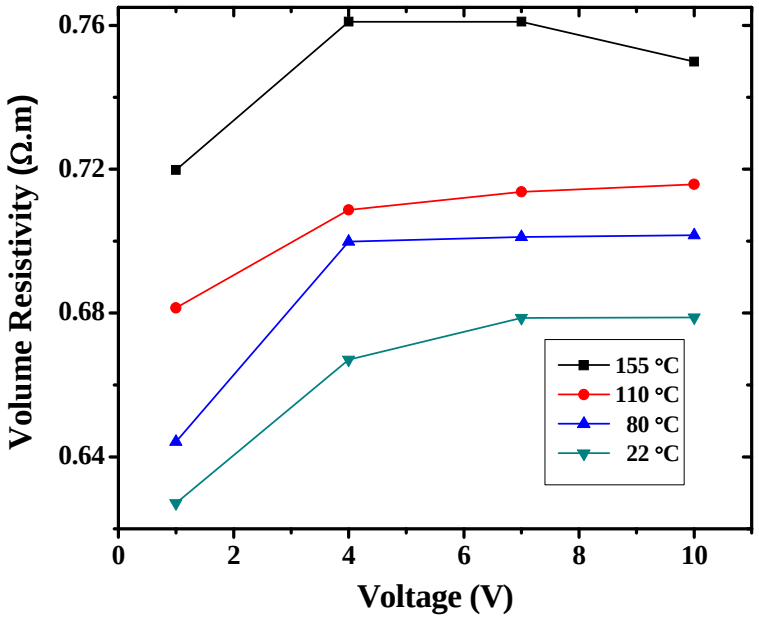

Figure 3-2: DC volume resistivity of the CAT as a function of voltage and at several temperatures.

The dc surface and volume resistivities of the SGT in longitudinal direction, measured at 22 °C, are shown in Figure 3-3 and Figure 3-4, respectively. The surface and volume resistivities of the nonlinear SGT as functions of electric field are described by the exponential relationships expressed in (3-1) and (3-2). The 2/3 exponent is in agreement with previously published work [52, 62].

$$\rho_{s-x}(E_x) = 6.25\times10^{11}\exp(-1.14\times10^{-3}E_x^{2/3})\Omega/sq \tag{3-1}$$

$$\rho_{v-x}(E_x) = 5.40\times10^{8}\ exp(-1.12\times10^{-3}E_x^{2/3})\ \Omega.m \tag{3-2}$$

The measured volume resistivity of the SGT at several temperatures was plotted as shown in Figure 3-5. These results show that temperature has a significant influence on the resistivity of the tape so that, for a low electric field, it has a negative thermal coefficient. However, the temperature coefficient becomes positive for fields above 450 kV/m. Measurements above 500 kV/m could not be taken, and it is therefore assumed that the resistivity follows the trend shown in the figure.

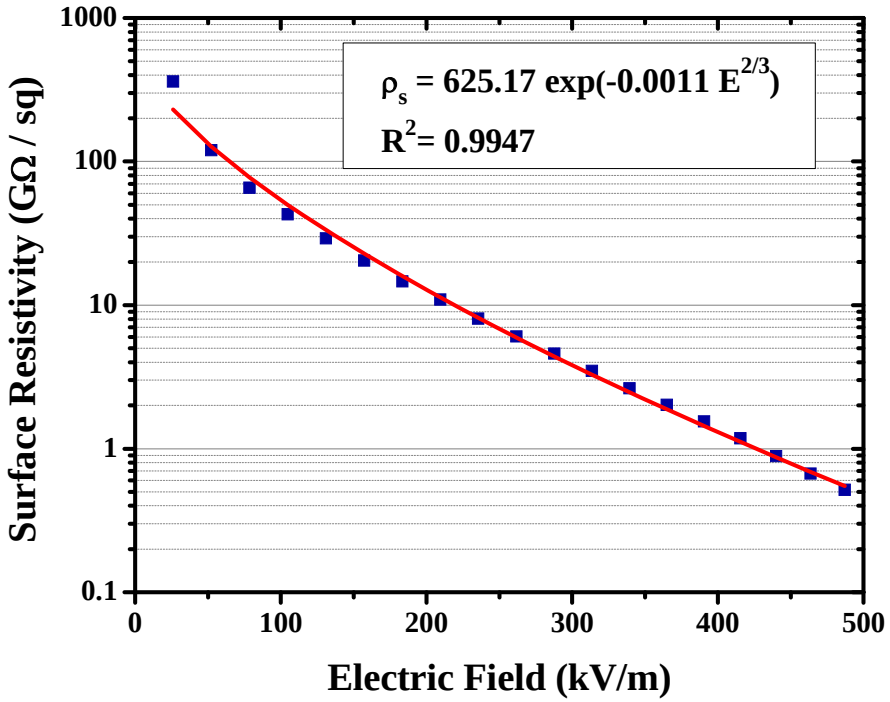

Figure 3-3: DC surface resistivity of the SGT in the longitudinal direction as a function of the electric field and at 22 °C.

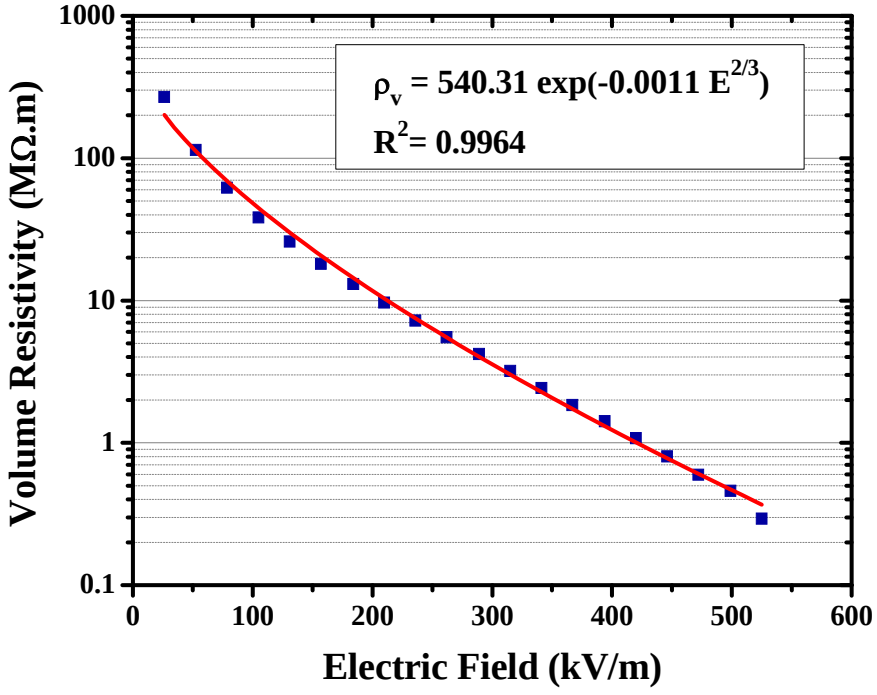

Figure 3-4: DC volume resistivity of the SGT in the longitudinal direction as a function of the electric field and at 22 °C.

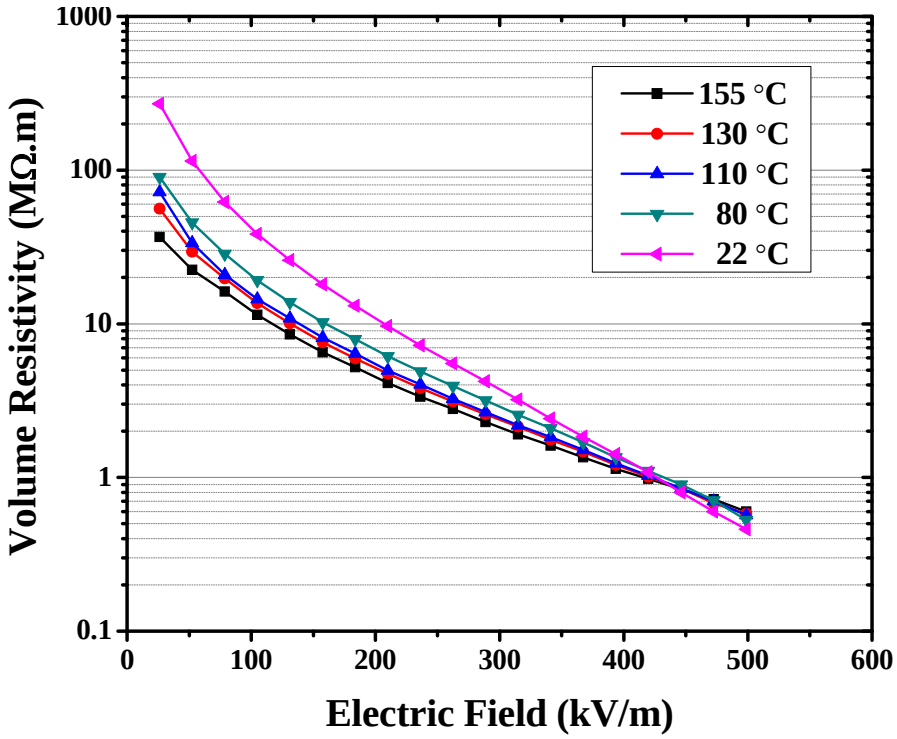

Figure 3-5: Variation in the dc volume resistivity of the SGT in the longitudinal direction as a function of the electric field and at several temperatures.

3.2.2 AC Dielectric Parameters

Sections 2.3 and 2.4.2 describe the technique and the setup used for measuring the ac dielectric parameters. These measurements were taken at room temperature (20°C).

3.2.2.1 Conductive Armour Tape

According to the measurements, it was discovered that the volume conductivities of the CAT in both the longitudinal and the thickness directions are essentially invariant with the electric field, and therefore can be considered field independent. The effect of frequency on the CAT dielectric properties in both directions was also studied. The variation of the CAT volume conductivity and tan δ with frequency up to 2 MHz is shown in Figure 3.6.

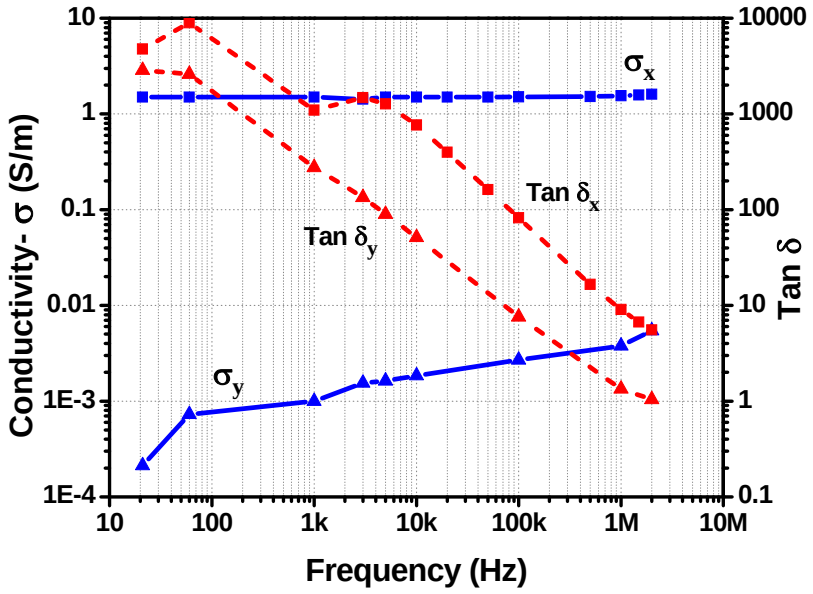

Figure 3-6: Conductivity and Tan δ of the CAT in the longitudinal (X) and thickness (Y) directions as a function of frequency.

3.2.2.2 Stress Grading Tape

Using the setup shown in Figure 2-5, the voltage and current of the SG tape were recorded in order to extract the ac dielectric properties. The voltage across the tape is almost purely sinusoidal (ignoring the nonlinearity of HF transformer), while the current is greatly distorted and contains harmonics. Figures 3-7 and 3-8 show the voltage and the current of the SG sample at 60 Hz and at room temperature. At 60 Hz and low electric field, the SG current is highly distorted. However, as shown in Figures 3-9 and 3-10, at high frequency voltages, the current distortion decreases significantly.

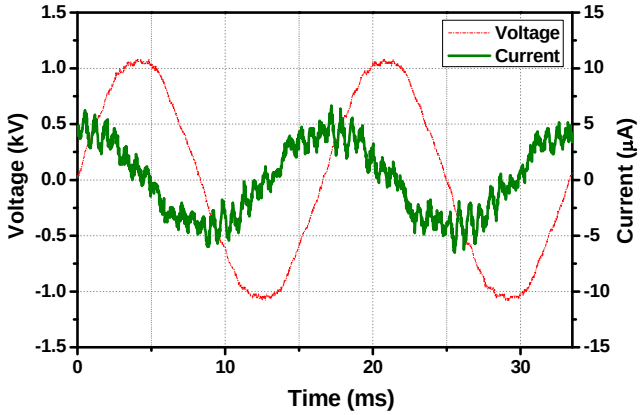

Figure 3-7: The voltage and current waveform of the SG sample in the longitudinal (x) direction at low electric field, 60 Hz, and room temperature.

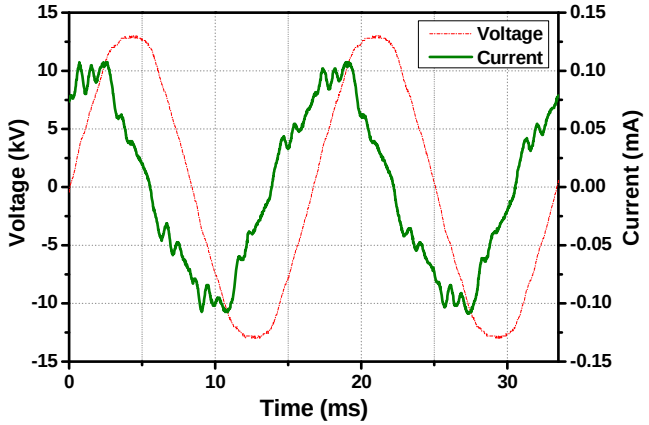

Figure 3-8: The voltage and current waveform of the SG sample in the longitudinal (x) direction, at high electric field, 60 Hz, and room temperature.

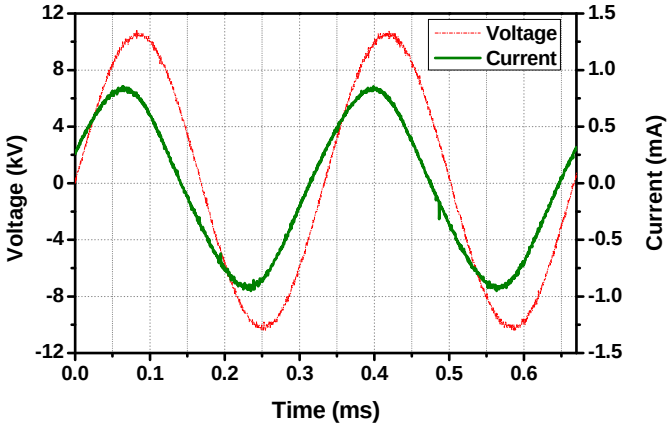

Figure 3-9: Voltage and current waveform of the SG sample in longitudinal (x) direction, at high electric field, 3 kHz, and room temperature.

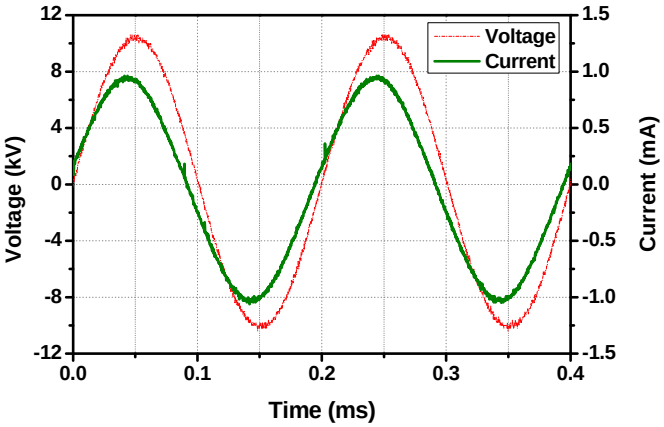

Figure 3-10: Voltage and current waveform of the SG sample in longitudinal (x) direction, at high electric field, 5 kHz, and room temperature.

From the recorded voltage and current data, and according to the signal processing method described in Section 2.3.2, the conductivity and dissipation factor of the SGT were extracted. Figure 3-11 shows the dc and ac volume conductivities in the longitudinal direction. As can be observed, the variation in conductivity with the electric field under dc is higher than that produced under ac. Moreover, the difference between the dc and ac conductivity decreases at higher electric field. AC measurements above 400 kV/m could not be performed due to the limitation of the power amplifier. It is therefore assumed that the conductivity follows the trends shown in Figure 3-11.

The effects of frequency and electric field on the dissipation factor are shown in Figure 3-12. The dissipation factor shows a direct relationship to both the electric field and the frequency. When the frequency increases, the loss factor of the SGT also increases, which means that the tape is more resistive at higher frequencies up to 5 kHz. Figures 3-13 and 3-14 show the variation in the conductivity and the dissipation factor of the SGT in the thickness direction with the electric field and the frequency.

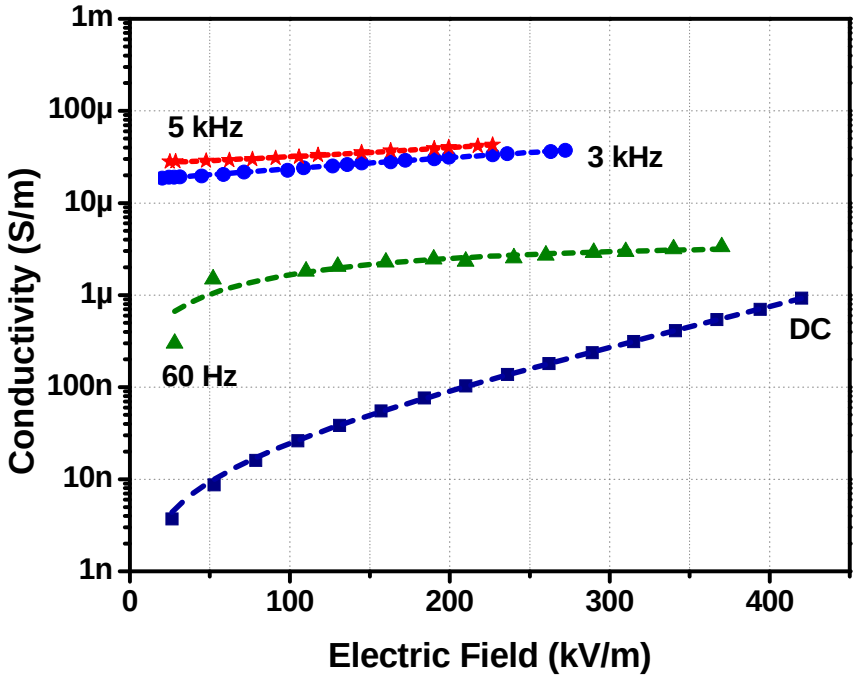

Figure 3-11: Conductivity of the SGT in the longitudinal (X) direction as a function of the electric field at several frequencies.

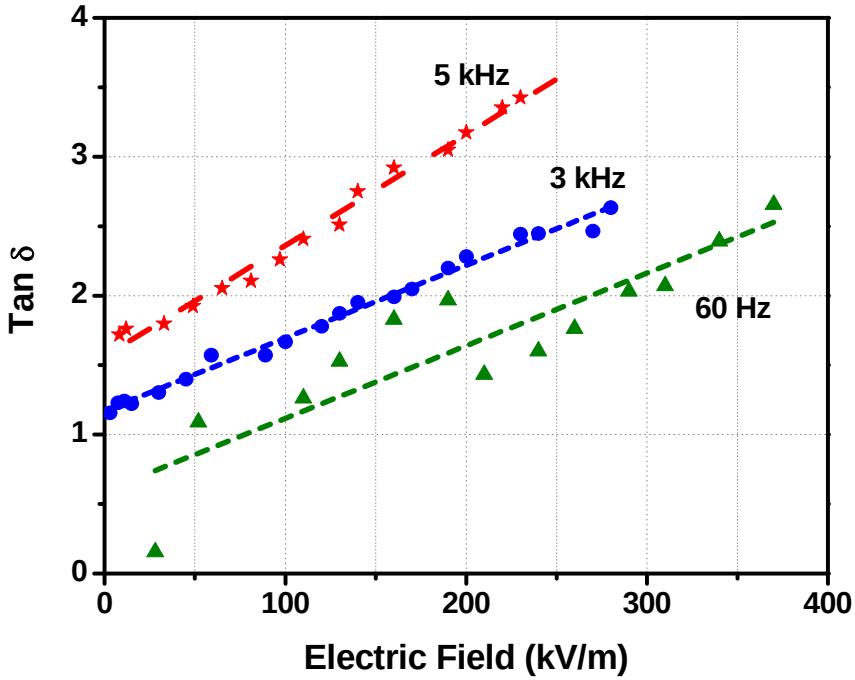

Figure 3-12: Dissipation factor of the SGT in the longitudinal (X) direction as a function of the electric field at several frequencies.

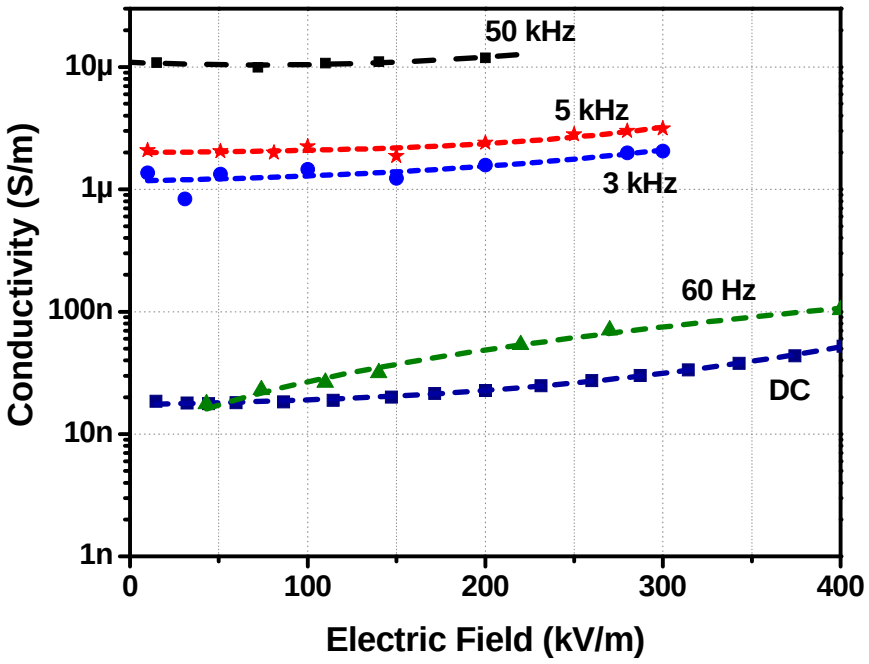

Figure 3-13: Conductivity of the SGT in the thickness direction (Y) as a function of the electric field at several frequencies.

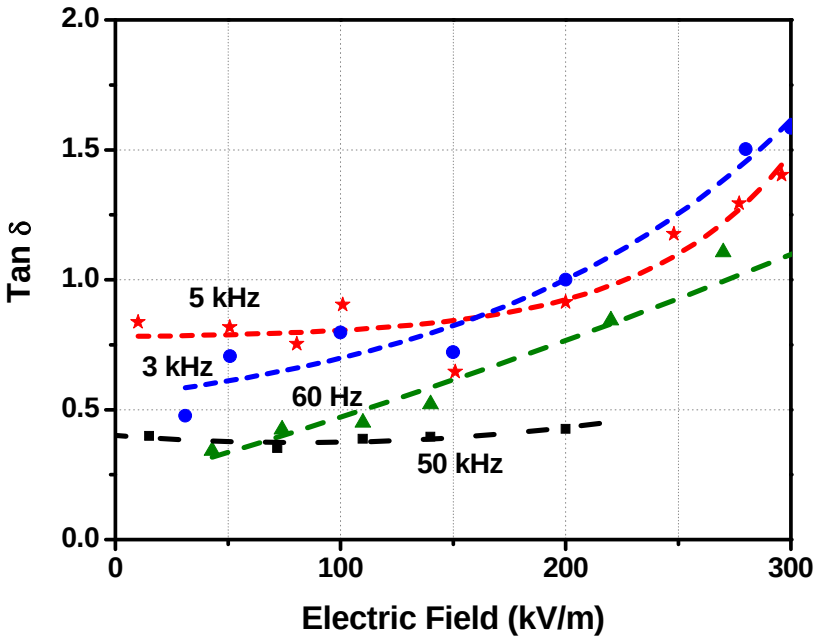

Figure 3-14: Dissipation factor of the SGT in the thickness direction (Y) as a function of the electric field at several frequencies.

3.2.3 Thermal Conductivity

The thermal resistance of groundwall tape, CAT, and SGT as a function of thickness are illustrated in Figure 3-15, the values for which were obtained using the method explained in Section 2.4.3.

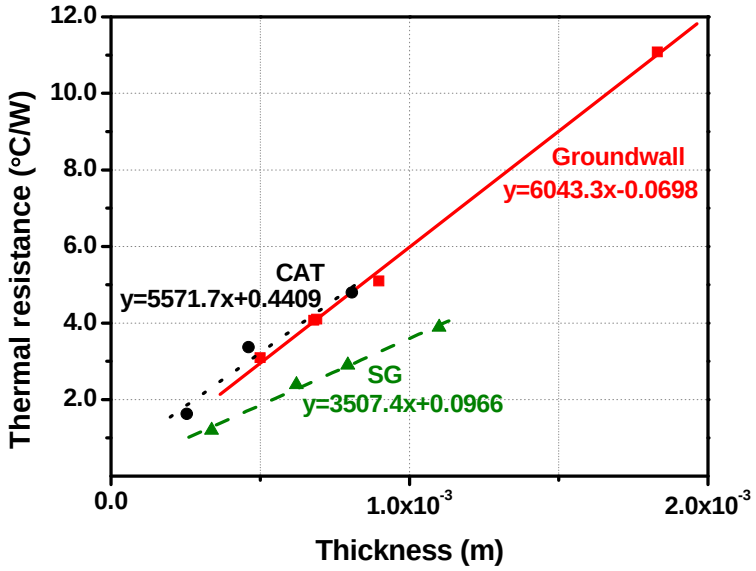

Figure 3-15: Thermal resistance of the groundwall tape, CAT, and SGT plotted as a function of thickness.

The thermal resistance is nearly a linear function of the thickness of the tape. When a line is fitted to the measured data, a linear function y= ax + b can be extracted, where b is the y-intercept and represents the contact resistance. With respect to (2-25), the thermal conductivity is the inverse of (a.A), where A is the area of the test sample and a is the slope of the linear function of the thermal resistance plotted against the thickness. Using this method, the thermal conductivities of the groundwall tape, CAT, and SGT are 0.26, 0.29, and 0.46 W/(m.˚K), respectively.

3.3 Electric Field Profile along SG System

The performance of an SG system on form-wound motor coils is evaluated with its ability to control the electric field below the breakdown strength of the surrounding media. In this section, the experimental and computational results that indicates the electric filed profile along the conventional and the proposed capacitive SG systems are presented.

3.3.1 Conventional SG System

3.3.1.1 Measurement of the Surface Potential and the Electric Field Profile at 60 Hz

Using the setup introduced in Section 2.4.4, the surface potential was measured along the surface of the bar sample at three temperatures as shown in Figure 3-16. It can be observed that the surface potential increases slightly at 90 °C. Figure 3-17 shows the corresponding electric fields extracted from the surface potentials.

To observe the dependency of the electric stress of the CAT and SGT, the applied voltage was changed from 12.5 % to 130 % of the nominal 8 kV_{rms} voltage. The results at several temperatures are shown in Figures 3-18, 3-19, and 3-20.

Due to the method adopted in this study of measuring the surface potential, this electric field is only the tangential component along the surface of the sample. In fact, the tangential component is expected to be the major electric field component along a homogeneous CAT and SGT. However, because these layers are not homogeneous and uniform, particularly at overlaps, the normal of the electric field must be studied separately. Since measuring the normal component of the electric field is not straightforward, a 2D FEM simulation is an effective approach to the problem, as discussed in Section 3.3.1.3.

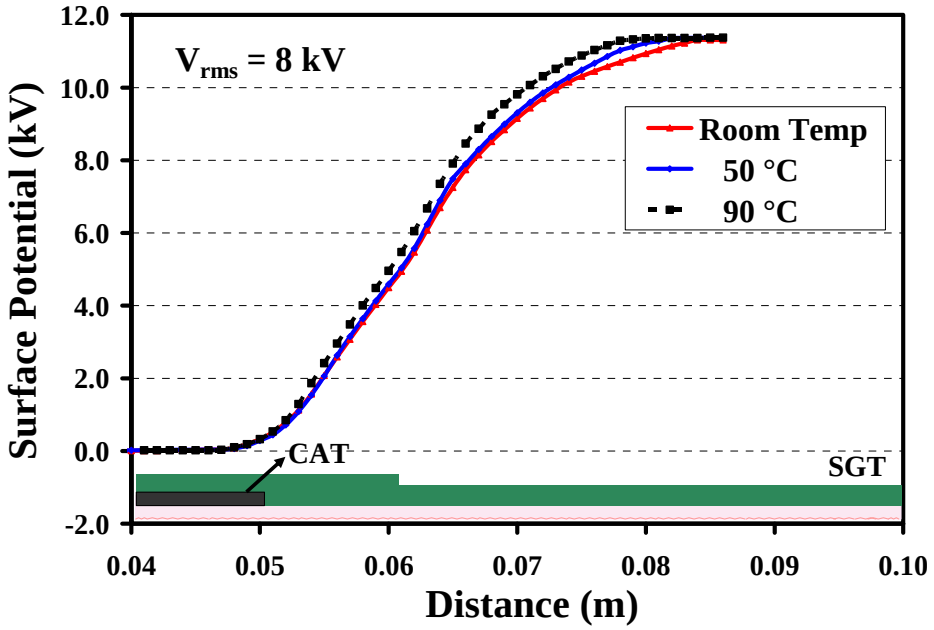

Figure 3-16: Peak surface potentials at 8 kV_{rms} nominal line-to-ground voltage, measured 2 to 4 mm above the surface of a bar sample, and at three temperatures.

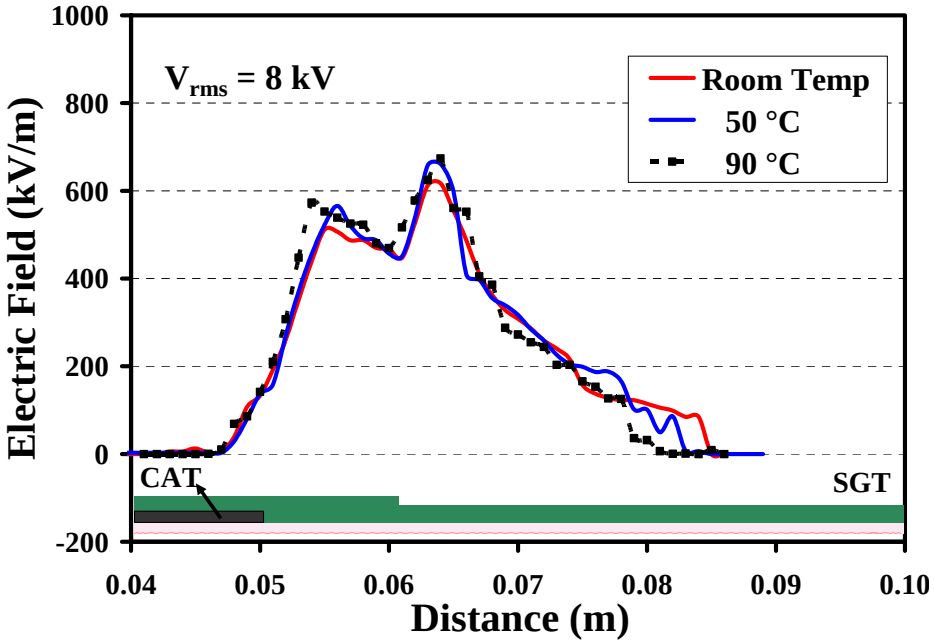

Figure 3-17: Tangential component of the surface electric field extracted from the measurements of the surface potential at 8 kV_{rms} and at three different temperatures.

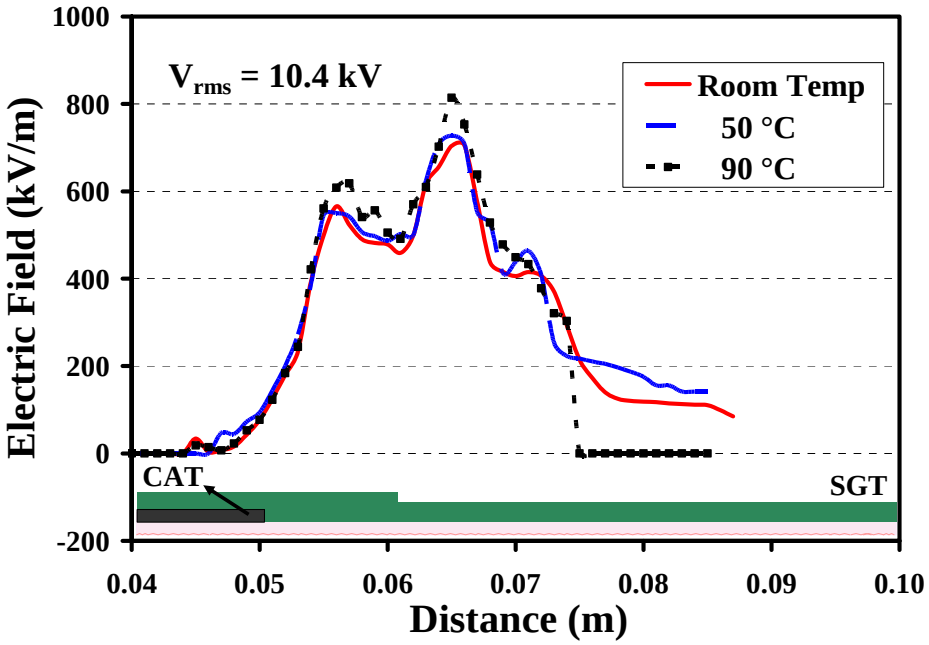

Figure 3-18: Tangential component of the surface electric field extracted from the measurements of the surface potential at 130 % nominal voltage and at three different temperatures.

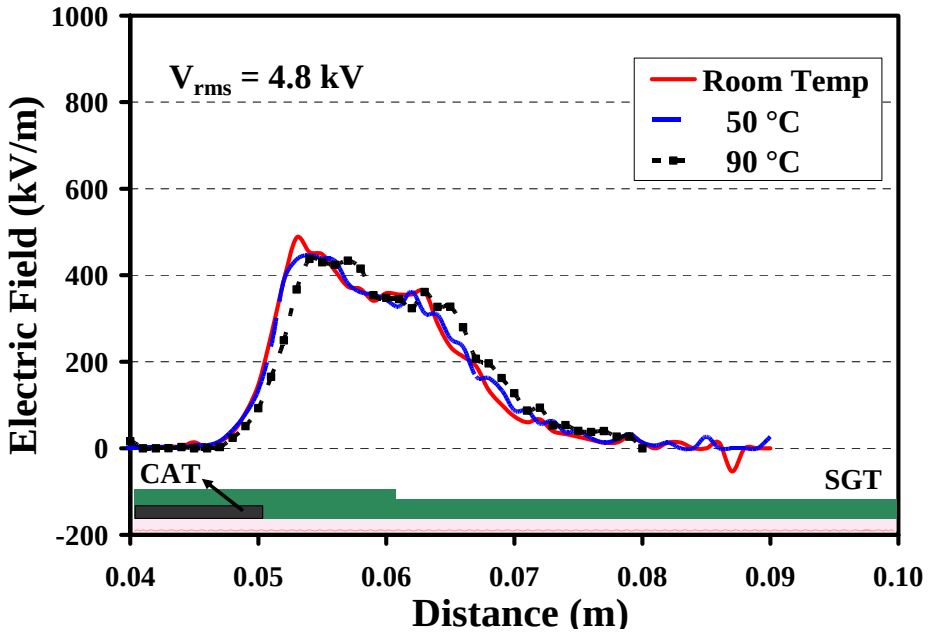

Figure 3-19: Tangential component of the surface electric field extracted from the measurements of the surface potential at 60 % nominal voltage and at three different temperatures.

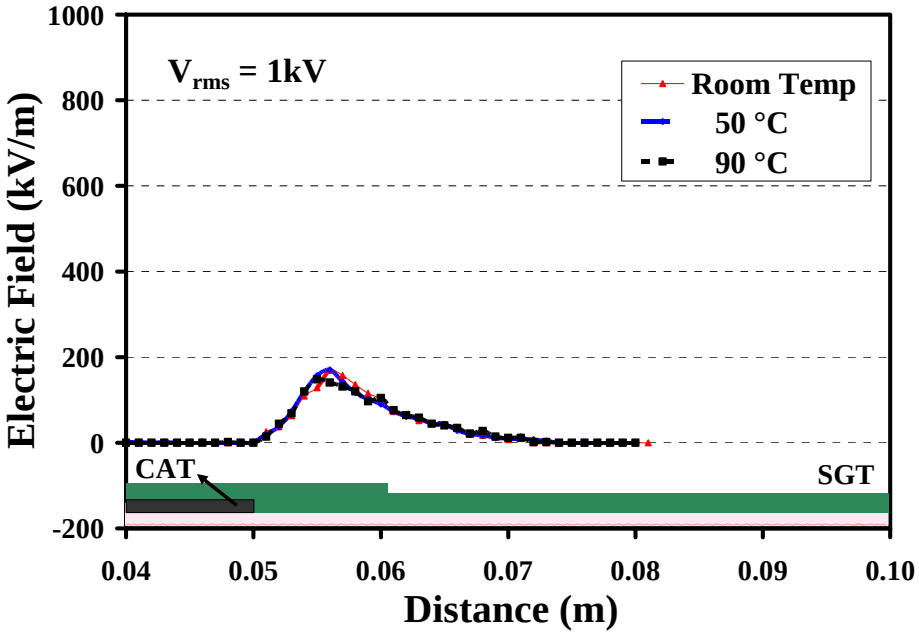

Figure 3-20: Tangential component of the surface electric field extracted from the measurements of the surface potential at 12.5 % nominal voltage and at three temperatures.

3.3.1.2 FEM Modelling and Analysis

Figure 3-21 illustrates the geometry of the SG system used in the FEM modelling, showing the CAT grounded to the body of the machine (G). For the FEM studies, the actual dimensions of a 13.8 kV bar sample were used along with corresponding measured material parameters.

Using the transient finite element modelling (FEM) to simulate the electric field, the surface potential and the electric field distribution is calculated. The geometry used in this modelling is illustrated in Figure 3-21.

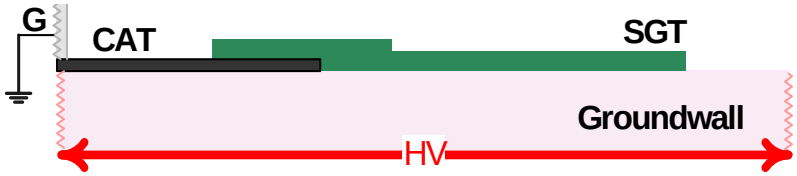

Figure 3-21: Illustration of the stress grading system at the endwinding of the 13.8 kV motor coil used in the simulations.

Electric Field Profile at 60 Hz

The system was simulated at 60 Hz with corresponding material parameters. To consider the effect of the nonlinear field dependent conductivity of the SGT on the surface potential and the

electric field profiles, a transient analysis and a time dependent solver were used according to the methodology explained in Section 2.5.1.

Figure 3-22 shows the simulation results for the tangential component of the electric field on the surface of the coil, which extends from the slot exit to the end of the SGT. To illustrate the effect of the electric stress, the results are shown for coil voltages from 12.5 % to 130 % of the nominal voltage of 8 kV_{rms}, all at 22 °C. The dependency of the electric field on the applied voltage, and therefore on the electric stress, is evident in the figure. The tape geometry shown in Figure 3-21 is superimposed on the lower part of Figure3-22 in order to show the rise in the electric field at the end of the CAT and the discontinuity in the electric field that corresponds to the discontinuity in the SGT.

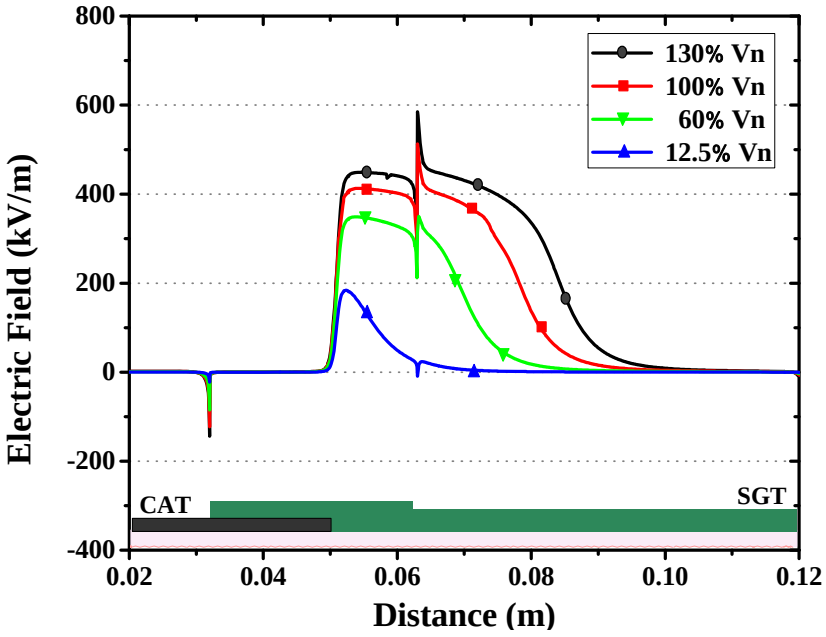

Figure 3-22: Transient FEM simulation of the tangential component of the electric field along the surface of the 13.8 kV coil, at several applied voltages, as a percentage of the nominal voltage of 8 kV_{rms} and at 22 °C.

Figure 3-23 shows the resultant electric field on the surface of the coil. The electric field in the thickness direction (Y) is considerably enhanced at the end of the CAT or the dielectric triple point. However, the present study has determined that the resultant electric field is about 50 % higher than the maximum tangential component of the electric field at the end of the CAT. Figure 3-23 also shows that the maximum tangential electric field (x component at the end of the CAT in Figure 3-23) is about 420 kV/m, a value in agreement with the space charge limited field of 440 kV/m described in Section 3.4.

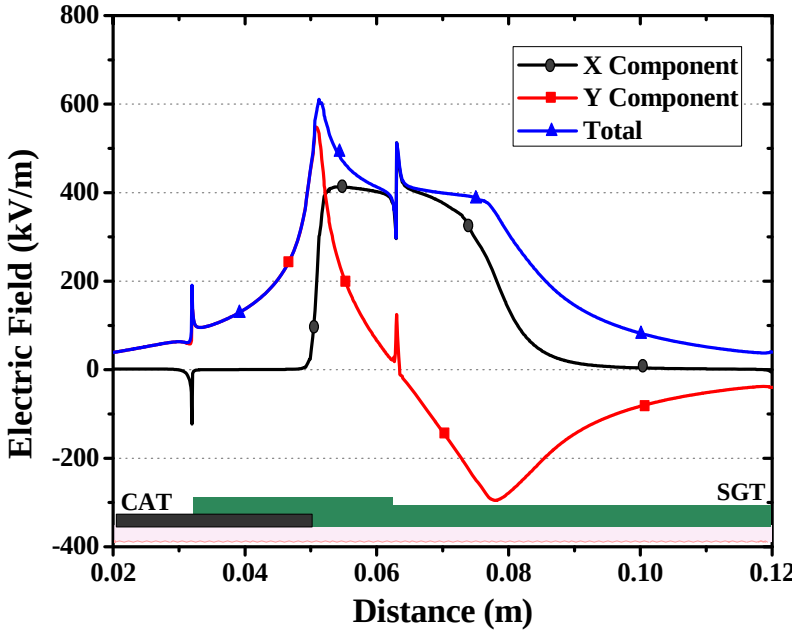

Figure 3-23: Simulated tangential (x), normal (y), and resultant components of the electric field on the surface of the 13.8 kV form-wound coil at 22 °C.

Electric Field Under Repetitive Impulses

Using the transient FEM to simulate the electric field, the surface potential and the electric field distribution for a fast pulse were calculated. The geometry used in this modelling is the same as that illustrated in Figure 3-21.

This simulation requires two steps: the first takes into consideration the dc isotropic properties while the second considers the ac anisotropic properties. Figure 3-24 shows the results of the electric field distribution along the endwinding of the form-wound coil corresponding to the first step, with isotropic properties and with an impulse voltage similar to that indicated in Figure 2-14. It is clear that the electric field is concentrated only in the SG region. It has already been shown that a hotspot can develop on the SGT or in conductive armour regions due to localized field enhancement [51, 106]. Since there is no field enhancement on the conductive armour at the slot exit, the result obtained in this step does not match the experimental results. In the second step, the ac anisotropic properties of the dielectric materials, as described in Section 3.2, are taken into account. Figure 3-25 illustrates the electric field distribution from a transient FEM simulation for the same geometry as in the first step but with different modelling of the sub-domains. In addition, a very small gap between the CAT and the ground plate similar to that in the actual conditions is included in the geometry. This air gap indicates the imperfect contact between the surface of the bar and the ground plate, particularly at the corners.

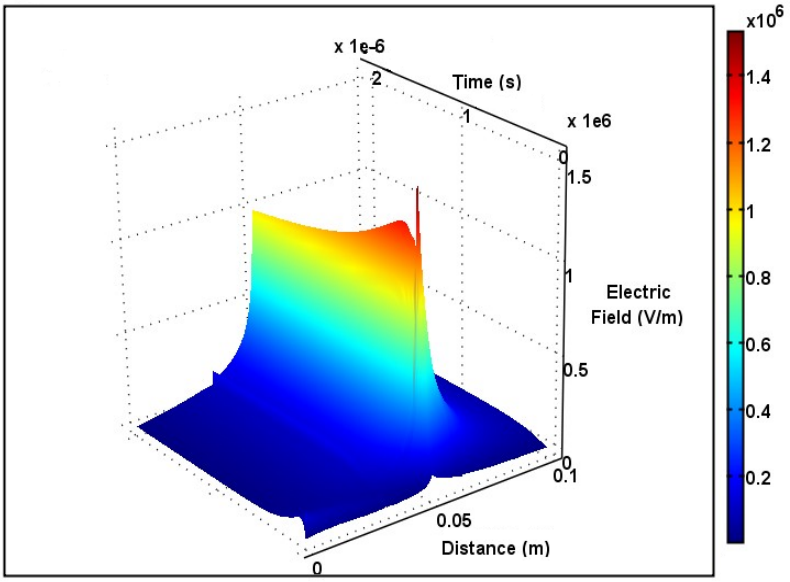

Figure 3-24: Electric field distribution along the endwinding of the 13.8 kV form-wound coil, energized with an impulse voltage using a transient FEM simulation with dc isotropic parameters of the materials.

In Figure 3-25, two regions of the high electric field stand out and correspond to the locations where the hot spots will develop: one is in the SG region and the other is on the CAT at the slot exit.

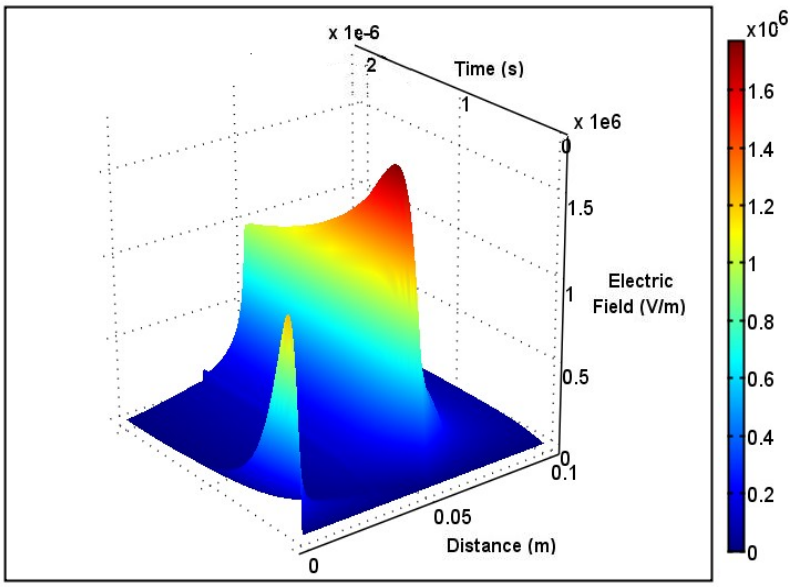

Figure 3-25: Electric field distribution along the endwinding of the 13.8 kV form-wound coil, energized with an impulse voltage using transient FEM simulation with ac anisotropic parameters of the materials.

3.3.2 Capacitive SG System

The impact of a high repetition rate and the high frequency components of the PWM pulses on resistive SG systems can be attributed to PD activity and joule heating. Therefore, a capacitive SG scheme that is independent of frequency may be an effective solution. Figure 3-26 illustrates two geometries for applying floating conductive foils within the groundwall insulation of 13.8 kV motor coils. In the first design, Figure 3-26 (a), three layers of aluminum foil are centred over the end of the CAT. The number, position, and length of these foil layers are the parameters that were selected based on the stress relief required as shown in Figure 3-27. In the second design, Figure 3-26 (b), three layers of aluminum foil are placed to extend from the slot exit beyond the CAT so that the length of layers increase step-by-step from the top to the lowest layer.

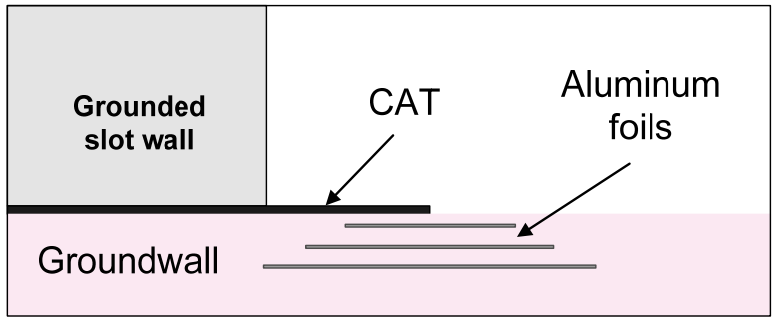

(a)

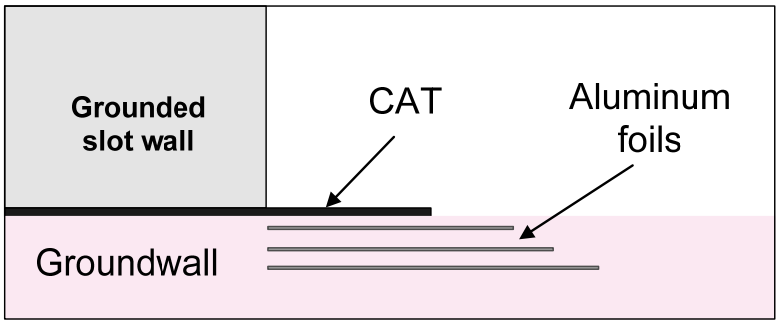

(b)

Figure 3-26: Geometries of two capacitive SG schemes under study according to three layers of aluminum foil (a) centered over the end of CAT (b) aligned with the slot exit.

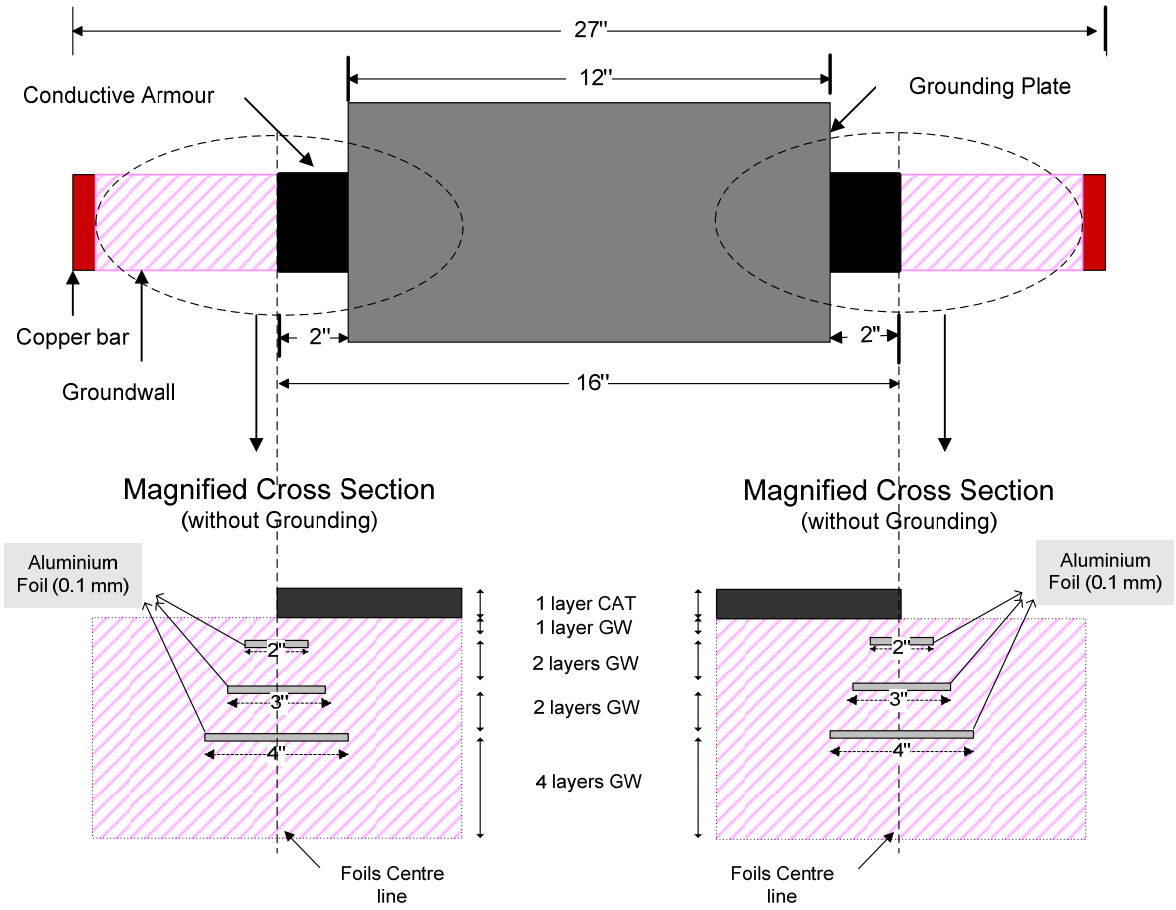

Figure 3-27: Cross section of a sample with a capacitive SG based on floating layers of aluminum foil.

Figure 3-28 shows the surface potential measured along the end portion of two samples using the capacitive SG systems when energized at 8 kV_{rms} and at 60 Hz. The electric fields calculated according to the method described in Section 2.4.4 are plotted against the corresponding surface potentials. As can be seen, the maximum electric field for both designs is nearly the same and is lower than the breakdown voltage of air. It can be then concluded that both designs can adequately control the electrical stress at 60 Hz.

The capacitive SG system shown in Figure 3-26 (a) was studied using FEM modelling. A time-harmonic analysis, or steady state analysis, was run at 60 Hz in order to determine the surface potential and the electric field. Since the conductivity of the aluminum foil is much higher than that of the groundwall insulation, several subsequent simulations were performed for gradually increasing levels of the foil conductivity in order to produce reasonable results. Figure 3-29 (a) shows the equipotential lines when a time-harmonic simulation was run in one step with the actual electrical conductivity of aluminum foil. As can be seen, the equipotential lines are concentrated at the end of the lowest aluminum layer, which is unrealistic. This phenomenon

occurred because of a numerical computation error resulting from a very large transient between the conductivity of the foils (order of 6) and the groundwall insulation (order of -15). When the conductivity of the foil was increased by three steps, from orders of -6, 0, and 6, and the first results were assigned as the initial conditions for the next simulation, equipotential lines can distributed appropriately similar to those shown in Figure 3-29 (b). It should be noted that this problem can be avoided if a transient analysis with a time dependent solver is used.

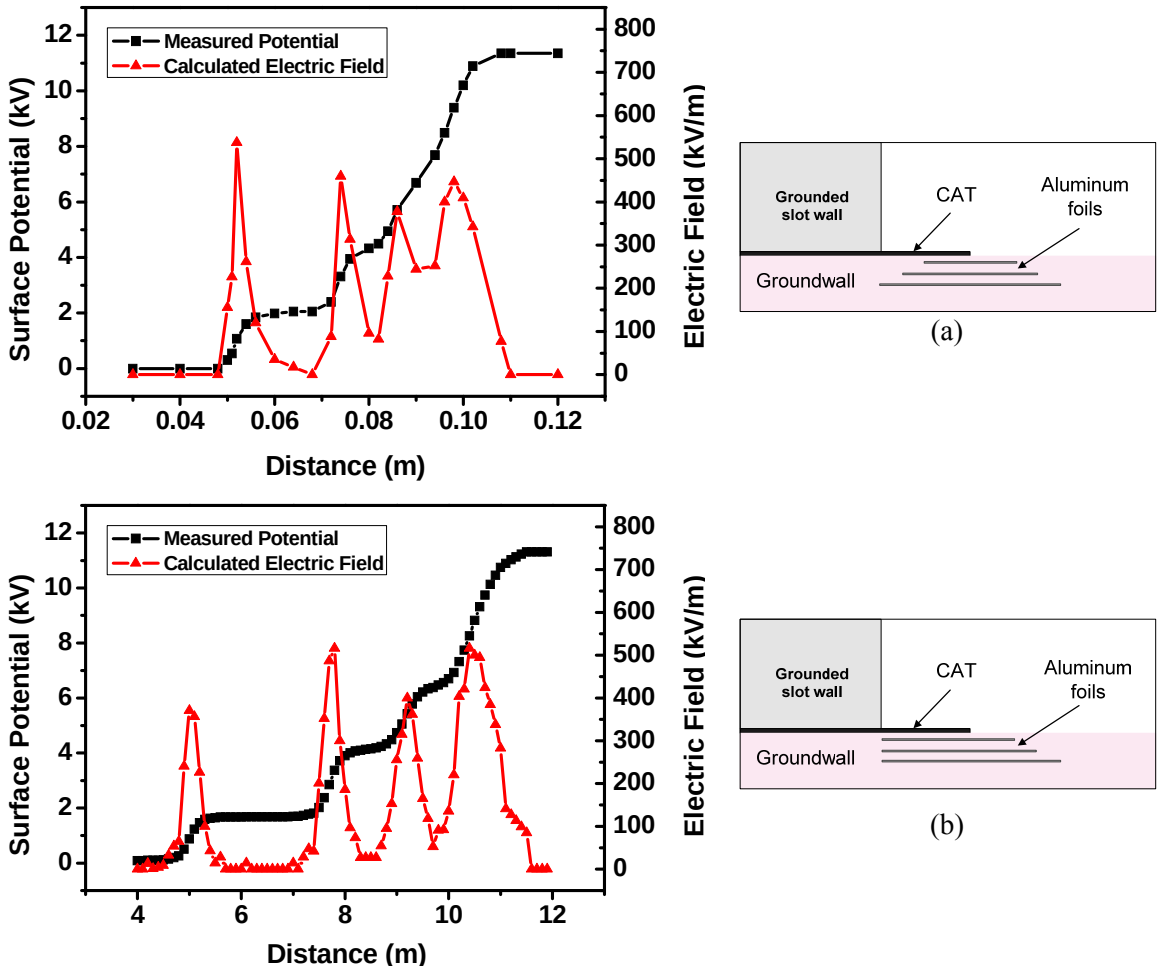

Figure 3-28: Measured surface potential and calculated electric field for two designs of the capacitive SG system with aluminum foil embedded within the groundwall insulation.

Figure 3-30 (a) shows the measured and simulated surface potentials in the endwinding region at 60 Hz. The voltage rises smoothly from ground to maximum phase voltage (11.2 kV), and the FEM-simulated result corresponds closely to measured potential. Figure 3-30 (b) also depicts the total electric field and the longitudinal electric field obtained from the simulation, along with the electric field calculated from the measured surface potential. The simulated electric field in the longitudinal direction (x component) is nearly identical to the calculated electric field. As

expected, the pattern of the total electric field is different from that of the calculated one. The main reason for this discrepancy is the effect of the second component of the electric field, which is perpendicular to the surface.

The effect of replacing the aluminum foils with CAT as a conductive tape for the capacitive SG schemes was also investigated. At 60 Hz and for the samples with conductive tape (CAT) embedded within the groundwall insulation, the surface potential and corresponding electric field along the SG region are quite similar to those with aluminum foil. These results confirmed that at 60 Hz CAT offers good conductive properties similar to those of aluminum foil.

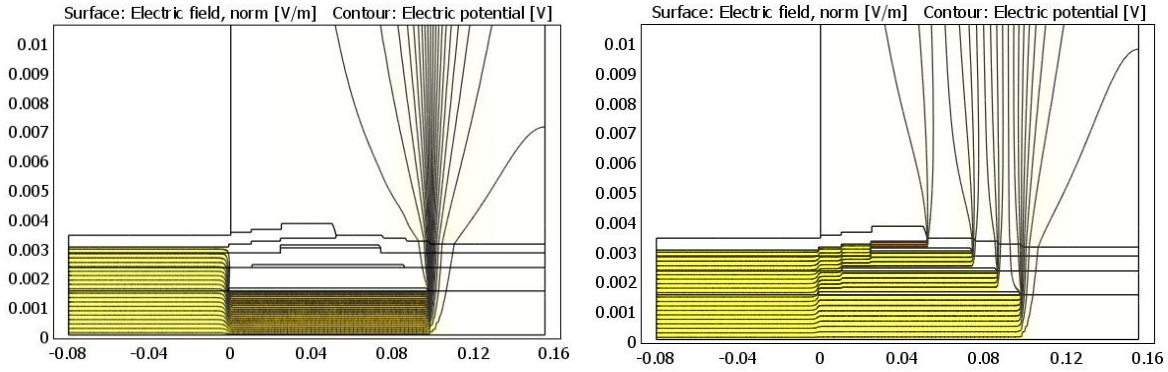

(a) (b)

Figure 3-29: Equipotential lines in a capacitive SG system with aluminum foils embedded within the groundwall insulation resulting from a time harmonic analysis run in (a) one step and (b) three step simulations.

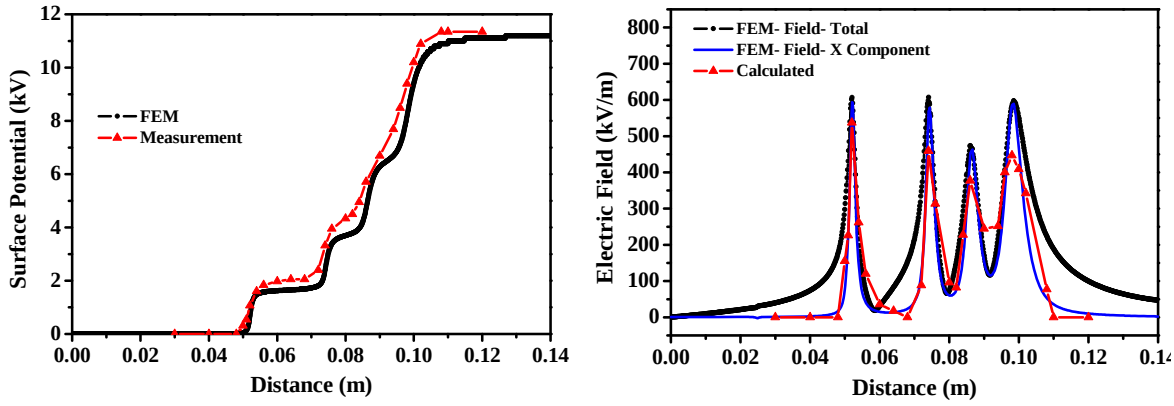

(a) (b)

Figure 3-30: Measured and simulated (a) surface potential along the end portion of the first proposed capacitive SG system energized with 60 Hz, 8 kV_{rms}, (b) electric field distribution.

Using the transient FE simulation, the electric field profile along the end portion of the sample with developed capacitive grading (Figure 3-26 (a)) energized with an impulse voltage is calculated. As shown in Figure 3-31, the electric field in SG region is appropriately control in an acceptable level that is much lower than the field in the conventional SG system at the same conditions as presented in Figure 3-25.

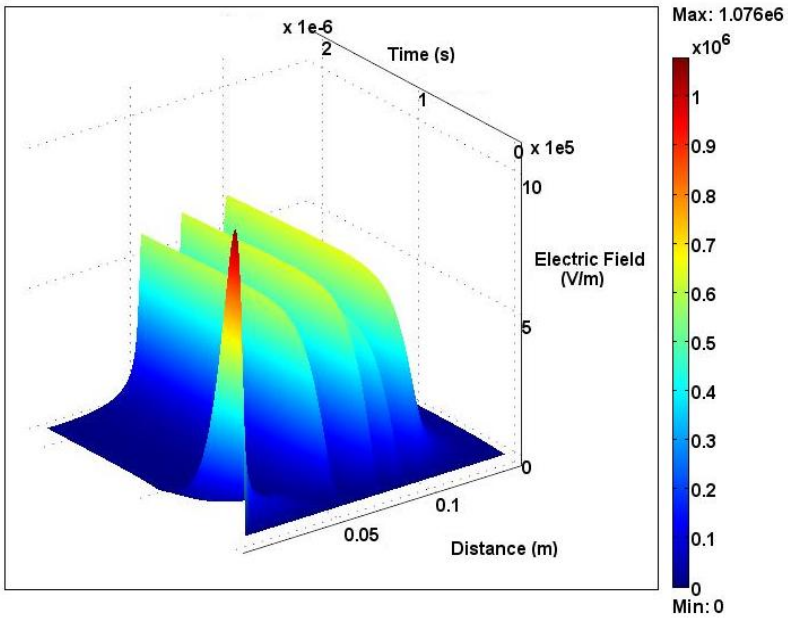

Figure 3-31: Electric field distribution along the endwinding of the bar sample with developed capacitive SG system energized with an impulse voltage using transient FEM simulation.

3.4 Thermal Stress Analysis

To investigate the effect of steep front pulses on motor coils, a series of tests were performed on both conventional and the proposed capacitive SG systems on 13.8 kV bar samples. Because the electrical and thermal stresses that developed on the conventional SGT are frequency dependent, the effects of the voltage waveform were investigated separately in detail.

3.4.1 Temperature Profile along the Conventional SG System

Tests were performed using bar samples constructed using identically the same insulation system as that of a 13.8 kV motor coil, as described in Section 2.2. Every data point reported is an average of 8 readings obtained from conducting tests on two bars. The thermal stresses due to three different voltage waveforms are compared in the following subsections.

3.4.1.1 PWM Voltage

Figure 3-32 shows the unipolar two-level PWM pulse train from the PWM generator used in the study. Due to the consistent pulse height of the generator, this type of PWM pulse stresses the insulation system of a 13.8 kV motor bar to a greater extent than a multi-level (> 2) PWM waveform. Previously it was shown that the temperature rise in the end portion of a 13.8 kV motor bar sample, with the voltage waveform illustrated in Figure 3-32, is nearly identical to that obtained with a unipolar square wave voltage (Figure 3-33) with a 50 % duty cycle [143]. This demonstrates the equivalence when the voltage peaks, switching frequencies (repetition rates), and rise and fall times of the pulses are identical.

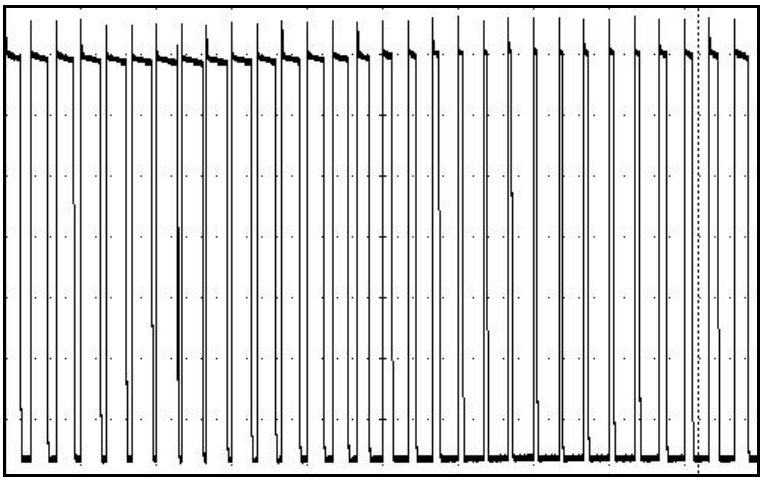

Figure 3-32: Unipolar two-level PWM pulses from the PWM generator used in the study.

3.4.1.2 Square Voltage

Figure 3-33 shows the train of a typical square wave pulse voltage used in this study. The pulse rise time (t_r), overshoot, and fall time (t_f) are functions of the switching devices, the feeder cable, and the load impedance characteristics.

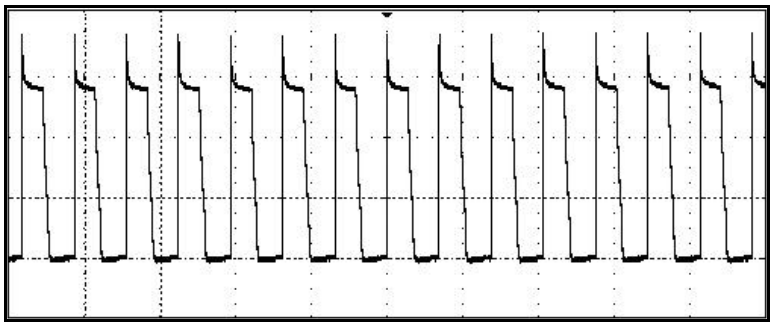

Figure 3-33: A typical train of square pulses with a 50 % duty cycle used in the study.

It is important to note that the rise time, measured by an oscilloscope, is based on the time between 10 % and 90 % of the peak value, which is different from the definition used in IEC TS 60034-18-42 [4] as indicated in Figures 2-13 and 2-14. All rise times used in this study are therefore based on the IEC definition, which is calculated from the value measured with an oscilloscope as $t_r = (t_{90} - t_{10})_r * 1.25$.

The temperature profile along the end portion of a 13.8 kV motor bar that has been energized with a square pulse train is shown in Figure 3-34. Hot spots are evident in both the stress grading (SG) region and at the slot exit.

Figure 3-35 shows the maximum temperature rise (ΔT) as function of the rise time of the square wave voltage at different repetition rates (switching frequencies). The duty cycle of the pulses is 50 % and is fixed. A low value series resistance was inserted into the circuit in order to change the rise time of the square wave pulses. Although the voltage rating of the sample is 11.2 kV_{peak} (peak of phase-to-ground), for this study, 10 kV_{p-p} was chosen due to the limitations of the power supply. The square wave pulses have an almost fixed fall time (t_f) that is much larger than the rise time ($t_f = 31$ µs).

As evident in Figure 3-35, the rise time of the pulses has little influence on the temperature rise on the SGT, particularly for lower switching frequencies. However, the effects are significant with respect to the hot spot on the CAT at the slot exit. Electric field enhancement and surface discharge are the main causes of hot spots in this area, as both are very sensitive to the pulse rise time and the repetition rate [144].

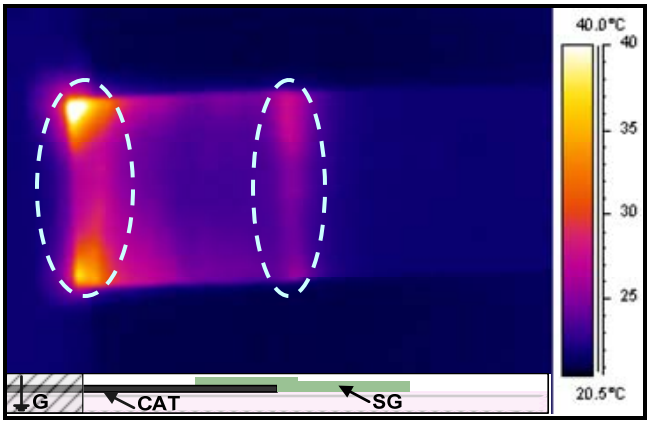

Figure 3-34: Temperature profile along the surface of a 13.8 kV motor bar sample energized with a square wave voltage: t_r = 181 ns, t_f = 31 µs. The illustration at the bottom of the figure corresponds to the geometry of the bar sample.

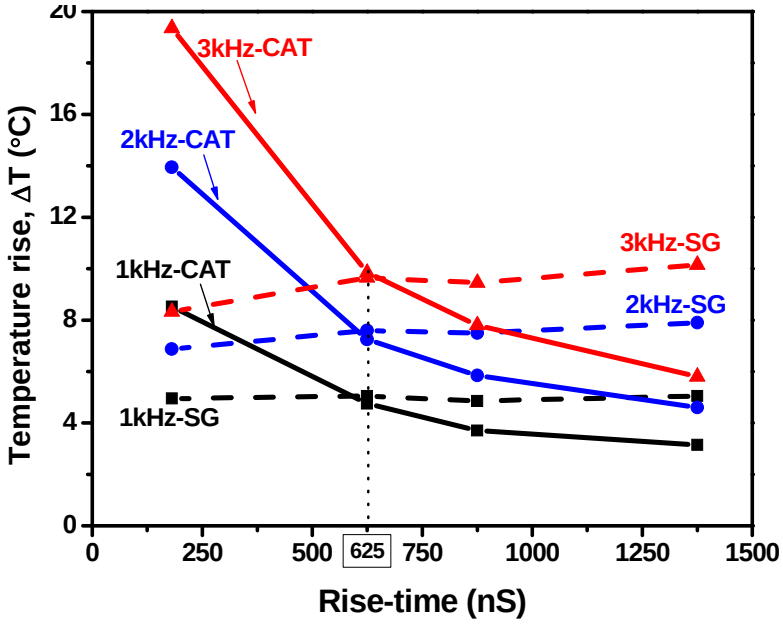

Figure 3-35: Maximum temperature rise of the CAT at the slot exit and of the SGT in the SG region as a function of the rise time at different switching frequencies for a 10 kV_{p-p} repetitive square wave voltage.

3.4.1.3 Impulse Voltage

Figures 3-36 and 3-37, respectively, show the typical form of an impulse voltage train and the temperature profile along the end portion of a 13.8 kV motor bar sample that is energized from the impulse train. In this case, hot spots are evident on both the SGT and on the CAT at the slot exit, but the heat distribution is different from that indicated by the profile shown in Figure 3-34.

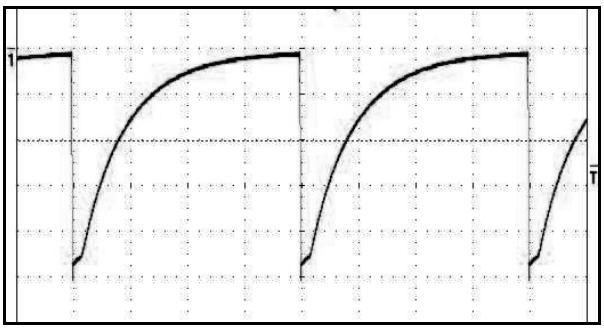

Figure 3-36: A typical repetitive impulse voltage used in the study.

The temperature rise, plotted as a function of switching frequency of the impulse voltage train with a pulse peak of 10 kV_{p-p} and a fixed rise time of 625 ns, is shown in Figure 3-38. It has been demonstrated that due to this impulse train (t_r = 625 ns, t_f = 100 μs), the temperature rise on the CAT at the slot exit is almost identical to that produced by the square wave voltage with the same

rise time and switching frequencies (Figure 3-34). However, in this case, the temperature of the hot spot in the SG region that is due to the square wave voltage is almost 50 % higher than that produced by the repetitive impulse voltage and is almost equal to that produced by the impulses that have twice the switching frequency.

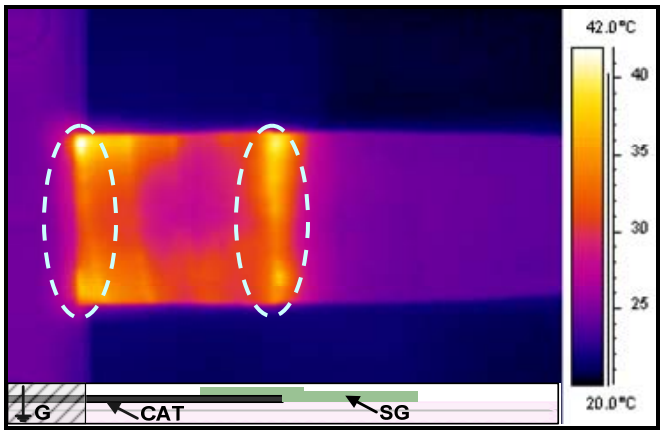

Figure 3-37: Temperature profile along the surface of a 13.8 kV motor bar sample energized with a repetitive impulse voltage: t_r = 625 ns, t_f = 100 μs. The illustration at the bottom of the figure corresponds to the geometry of the bar sample.

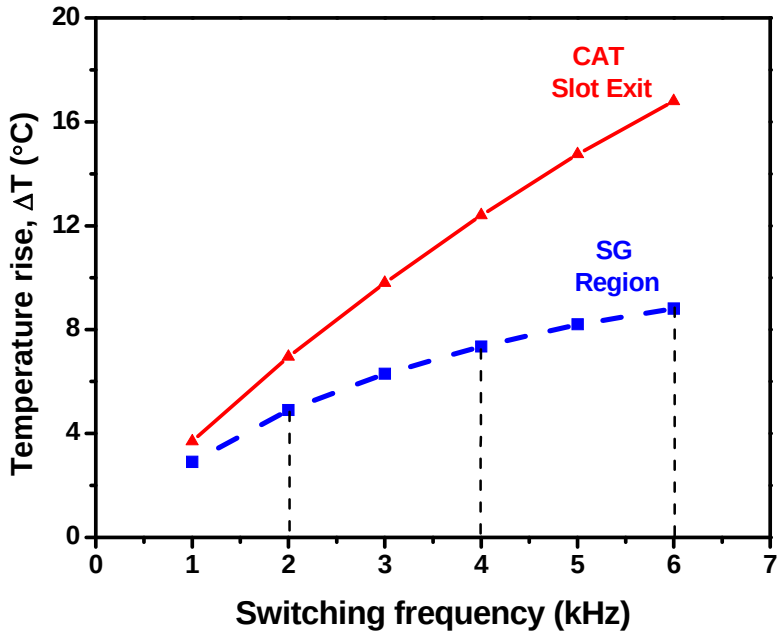

Figure 3-38: Temperature rise at the slot exit and in the SG region plotted as a function of switching frequency (repetition rate) of a 10 kV_{p-p} repetitive impulse voltage with a 625 ns rise time.

3.4.1.4 High Frequency Tests

In Section 2.5.2, it was analytically shown that for a conventional SG system two sinusoidal voltages at different frequencies can represent a train of impulse voltage with the same heat generation. To verify the proposed method, high-frequency (HF) tests were carried out for two different frequency ranges. The first range corresponds to the switching frequency of PWM voltage source inverters (1 kHz to 5 kHz) of drive duty motors. The second range (30 kHz to 60 kHz) was adopted in order to include higher order harmonics. It is evident from Figures 3-39 to 3-42 that for the first range of frequencies, the hot spot is located in the SG region, but for the second range of frequencies, the hot spot develops at the slot exit.

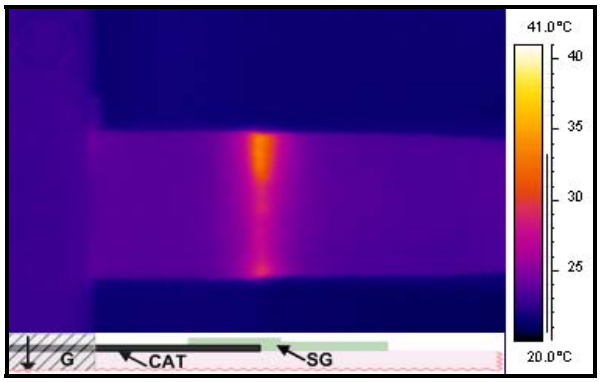

Figure 3-39: Temperature profile along the surface of a 13.8 kV motor bar sample energized with 5 kHz sinusoidal voltage at 3 kV_{rms} .

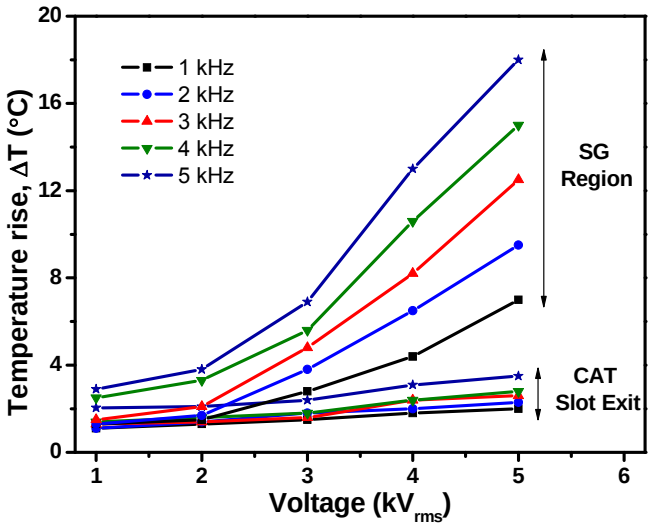

Figure 3-40: Maximum temperature at the slot exit and in the SG region of a 13.8 kV motor bar sample energized with 1-5 kHz.

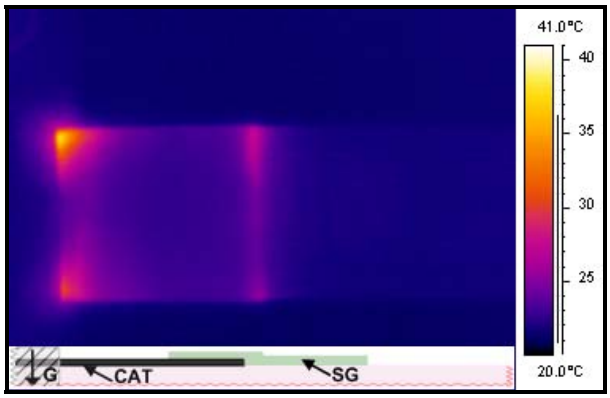

Figure 3-41: Temperature profile on the surface of a 13.8 kV motor bar sample energized with a 50 kHz sinusoidal voltage at 1.7 kV_{rms}.

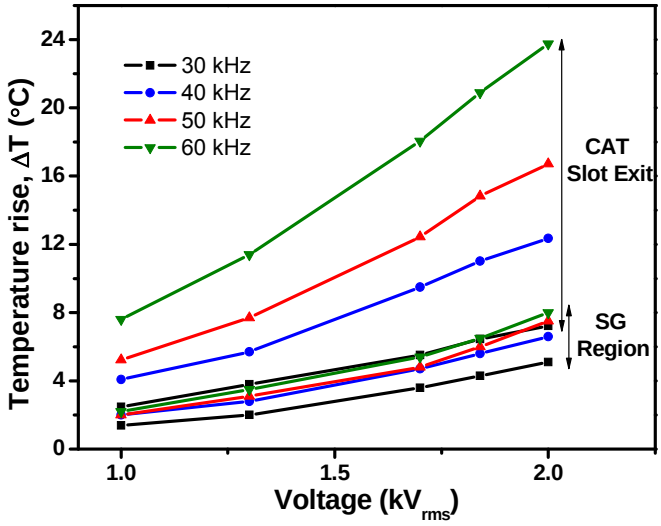

Figure 3-42: Maximum temperature at the slot exit and the SG region of a 13.8 kV motor bar sample energized with 30-60 kHz.

The decomposed power of the signal and a comparison of the temperature rise from the actual pulse trains shown in Figure 3-35 or 3-38, with the HF test results can be used to find k_1 and k_2 in equation (2-38). The results for the impulse train are presented in Table 3-1, the parameters of which are related to an impulse voltage with t_r = 625 ns and t_f =100 µs. These values of k_1 and k_2 are valid for similar impulse voltages with peak values up to 13 kV. Similarly, the coefficients k_1 and k_2 can be found for square pulse voltages with the rise times indicated in Figure 3-34. As shown, the temperature rise in the SG region is nearly proportional to the rise time. In other words, a larger rise time (slower pulses) causes a slightly higher temperature in the SG region,

particularly for higher switching frequencies. The reverse is true for the CAT; i.e., a smaller rise time (faster pulses) causes more intense hot spots on the CAT at the slot exit.

Table 3-1: Parameters for the HF analysis associated with an impulse voltage of 10 kV_{p-p} and with different switching frequencies: t_r = 625 ns and t_f=100 μs.

Switching Frequency (kHz)	$\sqrt{P_{v1}}$	$\sqrt{P_{v2}}$	A_1 (kV_{rms})	A_2 (kV_{rms})	k_1	k_2
1	1.3e3	634	2.8	0.7	2.08	1.13
2	1.9e3	879	3	1	1.57	1.15
3	2.3e3	1.1e3	3	1.3	1.27	1.24
4	2.7e3	1.2e3	3	1.5	1.11	1.26
5	3e3	1.4e3	3	1.7	1	1.22

The variations in the coefficients k_1 and k_2 with the rise time at different switching frequencies are in the range of (0.275-0.394) and (0.21-0.67), respectively. If the worst case is taken into account, the highest values of k_1 and k_2 must be selected. With these coefficients, maximum thermal stresses are generated in both the SGT and the CAT. According to this technique, HF high voltages can be applied individually in order to evaluate the thermal performance of the SGT and the CAT under repetitive fast pulses. They can also be superimposed as a means of studying the thermal effect on the whole system.

3.4.2 Coupled Electro-Thermal Field Simulation

3.4.2.1 2D- FEM Modelling

As previously indicated, the temperature rise associated with a single voltage impulse is very small [142, 144]; therefore, repetitive pulses must be applied to detect any rise in temperature. Running a transient coupled electro-thermal FEM simulation for repetitive fast pulses, such as 5 kHz, is impractical because the computation becomes complex and laborious. For modelling and computer simulation, a stationary analysis based on two sinusoidal voltages of different frequencies is therefore proposed as an alternative to a transient analysis for multiple pulses. As discussed in Section 2.5.2, the frequency and amplitude of such sinusoids are related to the switching frequency, the signal power, and the nonlinearity of the system and can be found from equation (2-38). Based on the frequencies and amplitudes determined in Section 3.4.1.4, Figures 3-43 and 3-44 show the temperature profile on the end portion of a 13.8 kV motor bar sample

caused by the two sinusoidal voltages obtained through static coupled electro-thermal finite element analysis. In Figure 3-43, with a 5 kHz and 3kV sinusoidal voltage, the main hot spot is located in the SG region; and correspondingly, with a 50 kHz and 1.7 kV sinusoidal voltage, the hot spot is on the CAT at the slot exit, as shown in Figure 3-44.

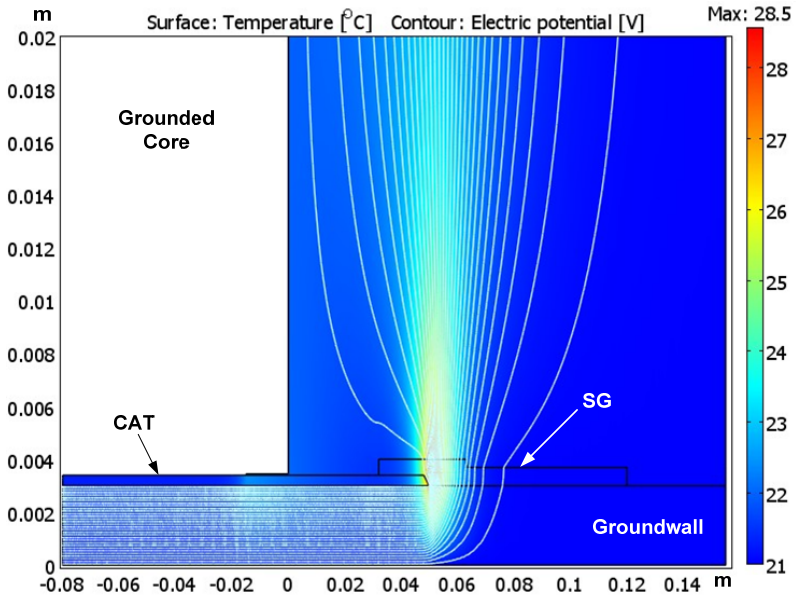

Figure 3-43: Temperature profile and equipotential lines on the end of a 13.8 kV motor bar sample, energized with a 5 kHz, 3 kV sinusoidal voltage.

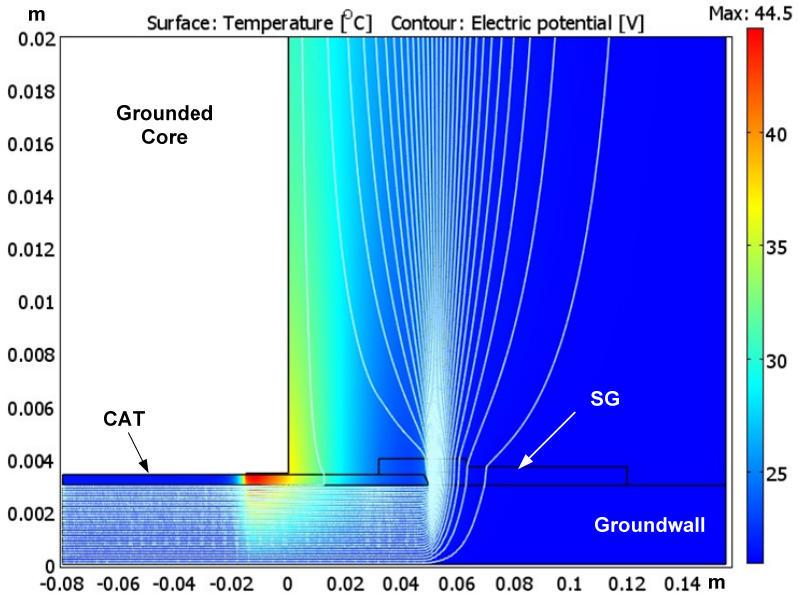

Figure 3-44: Temperature profile and equipotential lines on the end of a 13.8 kV motor bar sample, energized with a 50 kHz, 1.7 kV sinusoidal voltage.

A comparison of the total surface temperature shown in Figure 3-45 with the temperature profile from the actual repetitive impulses indicated in Figure 3-37 reveals good agreement between the results. This agreement confirms that the suggested method is an effective alternative method of investigating the thermal effect of repetitive impulses on the stress grading system of form-wound motor coils.

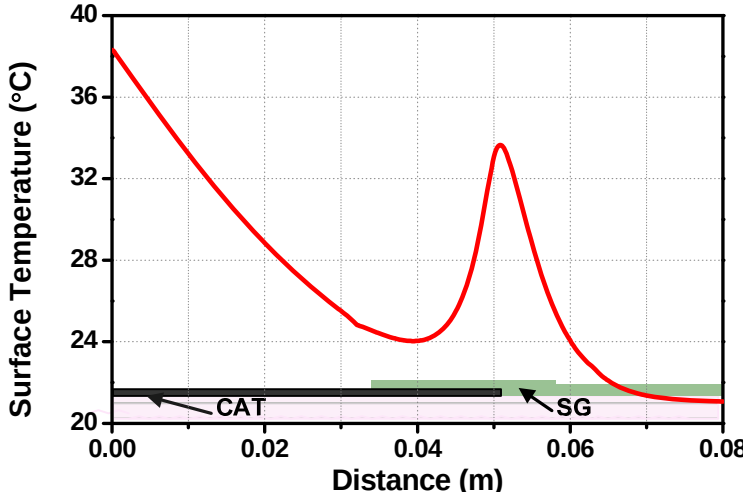

Figure 3-45: Superposition of temperature rises along the end portion of a 13.8 kV motor bar sample arising from 5 and 50 kHz sinusoidal voltages.

3.4.2.2 3D- FEM Modelling

The previous section presented the use of 2D FEM modelling for studying the electric field distribution and temperature profile along the endwinding of a 13.8 kV motor coil subjected to repetitive fast pulses for comparing the results with experimental work. Since the model has been developed in two dimensions, the locations and the reasons for developing the electrical and thermal stresses on the endwinding of the motor coils cannot be studied in detail. For example, due to the shape of the current-carrying conductors and the method of taping, the electrical and thermal stresses are concentrated near the coil corners. In addition, because of the inconsistent thickness of ground-wall and conductive armour layers, the outer surface of the coil is conical and has imperfect contact with the body of the stator slot at the corners. As a result, air gaps are formed between the coil and the grounded body, particularly at the slot exit. These air gaps, normally filled by resin during the global VPI process, are susceptible to electric field enhancement (edge breakdown effect [23]), surface discharge, and local temperature rises under high frequency transients. The high energy discharges can be a threat to the integrity of the insulation and may also be unacceptable for some motors that are operated in hazardous areas [96].

The 3D geometry of the test specimen used in this study is shown in Figure 3-46. To decrease the computational time and memory requirement, only the portion near the slot exit is included in the model. This portion consists of the CAT, SGT, groundwall (GW) insulation, and a small section of the grounded body (slot).

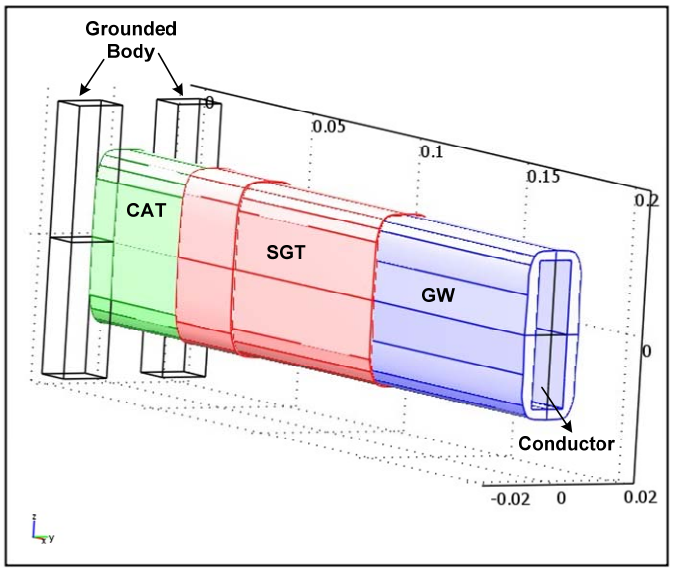

Figure 3-46: 3D geometry of the model used in the FEM simulation of the motor bar.

As previously shown, the thermal stress on the SGT and CAT of a 13.8 kV form wound motor bar subjected to a 5 kHz impulse voltage train with a height of 10 kV and a rise time of 625 ns is analogous to two sinusoids: the first at 5 kHz and 3 kV, and the second at 50 kHz and 1.7 kV. The thermal and dielectric parameters of the materials, described in Section 3.2., were used in the simulation. The frequency dependency and anisotropic dielectric properties of the materials were also taken into account in the simulation.

Figure 3-47 shows the temperature profile for the model shown in Figure 3-46 when energized at 3 kV at 5 kHz. The hot spot is shown to concentrate at the end of the CAT and in the SG region. In the second case, shown in Figure 3-48, and energized at 1.7 kV and 50 kHz, causes the hot spots to develop at the slot exit.

Both these simulation results are in good agreement with the laboratory experiments, which are presented in Section 3.4.1.4. The images in Figures 3-39 and 3-41 were obtained using infrared thermography. The surface temperature patterns taken from the 3D FEM simulation are very close to the actual ones. The discrepancies between the maximum surface temperatures are about 5 %. All the results verify the efficacy of the 3D FEM modelling and the material characterization.

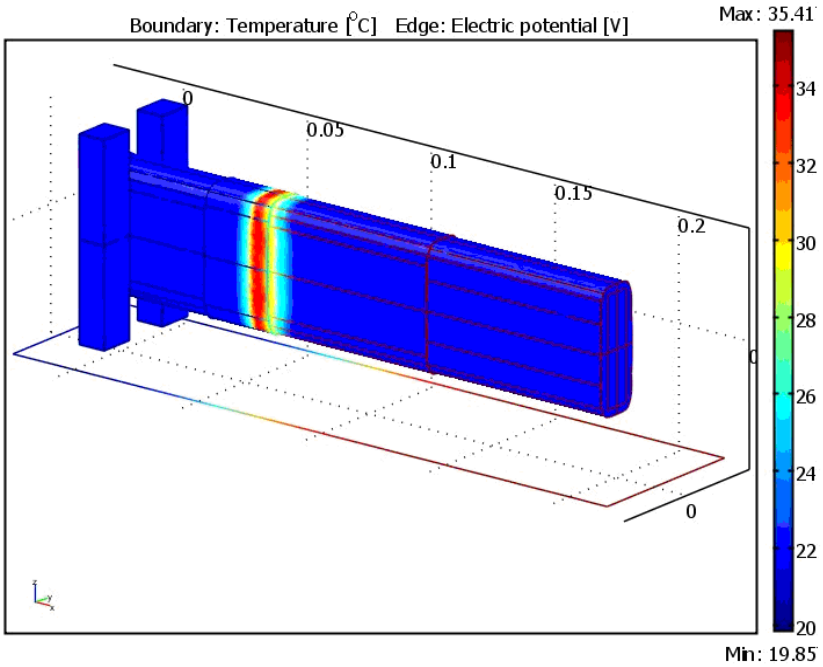

Figure 3-47: Temperature profile on the surface of a 13.8 kV motor bar sample energized at 3 kV_{rms}, 5 kHz sinusoidal voltage.

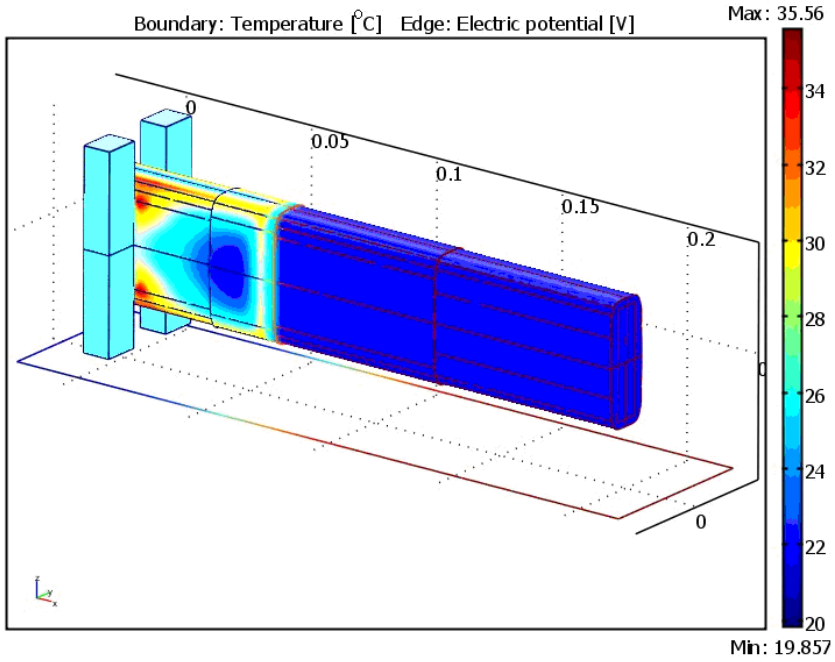

Figure 3-48: Temperature profile on the surface of a 13.8 kV motor bar sample energized at 1.7 kV_{rms}, 50 kHz sinusoidal voltage.

3.4.3 Capacitive SG System

The temperature profiles along the capacitive SG schemes introduced in Section 3.3.2 were studied and compared with the conventional SG system. However, the results presented in this section correspond to those produced by the capacitive SG scheme shown in Figure 3-26 (b), which provides better thermal performance than the one illustrated in Figure 3-26 (a).

The samples were subjected to a 13 kV peak-to-peak impulse voltage at various repetition rates. Figure 3-49 shows the temperature profile along the end portion of two samples with different SG systems: the conventional SG and the capacitive SG with embedded aluminum foils. In the resistive system, hot spots develop while in the capacitive system, no hot spots are present. In addition, the temperature is distributed uniformly in the capacitive SG system, and for each repetition rate, the maximum temperature is much lower than in the conventional SG. It is therefore concluded that the proposed capacitive SG system, based on conductive foil embedded in the groundwall, mitigates localized thermal stress on the end portion of motor coils fed by PWM-VSC.

The performance of the capacitive SG scheme with CAT embedded in the groundwall was studied separately. In Section 3-3-2, it was shown that the CAT is a conductive tape at 60 Hz and can replace aluminum foil. Figure 3-50 shows the thermal profiles along the end portions of two samples with a similar capacitive SG scheme energized with repetitive fast pulses. Hot spots are evident on the sample with embedded CAT, and the temperature rise is much higher than for the samples with embedded aluminum foil. In addition, hot spots now appear at the corner edges of the sample, particularly in the regions where CAT overlaps.

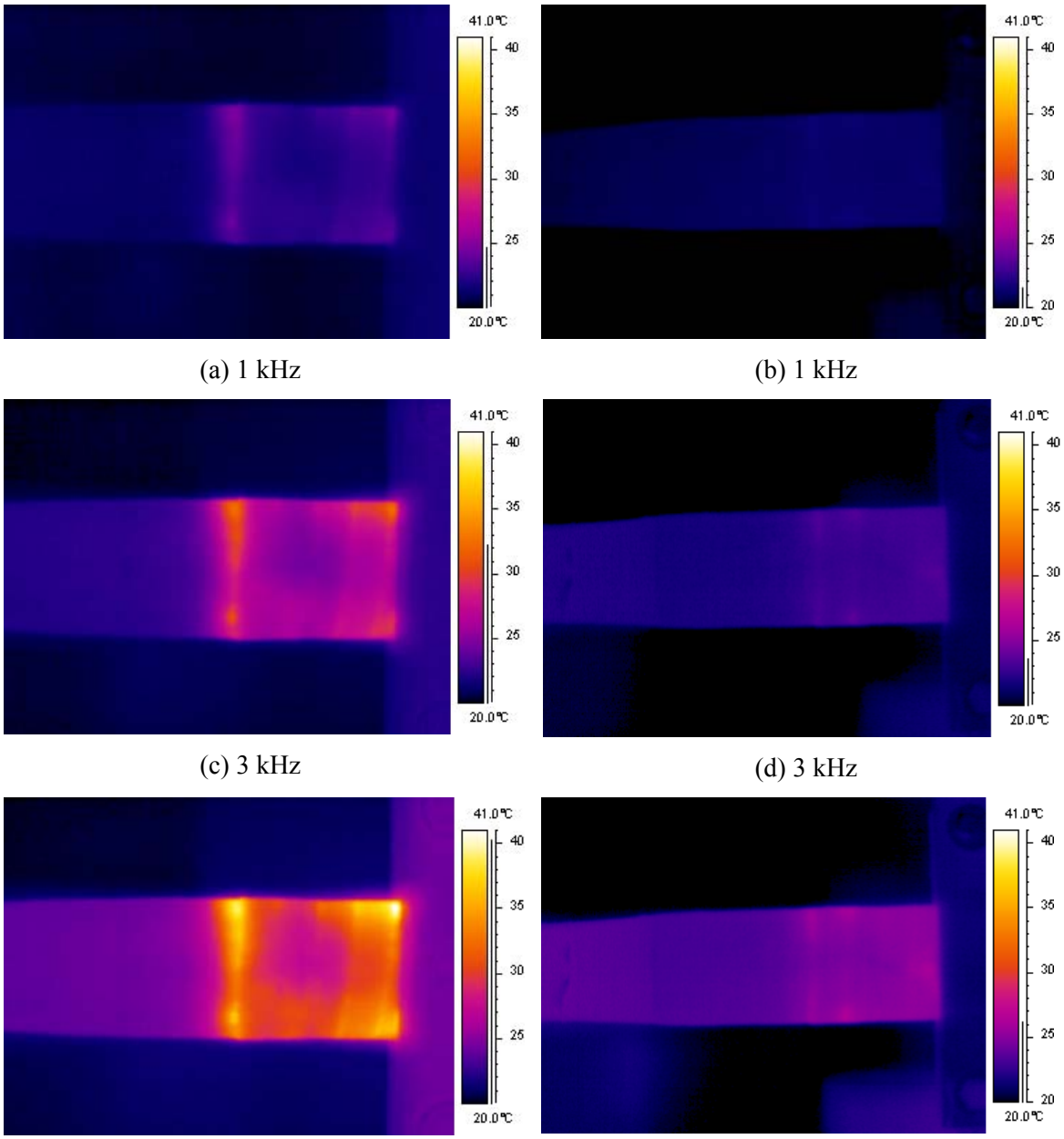

(a) 1 kHz (b) 1 kHz

(c) 3 kHz (d) 3 kHz

(e) 5 kHz (f) 5 kHz

Figure 3-49: Surface temperature profiles along the end portions of two samples energized with impulse voltages at different repetition rates: (a, c, e) with the conventional resistive SG system and (b, d, f) with the capacitive SG system.

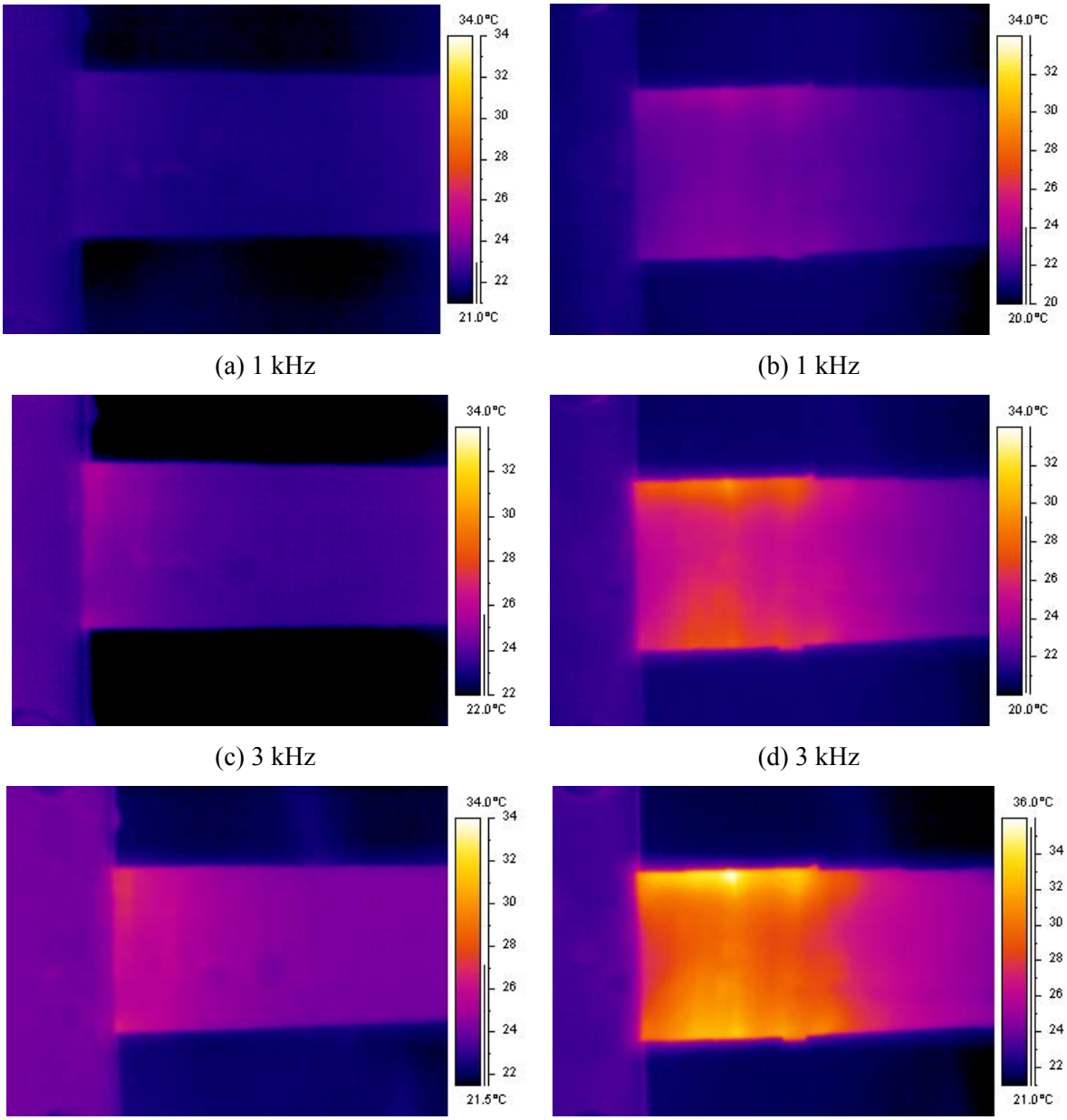

(a) 1 kHz (b) 1 kHz

(c) 3 kHz (d) 3 kHz

(e) 5 kHz (f) 5 kHz

Figure 3-50: Surface temperature profiles along the end portions of two samples with capacitive SG energized with impulse voltages at different repetition rates: (a, c, e) with aluminum foils and (b, d, f) with the CAT embedded in the groundwall insulation.

3.5 Qualification Testing

Using the setup and procedure explained in Section 2.4.6, tests were performed in order to demonstrate qualification of the proposed capacitive SG system for form-wound motor coils when energized with a repetitive fast pulse voltage. Based on the results obtained from the

performance tests on the samples with the preliminary capacitive SG designs presented in Sections 3.3.2 and 3.4.3, the samples with the design described in next paragraphs were manufactured by GE Canada and were used for the qualification tests.

Figure 3-51 shows the schematic geometry of the final samples that incorporate the proposed capacitive SG system. Rather than the previous configuration shown in Figure 3-26 (b), in the final design and for easier manufacturing, three equal-length aluminum foil layers were applied. The two outer layers of aluminum foils are also extended to the inside of the slot in order to decrease the stress at the slot exit as much as possible. However, since at least one layer of mica tape must be applied after the top layer of aluminum foil, this configuration does produce a minimal amount of electrical stress at the slot exit during the rising of the fast pulses. The layer closest to the copper bar begins at the slot exit so that with respect to the slot clearance limit, the total insulation thickness is not exceeded. The cross-section of the sample illustrated in Figure 3-52 shows the detailed configuration of the final proposed capacitive SG system.

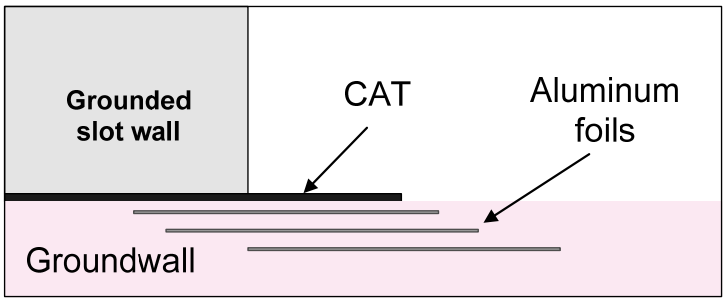

Figure 3-51: Schematic geometry of the final samples with the proposed capacitive SG with aluminum foil embedded in the groundwall insulation.

Five samples with conventional nonlinear resistive SGT (R1 to R5) and five samples with the proposed capacitive SG system (C1 to C5) were tested. The test was performed at a fixed forced heat level of 155 °C using the setup depicted in Figure 2-10. Rather than the temperature being controlled at 155 °C during the test, the heaters were controlled so that the insulation temperature was 155 °C at the middle of the samples at no voltage. The power of the heaters was maintained after energizing the samples. With this temperature setting, the temperature rise due to the dielectric loss can be investigated.

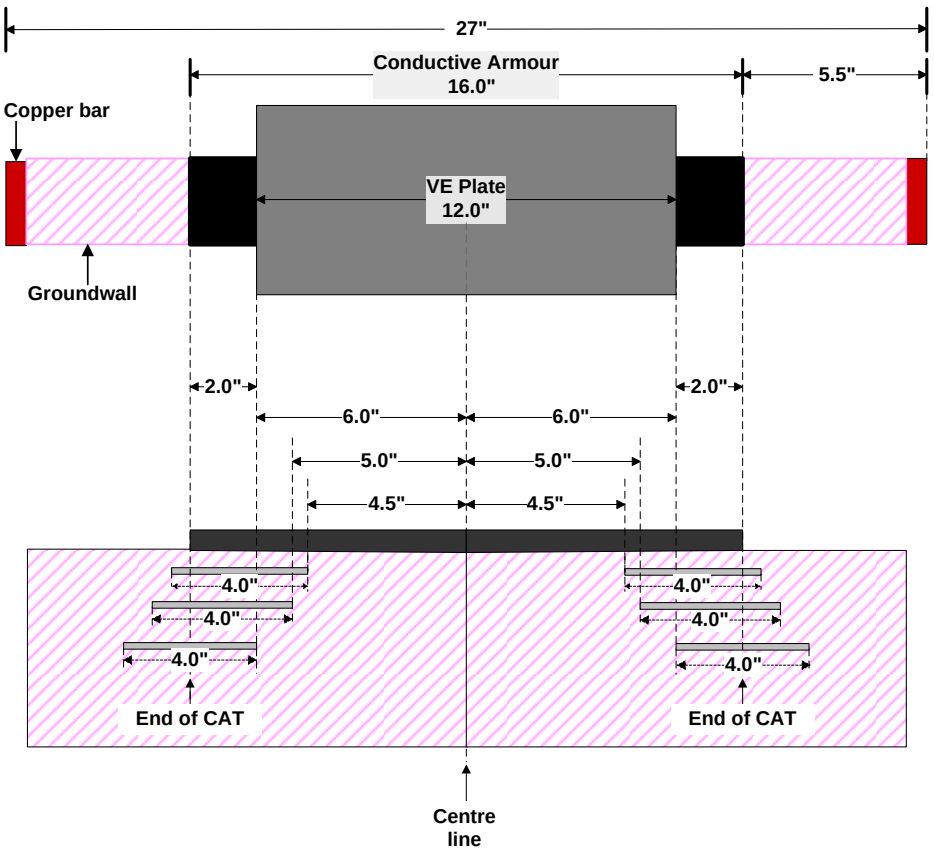

Figure 3-52: Schematic cross-section of the final samples with the capacitive SG used in the pulse qualification test.

As explained previously, the forced heat is generated by strip heaters and transferred through the grounded plates to the insulation system. However, without energization, the temperature distribution along the end portions of the samples is non-uniform because the strip heaters apply heat only to the grounded plates. For example, as shown in Figure 3-53, when the plates are at 155 °C, the temperature on the end portion of the bar sample varies from 132 °C at the slot exit to 100 °C at the end of the CAT. Thus, the temperature at these points are used as the reference temperatures for calculating the temperature rise after the sample is energized with repetitive fast pulse voltage.

Before the test was begun, and for each sample, the PD level was measured according to the procedure presented in Section 2.4.6.3. During the test, power supply voltage and temperature from thermocouples was recorded using a Labview® program developed for this study. In addition, the surface temperature was monitored using an infrared camera, and the surface discharge activity was checked using a corona camera. The test setup and the samples during the testing process are shown in Figure 3-54.

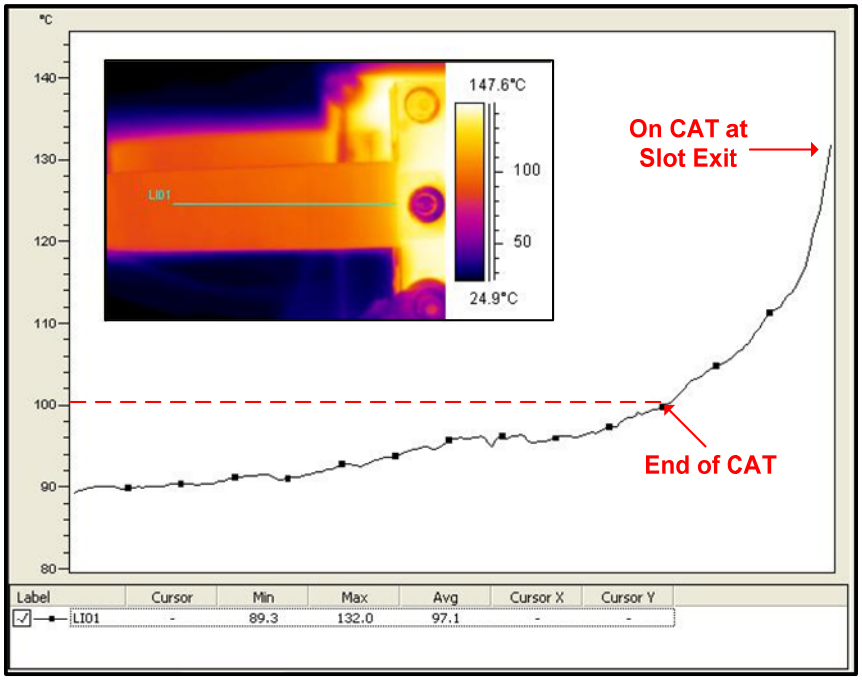

Figure 3-53: Temperature profile along the end portion of a sample with a capacitive SG subjected to 155 °C of forced heat at no applied voltage.

(a) (b)

Figure 3-54: (a) A view of the qualification test setup; (b) samples subjected to 155 °C of forced heat and energized with a repetitive impulse voltage during the qualification test.

The qualification tests were performed according to the following steps:

Step 1:

All samples were subjected to 155 °C of forced heat and a repetitive impulse voltage of 20 kV_{pp} with a 4 kHz pulse repetition rate for 100 hours. The average temperature rises at the end of the CAT on the conventional SGT and the proposed capacitive SG was 60 °C and 9 °C

respectively. No surface discharge and no colour change in the SGT were observed and all samples passed the test. In addition, no significant variation occurred in the PD levels.

Step 2:

Step 1 was repeated twice with the same conditions. All samples passed the test with no visible surface corona. The temperature rises were similar to those that observed during the step 1. However, as shown in Figure 3-55 (a), the colour of the SGT at the end of the CAT on the samples changed slightly on the conventional SG system and no significant change in the PD level was observed.

Step 3:

All samples were subjected to 155 °C of forced heat and a repetitive impulse voltage of 25 kV_{pp} with a 5 kHz pulse repetition rate for 100 hours. All samples passed the test with no visible surface corona. The temperature rises at the end of the CAT on the conventional SGT and the proposed capacitive SG were, on average, 126 °C and 20 °C respectively. As shown in Figure 3-55 (b), the colour of the SGT at the end of the CAT changed considerably on the samples with the conventional SG system. No significant change in the PD levels for all the samples was observed.

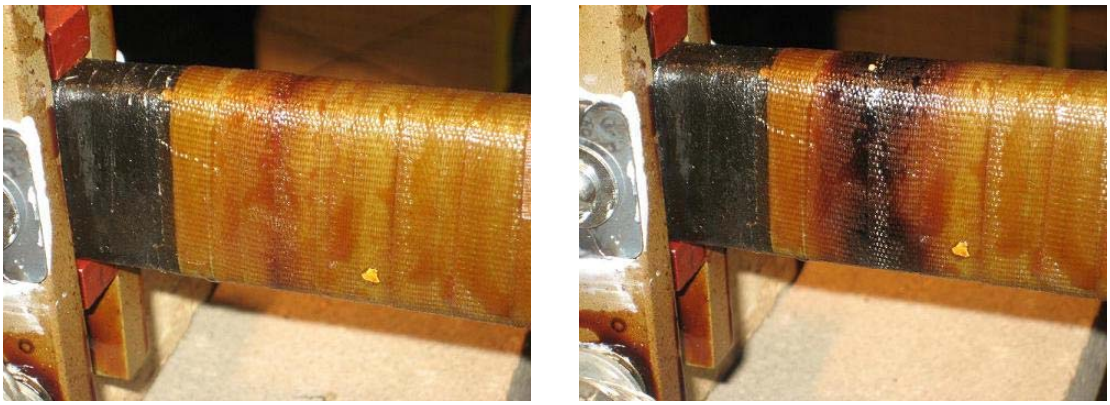

(a) (b)

Figure 3-55: A sample with the conventional SGT after the qualification tests: (a) 300 h energized at 20 kV_{pp}, 4 kHz impulse voltage; (b) 300 h energized at 20 kV_{pp}, 4 kHz with an additional 100 h at 25 kV_{pp}, 5 kHz impulse voltage.

Chapter 4
Discussion

4.1 Introduction

In this chapter the dc and ac material properties of the CAT and the SGT presented in Chapter 3 are analyzed and their dependence on the electric field, frequency, and temperature are discussed. The effect of VPI manufacturing of the form-wound coils on the material properties and performance of the CAT are detailed. Methods of computing the electric field along the SG system are presented and compared. Based on experimental and computational work, the performance of a conventional SGT under repetitive fast pulses is evaluated. The influence of characteristics of repetitive pulse on the development of electrical and thermal stresses is summarized. It is shown that precise coupled electro-thermal FEM modelling, using appropriate ac and anisotropic material properties, can be developed and used to produce accurate electric and thermal field analyses. Several capacitive SG schemes with embedded floating conductive foil/tape layers are discussed with respect to their performance at 60 Hz and with pulses. The developed capacitive SG system is introduced as an alternative to a conventional SG system for inverter-fed motor coils.

4.2 Dielectric Properties and Manufacturing of CAT

The dc resistivity of CAT increases significantly after the VPI process. The measured surface resistivity of the CAT used in this study is 204 Ω/sq before taping and 1640 Ω/sq after manufacturing. In other words, the ratio of increase in the dc resistivity after VPI is about 8, which corresponds to the ratio given in Section 1.5.1.2.

In addition, although the ac resistivity of the CAT is nearly independent of frequency, the dissipation factor of the CAT declines rapidly from a very large value at low frequencies to about 1 to 5 at 2 MHz. In other words, when the frequency increases, the CAT acts less resistive, and its mode changes to capacitive for frequencies above 2 MHz. For both dc and ac fields, the resistivity of the CAT in the thickness direction is much higher than in the longitudinal direction. Since the CAT is a carbon-loaded non-woven polyester fleece conductive tape, the resistivity through the thickness direction is larger than in the longitudinal direction, as expected.

Figure 4-1 is an illustration of a half-lapped CAT. As shown, because the tape is constructed as fleece tape and is lapped, resin can accumulate in the gaps between adjacent laps and can also

form a thin layer on the surface. In addition, the contacts between the laps are not perfect, and due to the penetration of the resin, a high contact resistance is formed that strongly influences resistance in both the longitudinal and thickness directions. A path of resin from the bottom to the top of a CAT layer can also allow the electric field to concentrate in the gaps between the laps.

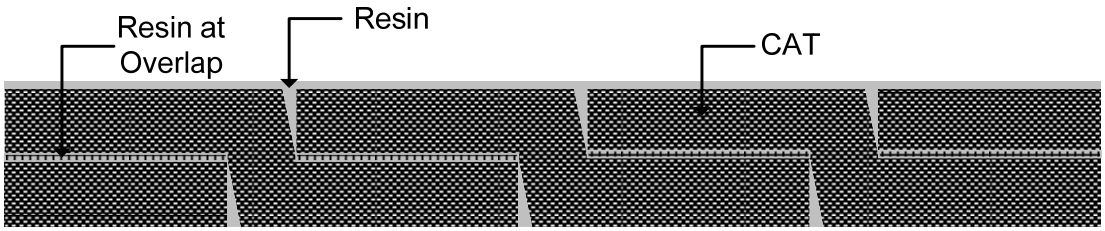

Figure 4-1: Illustration of a half-lapped CAT (not to scale).

Since the CAT is in contact with the stator core, or grounded plate for the samples used in this study, the contact resistance is very important because it can influence the performance of the CAT, particularly for high frequencies and pulses. Figure 4-2 shows how the gaps can fill with resin, or alternatively, unfilled leaving an air gap, to be formed between the coil and the stator core. The contact resistance can vary because of changes in several parameters, such as frequency, contact pressure, temperature, and the formation of a resin layer or an air gap between the outer surface of the coil/bar and the slot. Figure 4-3 shows the frequency dependency of the contact impedance (series capacitance and resistance) between the grounded plate and the CAT at a distance of 25.4 mm from the plate for four samples: A, B, C, and D. As can be seen, the contact resistance of samples C and D is much higher than that of samples A and B. The contact resistance of samples A and B is almost independent of frequency up to 100 kHz, but for samples D and C, it is strongly dependent on frequency. As previously mentioned, the contact impedance can be strongly influenced by the penetration of resin or by the formation of an air gap at the contact during manufacturing.

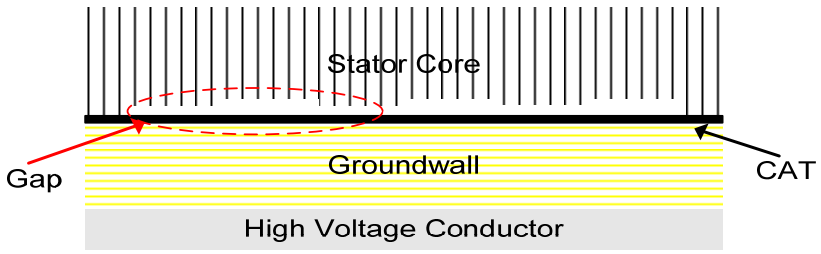

Figure 4-2: Illustration of the formation of gaps between the coil and the stator core.

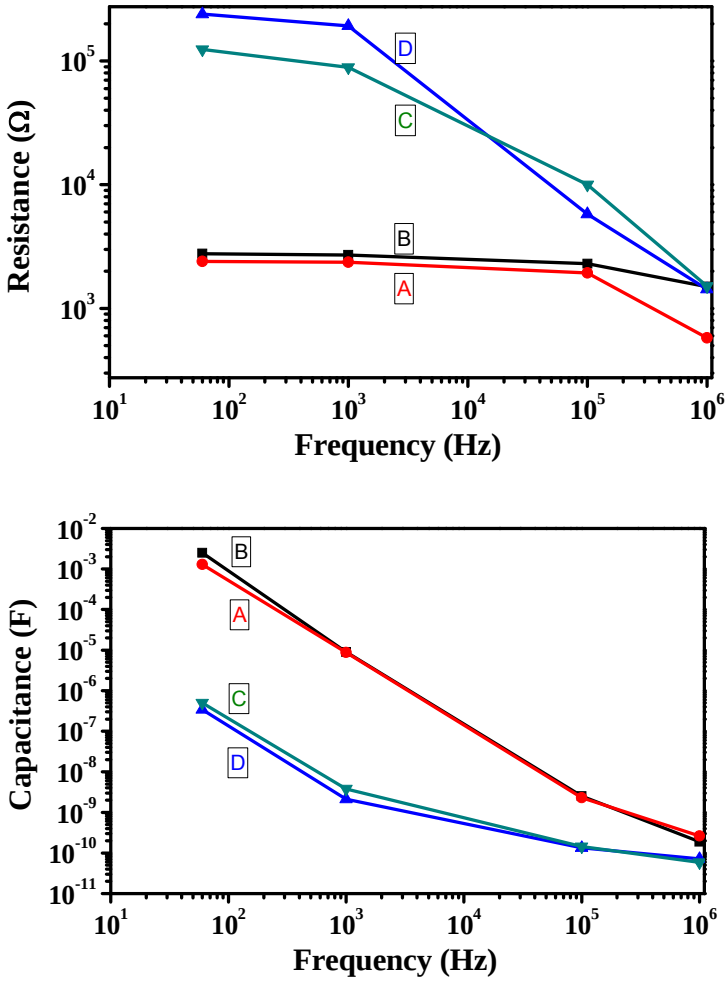

(a)

(b)

Figure 4-3: Contact impedance between the CAT and the grounded plate for four samples A, B, C, and D: (a) the contact resistance (b) the contact capacitance.

4.3 DC and AC Dielectric Properties of the SGT

In the longitudinal direction, the dc surface and volume resistivity of the SGT as a function of the electric field were described as exponential relationships in (3-1) and (3-2). A 2/3 exponent is in agreement with previously published work [52, 62]. However, it must be noted that other mathematical expressions can also be fitted to the measured data that might have higher accuracy or less numerical convergence problem. For example, a fifth or sixth degree polynomial function such as (4-1) can result in a regression square (R^2) very close to 1. In some cases, expressing the conductivity as a low degree polynomial function of the electric field might also result in better convergence in time harmonic or transient FEM analyses.

$$\rho_{x,y}(E_{x,y}) = a_6.E_{x,y}^6 + a_5.E_{x,y}^5 + a_4.E_{x,y}^4 + a_3.E_{x,y}^3 + a_2.E_{x,y}^2 + a_1.E_{x,y} + a_0 \quad (4\text{-}1)$$

The dc volume resistivity of the SGT not only is a function of the electric field, but also depends on the temperature. For a low electric field, the SGT resistivity has a negative temperature coefficient; however, with an electric field of about 400 kV/m it acts almost independent of temperature, and for a field above 450 kV/m, the temperature coefficient becomes positive.

The dc volume resistivity of the SGT in the thickness direction can be expressed as a quadratic equation such as (4-2) with a R^2 value of 0.992. A comparison of Figures 3-11 and 3-13 reveals that the nonlinearity of the dc volume conductivity in the thickness direction is less than that in the other direction.

$$\rho_{y-dc}(E_y) = -1.34\times10^{-4}\,E_y^2 - 4.3\times10^{1}\,E_y + 5.78\times10^{7} \quad (\Omega.m) \quad (4\text{-}2)$$

DC surface and volume resistivity are the most common parameters used in industry; however, for FEM modelling, volume conductivity is the parameter generally applied. The ac volume conductivity has therefore been adopted for the ac characterization of the SGT.

From Figures 3-11 and 3-13, it can be observed that the variation in the SGT conductivity with a dc electric field is much higher than that obtained with ac, particularly at high frequencies. In other words, at high frequencies, the conductivity varies linearly with the electric field. For example, at 3 kHz, linear equation (4-3) can be fitted to the measured data with a R^2 value of 0.992.

$$\sigma_{x-3kHz}(E_x) = 8.23\times10^{-11}\,E_x + 2.02\times10^{-5} \quad (S/m) \quad (4\text{-}3)$$

Temperature has little effect on the conductivity and dissipation factor of the SGT at high frequencies. For example, as shown in Figure 4-4, at 3 kHz and 5 kHz, the conductivity varies only slightly at elevated temperatures.

As mentioned in Section 2.3.1, the sample with the configuration shown in Figure 2-3 was used to measure both the dc and ac volume conductivity of the CAT and the SGT in the longitudinal direction. According to this method, the impedance of the groundwall and stray capacitance can contribute to the measured impedance as shown in Figure 4-5. Although, the contribution for dc and low frequencies is negligible, at high frequencies, it is comparable to the actual SGT impedance, and it must be taken into account.

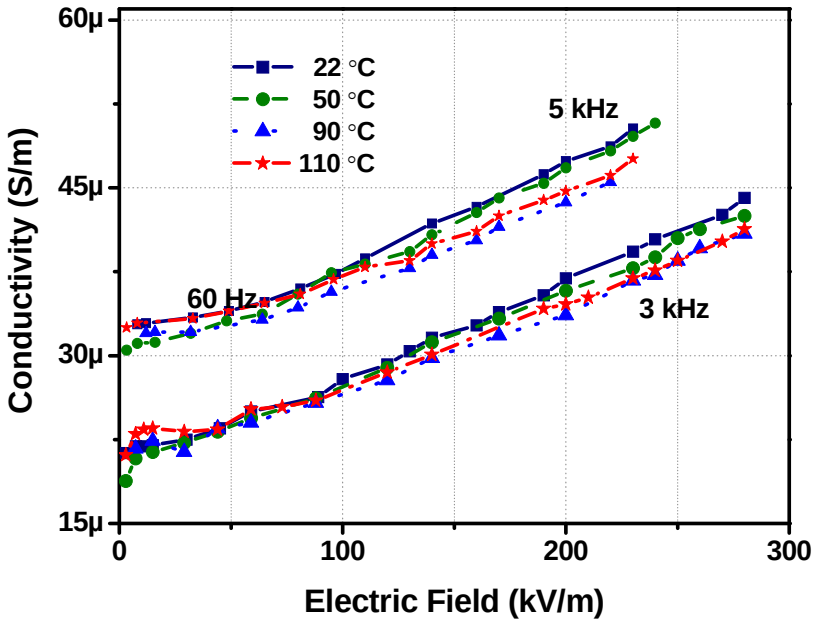

Figure 4-4: Variations in the conductivity of the SGT in the longitudinal direction as a function of electric field at various temperatures and at 3 kHz and 5 kHz frequencies.

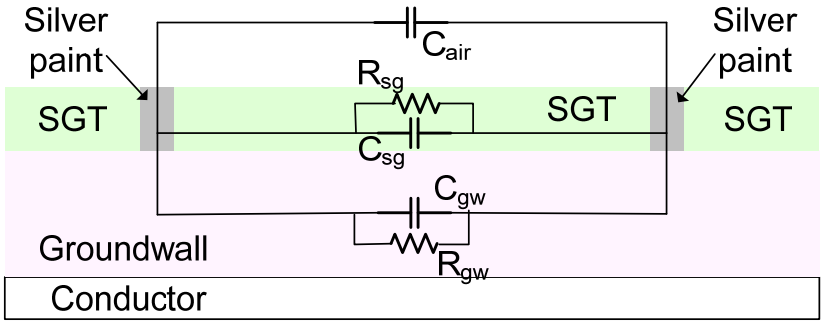

Figure 4-5: Equivalent circuit of SGT for measurements in the longitudinal direction as shown in Figure 2-3.

4.4 Performance of the Conventional Resistive SG System

4.4.1 Space Charge Limited Field

According to the space charge limited field (SCLF) theory, the maximum tangential component of an electric field can be predicted for an ac electric field with a frequency f [54, 145]. The electric field in a dielectric is limited to a value, E_{lim}, determined approximately according to the conditions that

$$\sigma(E_{\lim}) = \varepsilon\,\omega \tag{4-4}$$

where, σ and ε are respectively the electrical conductivity and the permittivity. *σ(E)* is itself a function of the electric field (E) that can be defined as follows:

$$\sigma(E) = \sigma_0 . exp(k|E|^n) \tag{4-5}$$

In an ac steady state electric field, the current density in the dielectric consists of two parts: the resistive current density (J_R), which is in phase with E, and the displacement (capacitive) current density (J_C), which is in quadrature with E. In a general form, J_R and J_C as a function of the electric field are defined in (1-1). At steady state, the total current density *(J)* in phasor form is expressed as

$$J = J_R + j J_C = \sigma E + j \varepsilon\omega E \tag{4-6}$$

Although both the conductivity and permittivity are normally dependent on temperature, when the maximum field is being predicted, this dependency is not considered. Permittivity is often a weak function of the field and thus can be considered constant.

The grading behaviour of the dielectric is determined by the relative values of the resistive and capacitive current densities: thus $\varepsilon\omega$ and $\sigma(E)$. For low electric field, $\varepsilon\omega$ is generally larger than $\sigma(E)$, which means that the grading is dominated by the capacitive current or that the system is capacitively graded. However, for high electric fields, the resistive current increases significantly and can become greater than $\varepsilon\omega$. When this situation occurs, the grading is dominated by the resistive conductivity, and therefore, the system is resistively graded, and the surface potential is uniformly distributed. Based on these considerations, it can be concluded that the field in a dielectric will be limited to a value E_{lim}, determined approximately by the conditions that $\sigma = \varepsilon\omega$, because for higher fields, $\sigma(E)$ will increase and will dominate the field grading [145].

Using an alternative approach, and in a high electric field region, the conductivity will become untenably high unless the dielectric relaxation time constant ($\tau = \varepsilon/\sigma$) becomes comparable to the time constant of the applied voltage, which means that space charge formation in the dielectric must limit the field. If the field is not limited in this way, it will become so high that the conductivity will increase to the point that it will be the limiting factor [54]. This condition can be expressed as follows:

$$\tau = \frac{\varepsilon}{\sigma} = \frac{1}{c.\omega} \quad \Rightarrow \quad \sigma(E) = c\ \varepsilon\omega \tag{4-7}$$

where c is a constant that matches the time constants. Thus, inserting the formulation of the field dependent conductivity from (4-5) into (4-7):

$$ln(\sigma_0)+k|E|^n=ln(c)+ln(\varepsilon\omega)\Rightarrow E=\left[\frac{1}{k}\left(ln\left(\frac{\varepsilon\omega}{\sigma_0}\right)+ln(c)\right)\right]^{(1/n)} \tag{4-8}$$

With typical values for σ_0 and $\varepsilon\omega$, the result *(E)* is relatively insensitive to the coefficient c. Thus, the formulation $\sigma = \varepsilon\omega$ can result in a good approximation of the maximum electric field in the nonlinear field dependent dielectric.

Based on (3-2), the conductivity as a function of the electric field can be expressed by (4-9).

$$\sigma_T(E)=\sigma_{0T}.\exp\left(k_T.(E)^{2/3}\right) \tag{4-9}$$

where k_T and σ_{0T} at each temperature are taken from Figure 3-5, the latter equating to the hypothetical conductivity at zero stress. Based on (4-4) and (4-9), the limited field is

$$E_{\lim}=\left[\frac{1}{k_T}\ln\left(\frac{\varepsilon\omega}{\sigma_{0T}}\right)\right]^{(3/2)} \tag{4-10}$$

The graphical illustration for finding E_{lim} is shown in Figure 4-6. For example, at 60 Hz and at 22 °C, the space charge limited field (SCLF) is about 440 kV/m.

To evaluate the electric field more accurately in different directions, either on the surface of the stress relief system, which is surrounded by media, or within the dielectric, a transient finite element model is required in order to solve Poisson's equation for field dependent conductivity and time dependent voltage.

As discussed, the SCLF theory can predict only the tangential component of the limited electric field within the dielectric; it cannot predict the total electric field in the air adjacent to the surface of the tape, which is in fact, the vector sum of the tangential and normal components (the tangential field is continuous across the boundary). Due to the law of refraction, the normal component of the electric field can be significant at the triple point of the conductor, the dielectric and the air, and also where there are irregularities in the surface. In addition, the validity of the SCLF theory at high frequencies must be confirmed, because the mechanisms of the conduction and space charge formation, such as interfacial and dipolar polarization, are frequency dependent.

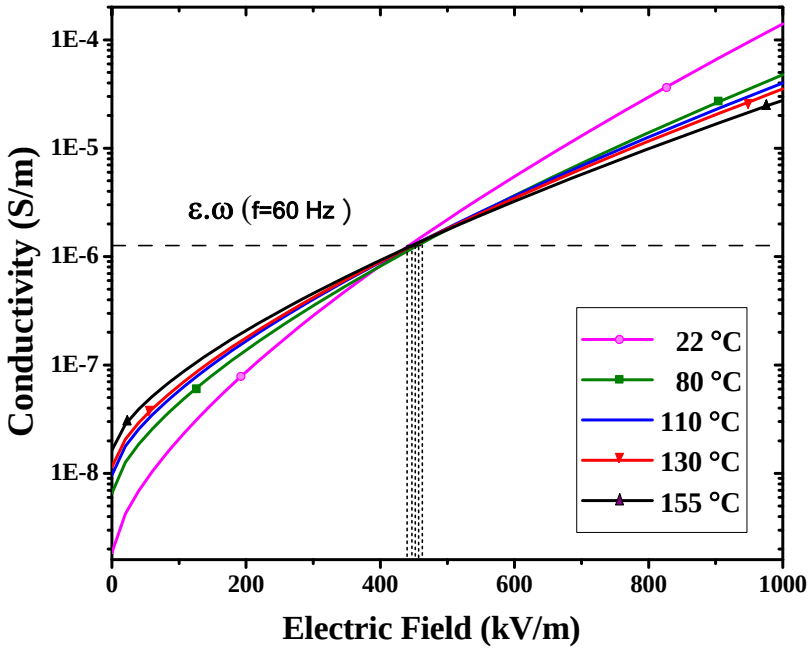

Figure 4-6: Space charge limited field for the exponential field dependent dc conductivity of the SGT at various temperatures.

4.4.2 Computation of Surface Electric Field

It has been shown that the gradient of the measured surface potential is a simple method of computing the tangential electric field along the SG region at 60 Hz. In Figure 3-17 at a nominal voltage (8 kV_{rms} phase-to-ground) and in Figure 3-18 at 130 % of the nominal voltage, the maximum tangential field shows a positive thermal coefficient. At lower voltages corresponding to lower stresses, a negative thermal coefficient is observed. These results agree with the discussion in Section 4.3 with respect to the effect of temperature on the resistivity of the stress grading tape for several electric stresses.

It is also quite clear that temperature does not play a significant role in the distribution of the electric field. This result corresponds closely to the measured dc resistivity of the stress grading tape, as shown in Figure 3-5, which indicates that temperature has no effect on resistivity at an electric stress of about 420 kV/m, which is very close to the space charge limited field of 440 kV/m.

A comparison of the tangential electric field from the FEM simulations and the gradient of the measured surface potential are shown in Figure 4-7 at nominal voltage and at room temperature. For the simulations, two cases were studied: the first with dc isotropic and the second with ac anisotropic material properties. The peaks of the tangential electric field in both simulations are

nearly identical; however, with the ac modelling, the falling slope of the electric field is slower than in the other case, which is the reason that the electric field is enhanced slightly again at the end of the SGT. An extreme enhancement of the electric field at the end of the SGT can be observed in a hi-pot test, which can be explained because of the ac anisotropic simulation [116]. The peaks shown in the experimental results are higher than those determined by the simulations. The discrepancy can be attributed to the way the probe measures the surface potential.

The probe is basically a charge coupled device in which the charge induced on the probe is opposite in polarity to the charge on the surface beneath the probe. In a region of uniform charge and therefore uniform potential, the probe accurately measures the surface potential. However, where the surface charge is highly non-uniform, the charge detected by the probe is an average of the charge on the surface beneath the probe. In regions where the potential/electric filed is highly divergent, for example, at the transition between the CAT and the SGT, the accuracy of the probe is therefore not very great. An estimate of the accuracy cannot be given in this situation; however, it can be stated that the correct profile of the potential, and therefore of the electric field, is maintained.

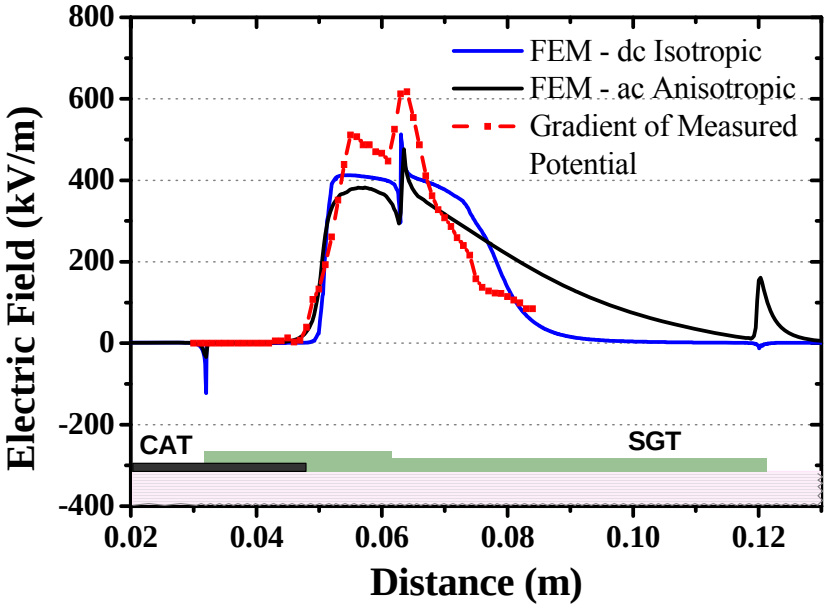

Figure 4-7: Comparison of the experimental and the simulated tangential components of the surface electric field at nominal voltage and at room temperature.

For the computation of the electric field from the surface potential profile along the conventional SG system, two concepts, as illustrated in Figure 4-8, can be addressed: the maximum and the average electric field in the longitudinal direction. The slope of the line from

the ground to the maximum measured potential represents the average electric field ($E_{x\text{-}avg}$). In addition, the slope of the line tangential to the steepest part of the surface potential profile indicates the maximum tangential electric field ($E_{x\text{-}max}$).

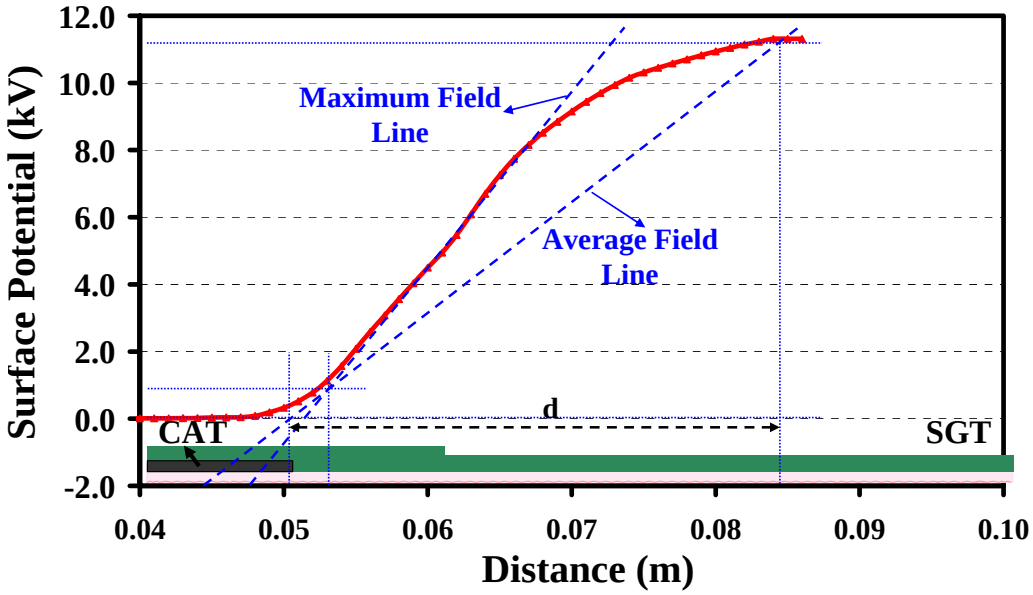

Figure 4-8: Illustration of the computation of the maximum and average electric fields from the surface potential profile.

As discussed in Section 3.3.1.2, the total electric field ($E_{t\text{-}max}$) can be considerably larger than the tangential component. According to the simulations, Figures 4-9 and 4-10 depict ($E_{x\text{-}max}$) versus ($E_{x\text{-}avg}$) and the ($E_{t\text{-}max}$) versus ($E_{x\text{-}max}$) for each of three frequencies, 60, 3 kHz, and 5 kHz. At each frequency, the percentage ratio of ($E_{t\text{-}max}$) to ($E_{x\text{-}max}$) varies slightly from 125 to 135 percent.

The distance for which the surface potential rises from ground to maximum potential is one of the important factors for designing the length of the SGT. This distance, "d" in Figure 4-8, called the "potential rise distance," increases directly with the amplitude and inversely with the frequency of the applied voltage. In the simulations, as shown in Figure 4-11, the maximum tangential field varies with the potential rise distance. At the higher frequencies, the potential rise distance decreases at a specific field. Based on this study, the ratio of the maximum tangential field ($E_{x\text{-}max}$) to the average field ($E_{x\text{-}avg}$) versus the potential rise distance can be extracted, as shown in Figure 4-12. Using this plot the maximum tangential field can easily be predicted from the measurement of the surface potential.

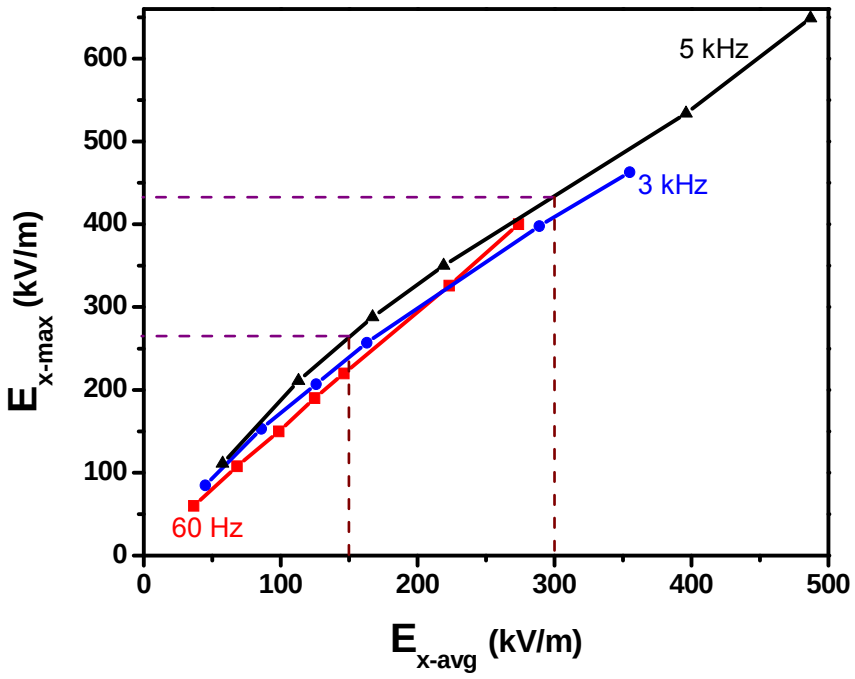

Figure 4-9: Maximum tangential field ($E_{x\text{-}max}$) versus the average field ($E_{x\text{-}avg}$) for three frequencies along the conventional SG system.

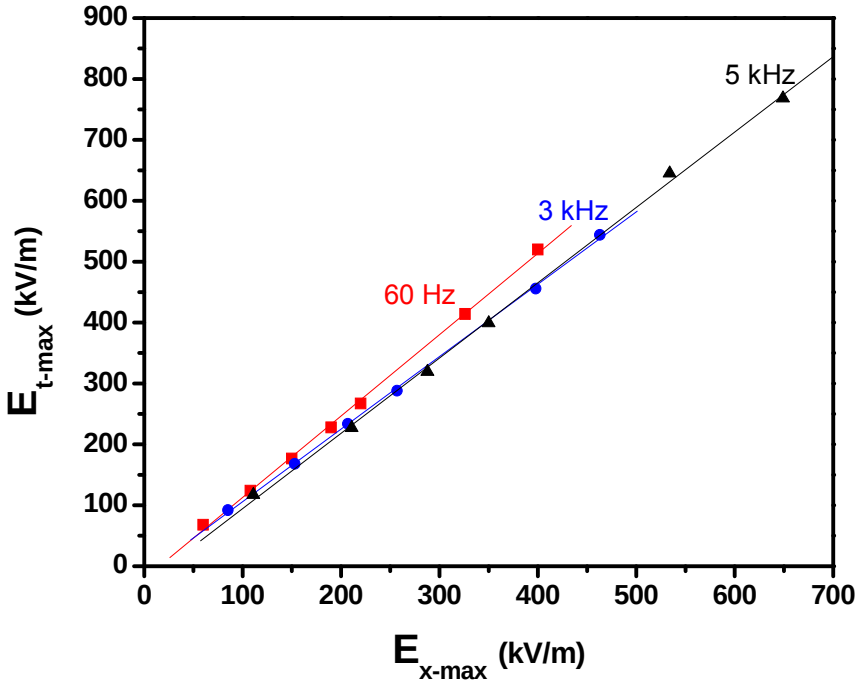

Figure 4-10: Maximum total field ($E_{t\text{-}max}$) versus the maximum tangential field ($E_{x\text{-}max}$) for three frequencies along the conventional SG system.

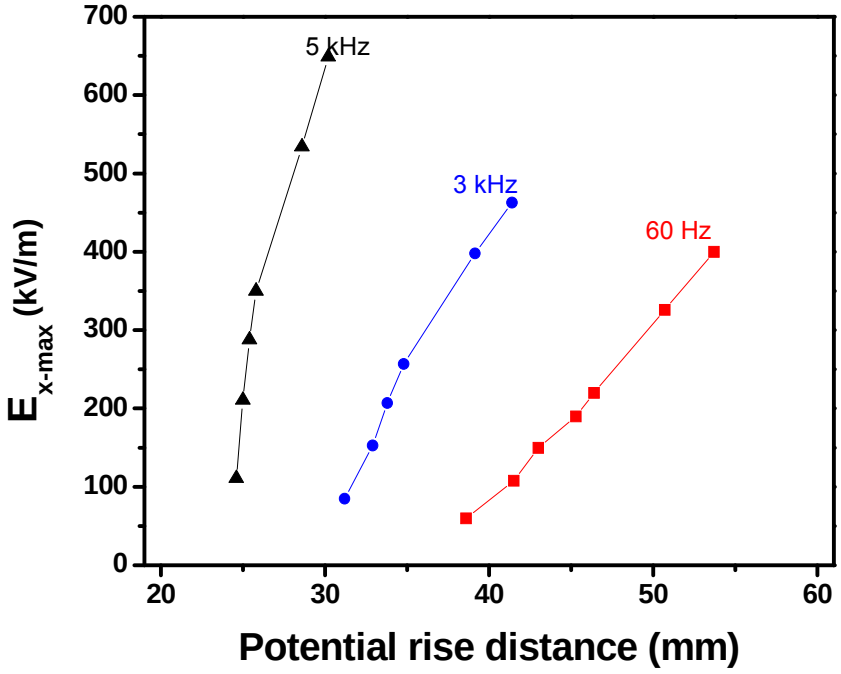

Figure 4-11: Maximum tangential field ($E_{x\text{-}max}$) versus the potential rise distance (d).

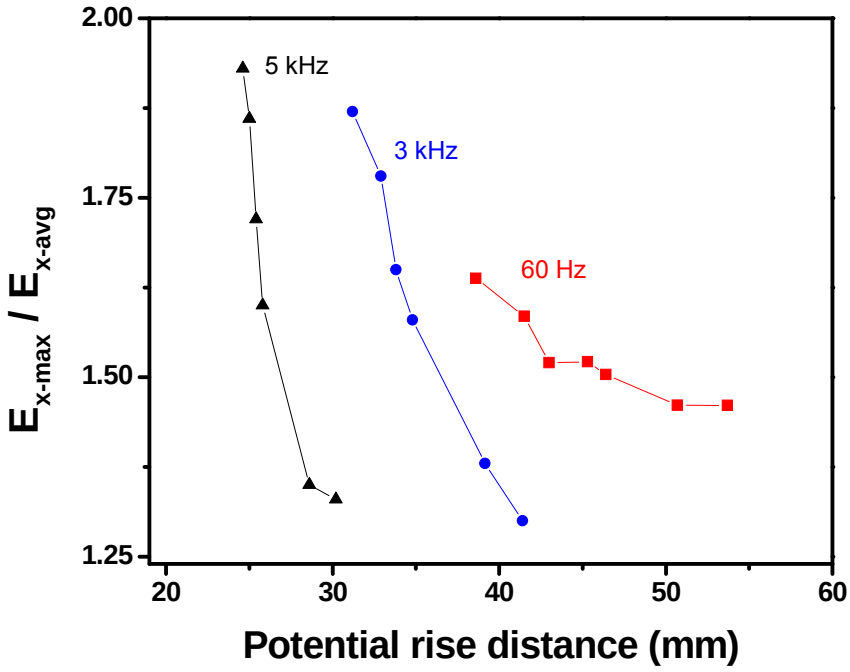

Figure 4-12: Ratio of the maximum tangential field ($E_{x\text{-}max}$) to the average field ($E_{x\text{-}avg}$) versus the potential rise distance for three frequencies.

4.4.3 Conventional SG System Subjected to Fast Pulses

As shown in Chapter 3, elevated electrical and thermal stresses can develop on the CAT and SGT of form-wound coils when the coils are energized by repetitive fast pulses. The intensity of these stresses generally depends on the properties of the CAT and SGT materials; pulse characteristics; and the geometry of the coil; and the contact between the coil and the stator slot, or grounded core.

In Figure 3-25, two regions of the high electric field stand out and correspond to the locations where the hot spots develop: one is in the SG region and the other is on the conductive armour immediately after the slot exit. These results are in good agreement with the actual position of the hot spots observed as shown in Figure 3-37. The electric field is enhanced at the slot exit during the rise-time of every impulse voltage that is associated with very high frequency components. This high electric field increases the resistive loss in this region. In addition, due to differences in the dielectric constants, the electric field can be greatly enhanced in the small air gaps, or voids, in this region, which leads to partial discharge (PD) and also increases the local heating. Both of these symptoms are frequency dependent, which translates into a higher repetition rate, higher dielectric loss, and more PD. Another condition that can result from increasing the electric field across the minute air gaps is a high surface discharge current under repetitive fast pulses, particularly from the SG region [96].

If the conductivity of the CAT in different directions is not sufficiently high, the voltage of the coating can be increased because of the surface discharge. This effect may provide a high electric field beyond the PD inception level in the air. However, the conductivity of the CAT used in this study, particularly in the longitudinal direction, is fairly high and varies slightly with frequency [116]. This contradiction can be explained using 3D-FEM modelling. Figure 4-13 illustrates a cross section of the bar sample that was modelled in the 3D-FEM simulation. The air gaps between the CAT and the grounded core at the corners are indicated by dashed circles that cannot be shown in 2D modelling. The high-frequency harmonics associated with the fast rise time pulses enhance the electric field in these sharp gaps, particularly at the tape overlaps, as discussed in Section 4.2.

The dashed circle in Figure 4-14 (a) shows the edge of the corner near the slot exit. The tape overlaps in this area, which is precisely the location of the hot spots seen in the temperature profile Figure 4-14 (b). Since the taping method of the CAT is the same for the conventional SG and the capacitive SG systems, this phenomenon was observed for both systems, as discussed in Section 3.4.3 and shown in Figure 3-50.

The contact resistance between the CAT and the grounded core is another important factor that has a significant influence on stress enhancement at the slot exit. When a repetitive pulse voltage is applied to the four samples studied in Section 4.2, visible corona was observed only at the slot exit of samples C and D, which exhibited high contact resistance. The temperature rise at the slot exit on these samples was much higher than for samples A and B.

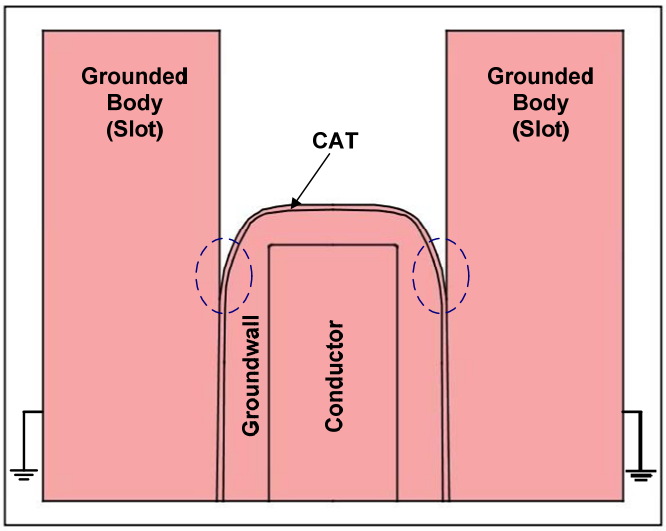

Figure 4-13: Half cross section of the motor bar geometry used in the 3D-FEM simulation.

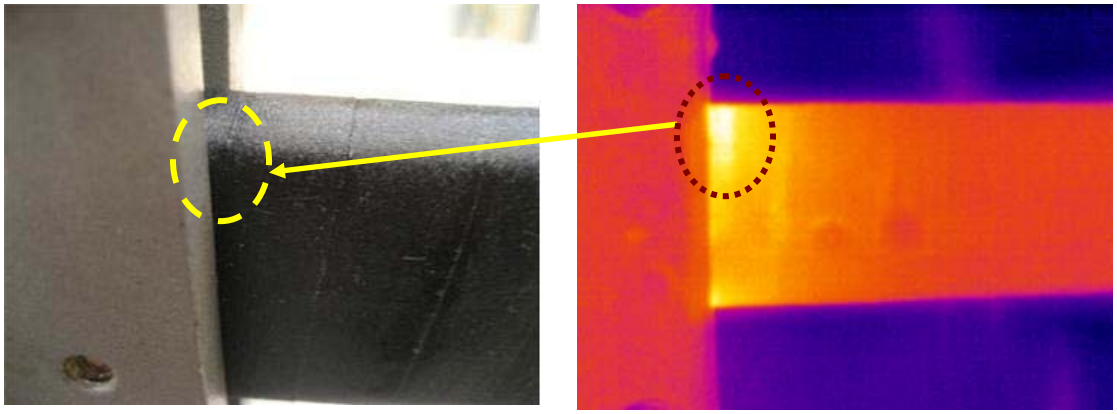

(a) (b)

Figure 4-14: (a) Slot exit for one sample with a tape overlap at the corner near the slot exit; (b) Hot spot that developed in the area indicated by a dashed circle in (a) when the sample was energized with a repetitive fast pulses.

Through experimentation and computational analyses, the effects of the pulse waveform and the pulse characteristics on the development of thermal stress on the CAT and the SGT were comprehensively studied. It was shown that the temperature rise and its profile in the end portion of a 13.8 kV motor bar with PWM voltage waveform is almost identical to a unipolar square

wave voltage with a 50 % duty cycle if the voltage peaks, switching frequencies (repetition rates), and rise and fall times of the pulses are the same. In addition, it was shown that for any train of square wave pulses, an equivalent repetitive impulse voltage exists that can produce the same amount of heat and the same temperature rise in the SG region.

Prior to this present study, the effects of the pulse parameters on the hot spots that develop at the slot exit and in the SG region was not understood well. One study showed that electrical losses in the SGT were independent of the pulse rise time [66]. The study was conducted using specimens that consisted of copper tubes wrapped with groundwall insulation, CAT, and SGT. Because the geometry of the specimen used in that study was completely different from the actual motor coil's geometry, the thermal stress on the CAT at the slot exit could not be investigated appropriately. However, in the present study, the geometries of the motor bar samples and of the ground connection are very close to those of actual coils.

As shown, the rise time of the pulses has little influence on the loss in the SGT, particularly for lower switching frequencies. However, the effects are significant with respect to the hot spot on the CAT at the slot exit. Electric field enhancement and surface discharge are the main causes of hot spots in this area: both are very sensitive to the pulse rise time and the repetition rate. With fast pulses, the maximum thermal stress is exerted on the CAT at the slot exit. However, with slower pulses, e.g., more than 1 μs, the SGT is exposed to the maximum thermal stress.

It has been analytically and experimentally shown that two sinusoidal voltages, having frequencies f_1 *and* f_2 and amplitudes A_1 and A_2, respectively, (f_1 , A_1) and (f_1 , A_2), can represent a train of impulses that yields the same heat generation in the CAT and the SGT. The frequency f_1 is equal to the signal repetition rate (switching frequency). However, f_2 can be assumed to be a fixed frequency that represents the high-frequency components. In this study, a value of 50 kHz was selected for f_2 based on the experimental tests, and the amplitudes A_1 and A_2 can be determined from Table 3-1. According to the developed method, the thermal performance of the CAT and the SGT can be evaluated separately with a single HF-HV sine wave corresponding to the worst possible scenario in which a PWM voltage produces. The worse possible scenario for the CAT is the fastest rise time of the pulses at the maximum repetition rate; for the SGT it is the lowest rise time.

Another benefit of the method introduced is with respect to coupled electro-thermal FEM modelling. Simulating SG systems under repetitive fast pulses has been a significant challenge using traditional transient coupled electro-thermal FEM modelling. However, with the developed method, two static coupled electro-thermal FEM analyses can be used instead, and the equivalent

temperature rise can be determined through the use of the superposition principle. For each simulation, the corresponding ac material parameters provided in the previous stages were applied. To verify the developed method, high-frequency (HF) tests were carried out for two different frequency ranges. The close agreement of the simulation results with the experimental results verified the validity of both the developed method and the measured material properties.

4.5 Developed Capacitive SG System

In previous sections, the poor performance of the conventional resistive SG system under repetitive fast pulses was shown and discussed. The development of thermal stress is the crucial problem associated with a traditional SG system under pulse application. Using a capacitive SG system can be a practical alternative that can significantly mitigate thermal stress. This research examined several capacitive SG schemes based on conductive foil or tape embedded within the groundwall insulation. To evaluate the performance, experimental tests were carried out at 60 Hz and with pulse applications.

The developed systems worked perfectly at 60 Hz. The surface potential measurement showed that the voltage rises smoothly from ground potential to the maximum phase voltage. The gradient of the surface potential provided the tangential electric field. The profile and the maximum of the electric field both depend on the number and position of the foil layers. Using FEM simulations, the number and position of the internal floating layers were determined. For 13.8 kV motor coils, three layers of aluminum foil with the positions proposed can effectively control the electrical stress along the end portion of the coils. However, with this method, the grading of the stress at the end of the CAT is limited because at least one layer of mica tape must be applied between the CAT and the top foil layer. The surface corona inception voltage was about 22 kV for the samples with the developed capacitive SG system; all of which passed a hi-pot test at 28.6 kV ($2U_n+1$) for one minute. The results of the FEM simulations corresponded well with the experimental results.

The application of CAT as a conductive floating layer for the developed capacitive SG schemes was also studied. The performance of this design at 60 Hz was very close to the design that incorporated aluminum foils, which demonstrates that the CAT at 60 Hz behaves similarly to aluminum foil.

The temperature rise along the developed capacitive SG system exposed to repetitive fast pulses was much less than along the conventional SGT. It is therefore concluded that the developed capacitive SG system can effectively mitigate localized thermal stress in an SG

system. The repetition rate and rise time of the pulses have little influence on the temperature rise along the developed capacitive SG system. For the reason discussed in the previous section with respect to the stress that develops at the corner edge of the slot exit, the developed capacitive schemes using CAT embedded within the groundwall performed poorly compared to the schemes that used aluminum foil.

The developed capacitive SG system subjected to fast pulses can mitigate appropriately the electric field at the triple point; however its ability to control the electrical and thermal stress at the slot exit or inside the slot is also limited. As discussed in the previous section, the stress that develops in these regions depends on the geometry and the contact resistance between the CAT and the grounded core and the operating temperature. Mitigation of the stress in those regions must therefore be studied separately using a modified coil and/or slot geometries and taping methods. Suggestions for future work in this respect are presented in Chapter 5.

4.6 Qualification of the Developed Capacitive SG System

The results from the testing steps described in Section 3.5 are summarized in Table 4-1. A typical temperature profile recorded during the test is shown in Figure 4-15. The maximum temperatures in three regions were recorded: in the core (T_{core}); at the slot exit (T_1); and at the end of the CAT (T_2). The difference in temperature before and after the samples were energized is labelled Δ. For both SG systems, the temperature rises in the core and CAT at the slot exit are small and are nearly identical; however, a significant rise in temperature manifested as hot spots was observed in the conventional SGT but not in the developed capacitive SG system. These hot spots thermally affected the insulation as evidenced by colour changes in the SGT. For both SG systems, no surface discharge was observed during the test, and no significant variation in the PD level occurred after the test had been performed.

According to the results obtained from the test, the developed capacitive SG system passes all of the test-pass criteria recommended by IEC/TS 60034-18-42. The technical specifications recommend that the samples be subjected to a 100 h impulse voltage test and that the voltage impulse be at least 1.3 times the magnitude of the voltages to be withstood in service. As previously described, in the tests performed in this study, more severe stresses were applied with respect to both the level of the stresses, which are assigned for moderate category, and the duration of the test.

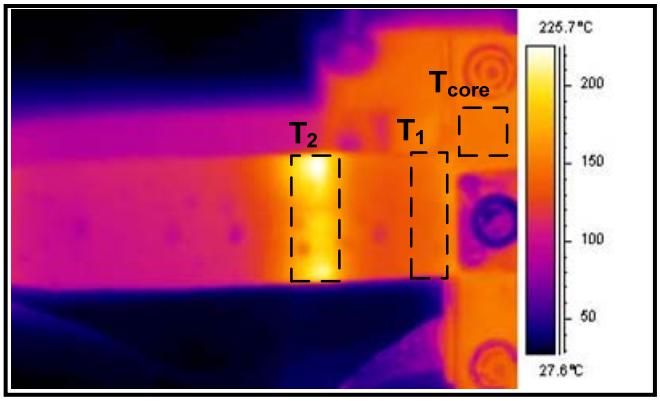

Figure 4-15: A typical surface temperature profile during the qualification tests. The maximum temperature was recorded in the dashed areas.

Table 4-1: Summary of the results of the qualification tests.

Samples	Repetitive Impulse Voltage	Time (h)	T_{core} / ΔT_{core} (°C)	T_{max1} / ΔT_{max1} (°C)	T_{max2} / ΔT_{max2} (°C)	Pass / Fail
R1 – R5	20 kV_{pp} @ 4 kHz	300	158 / 3	147 / 15	160 / 60	P
C1 – C5	20 kV_{pp} @ 4 kHz	300	158 / 3	142 / 10	109 / 9	P
R1 – R5	25 kV_{pp} @ 5 kHz	100	166 / 11	166 / 34	226 / 126	P
C1 – C5	25 kV_{pp} @ 5 kHz	100	165 / 10	156 / 24	120 / 20	P

Chapter 5
Conclusions and Suggestions for Future Work

5.1 Conclusions

The material properties of conductive armour tape (CAT) and stress grading tape (SGT) and the method with which they are applied on form-wound motor coils were traditionally designed for power frequency. Repetitive fast pulses from a pulse width modulated (PWM) voltage source converter (VSC) used as an adjustable motor speed drive have adverse effects on a conventional stress relief system. Although these tapes have been applied in order to control the stress and to protect the main insulation of medium voltage motors at 60 Hz, they are exposed to elevated electrical and thermal stresses when the motor is energized with repetitive fast pulses. Under these circumstances, the stress relief system is susceptible to damage, which causes the main insulation to deteriorate and eventually leads to premature motor failure.

Prior to this research, only a few studies had been conducted to investigate the problems associated with stress relief systems subjected to repetitive fast pulse voltages in form-wound motor coil. These studies lacked the understanding of the behaviour of the materials and therefore the analyses of the root causes were incomplete. This research has therefore focused on gaining a comprehensive understanding of the problems associated with the conventional SG systems in PWM-VSC drive-fed motors and on proposing effective and reliable solutions. The conclusions of the work are summarized below:

Experimentally, tests were performed in order to characterize CAT and SGT in dc and ac electric fields. The isotropic dc conductivity properties of CAT and SGT, which are generally the basis of power frequency modelling, do not produce accurate results for repetitive fast pulses and high-frequency voltages.

Electrical conductivity of CAT and SGT in the longitudinal or lapped direction is generally assumed to be the main conduction path of the materials. However, because of the inconsistent thickness and non-uniformity of these taped layers, conduction in the thickness direction is also important for high-frequency applications, particularly where there are surface discontinuities and tape overlaps.

CAT is less resistive at higher frequencies, and its mode changes to capacitive at frequencies above 2 MHz. In dc and ac fields, the resistivity of the CAT in the thickness direction is much higher than in the longitudinal direction.

The anisotropic conductivity of the CAT is very important for analyzing the electric field enhancement at the slot exit because of the fast pulses. In addition, high contact resistance between the CAT and the stator slot, particularly at the slot exit, can significantly enhance the electric field at the point of contact. The tape lapping ratio, the coil corner radius, the stator slot clearance, the slot exit geometry, and the operating temperature are all factors that can influence the intensity of the electrical and thermal stresses on the CAT at high frequencies. With a low contact resistance, the elevated thermal stress on the CAT is negligible at the rated operating temperature.

The variation in the conductivity of the SGT with dc electric field is much higher than that obtained with ac electric field. In other words, the nonlinearity of the SG material decreases as the frequency increases. It has been shown that at high frequencies, e.g., 5 kHz, the conductivity of the SGT is a linear function of the electric field. Moreover, from the variation in the dissipation factor of the SGT in both the longitudinal and thickness directions, it can be concluded that the SGT acts more capacitively, $\tan\delta < 1$, for a very low electric field or at very high frequencies, e.g., 50 kHz. In other words, in these circumstances, the SGT cannot effectively mitigate the surface electric field.

At 60 Hz, temperature does not play a significant role in the maximum surface electric field along the stress grading region, which corresponds well with the dc resistivity characteristics of the SGT. The dc resistivity of the SGT is nearly independent of the temperature at about the space charge limited field (SCLF) level. Below this level, the SGT resistivity has a negative thermal coefficient.

The SCLF theory can predict only the tangential component of the limited electric field within the dielectric and cannot predict the total electric field in the air adjacent to the surface of the tape, which is the vector sum of the tangential and normal components. Due to the law of refraction, the normal component of the electric field, particularly at the triple point (the intersection of the conductor, the dielectric and the air) and also at irregularities in the surface of the tape, can be significant, and it must be taken into account.

For 13.8 kV form-wound coils, the space charge limited field approximately equals the maximum tangential electric field at power frequency and nominal line-to-ground voltage. The

resultant electric field from both the tangential and normal components on the surface of the coil, must be taken into account in the design of an appropriate overlap between the CAT and SGT.

The gradient of the measured surface potential can provide a good estimate of the tangential electric field profile along an SG system at 60 Hz. Electrostatic voltmeters can measure only the potential at dc and low frequencies, i.e., < 100 Hz. However, transient FEM modelling can compute the components of the electric field along nonlinear SG systems for 60 Hz and fast pulse voltages with a reasonably good accuracy.

Through experimental tests and computational analyses, the effects of the pulse waveform and the pulse characteristics on the development of thermal stress on CAT and SGT were comprehensively studied. It was determined that the temperature rise at the end portion of a 13.8 kV motor bar with a PWM voltage waveform is nearly identical to a unipolar square wave voltage with a 50 % duty cycle if the voltage peaks, switching frequencies (repetition rates), and rise and fall times of the pulses are the same. At these conditions, the signal power of both waveforms is almost equal. In addition, the thermal stresses in the SGT due to a unipolar square pulse train and an impulse train with the same repetition rate, peaks, and rise times are not equal; however, for any train of square wave pulses, an equivalent repetitive impulse voltage exists that produces the same amount of heat and the same temperature rise in the SG region. This factor needs to be taken into account when IEC/TS 60034-18-42 is reviewed for revision.

Although the repetition rate of the fast pulses plays a significant role in creating joule heating in the SGT, the pulse rise time has little influence on the loss that occurs in the tape. However, the intensity of the hot spot on the CAT at the slot exit is highly dependent on the rise time. At room temperature and with fast pulses, the maximum thermal stress on the CAT occurs at the slot exit. In addition, at the high frequencies associated with a rise time of less than 1 μs, the CAT does not perform well as a grounded screen: the faster the pulses, the more stress on the CAT at the slot exit. However, with slower pulses, i.e., more than 1 μs rise time, the SGT is exposed to the maximum thermal stress. At an elevated temperature, e.g., the rated operating temperature, and without a high contact resistance, even with faster pulses, the stress concentrates only on the SGT.

In this study, the electrical and thermal fields along the SG system were analyzed using coupled electro-thermal FEM modelling with actual geometries and measured ac material properties. However, adopting transient FEM modelling for the thermal analysis of a train of fast pulses is a difficult challenge. This research suggests a new method for developing the power of signal theory for nonlinear materials. Two static coupled electro-thermal FEM analyses can be

used as an alternative, and the equivalent temperature rise can be determined through the use of the superposition principle. When this new method is used, the results correspond well with the experimental results.

With the developed method, the thermal performance of the CAT and the SGT can be evaluated separately with only a single high-frequency and high-voltage sine wave that corresponds to the worst possible scenario, in which a PWM voltage is produced. The worst possible scenario for the CAT is the fastest rise time of the pulses at the maximum repetition rate, and for the SGT is the lowest rise time.

Due to the complexity of the motor bar geometry, 2D modelling cannot show all the causes of elevated electrical and thermal stresses at high frequencies. Using 3D modelling of the motor coil insulation system with anisotropic properties of the materials is crucial for electrical and thermal stress analyses and for the purposes of optimization with high-frequency applications.

The developed capacitive SG system based on floating conductive foil embedded in the groundwall is a promising solution for PWM-VSI drive fed motors. Based on the simulation and experimental test results, this SG system performs well with both power frequency and repetitive fast pulses. The performance of the system is independent of frequency and therefore can provide the required mitigation of the stress caused by repetitive fast pulses. This technique has the advantage of being unaffected by the variability in the conductivity of the SGT that occurs during both the manufacturing process and motor operation.

With respect to the qualification test, the developed capacitive SG system not only passed all test-pass criteria recommended by IEC/TS 60034-18-42, but also tolerated even more severe stresses. It is therefore concluded that the developed capacitive SG system can be an alternative that will perform better than conventional SG systems for the form-wound coils of inverter fed motors.

5.2 Suggestions for Future Work

The measurement of the electric field along the end portion of form-wound coils is crucial for evaluating the performance of an SG system in a variety of conditions. It was shown that various techniques can be adopted in order to obtain the electric field profile along an SG system. In this research, an electrostatic voltmeter was used to measure surface potential at 60 Hz and electric field was computed from the gradient of the potential. However, while an electrostatic voltmeter is suitable for dc and low frequency applications, it has limited accuracy with respect to

measuring the potential in an area with a very high divergent electric field. The application of other methods of measuring a high divergent field at high frequencies could be studied.

The dielectric properties of the SG materials depend strongly on the electric field, the frequency, and the temperature. In this study, the materials were characterized at both low and high electric field and at both dc and ac with low and high frequencies. Characterizing the materials under repetitive fast pulses is another topic for future research.

Computation of coupled electric and thermal fields on the SG systems under repetitive fast pulses is still a challenge. The method used in this study was to apply two equivalent high-frequency voltages and to simulate the system using two static coupled electro-thermal finite element analyses. Developing a focused study in this area using other techniques, such as an iterative quasi-static technique, for the thermal analysis of an SG system under repetitive fast pulses is suggested.

Using 2D- and 3D-FEM simulation and also through experimental testing, it was shown that the geometry and manufacturing of the bars can strongly influence the electrical and thermal stress that develops on the SG system under fast pulses. Similar studies could be extended for the actual coil geometry, the stator slot, the tape lapping, the clamping fingers, and the cross interference from other phases. Additional work could include an examination of the effects of force air cooling, pollution and moisture, and the resin in global VPI motors on the development of stress in the stator slots and endwinding.

The tape lapping can have a negative impact on the performance of the CAT and SGT at high frequencies. In this study, the CAT was applied in a half-lapped configuration, which makes it likely that gaps filled with resin will form between the laps. These resin-filled gaps and the overlap contact resistance can be a secondary mechanism for conduction and development of stress. The application of other tape lapping configurations such as 2/3 lapped, or the application of paint as conductive armour or as SG coating could be studied with respect to inverter fed motor coils.

Optimization of additional parameters such as the coil corner radius, the slot clearance between the coil and the core, the geometry of the slots, the thermal class of the material, and the operating temperature, could mitigate electrical and thermal stress, particularly on the CAT at the slot exit and inside of the stator slot.

In addition, for conventional SG systems, the overlap between the CAT and the SGT could be increased. In other words, SGT could be applied from the slot exit to cover the whole length of

the CAT along the endwinding in a manner similar to that shown in Figure 5-1 (b). The simulation work conducted in this research indicated that this adjustment could significantly decrease the stress at the slot exit.

A combination of a conventional resistive SG system and the developed capacitive SG system could be studied. Two designs for this scheme are suggested in Figure 5-1. In these designs, highly conductive tape is used rather than aluminum foil within the groundwall insulation, and it is expected that these designs could mitigate significantly the thermal stress on the SGT. The conductive tape must be more conductive than the CAT that is used as the slot surface discharge protection. Using the highly conductive tape with similar construction to mica tape with glass fibre backing has some benefits over aluminum foil to eliminate any air gap that could be formed between the aluminum foil and the mica tape.

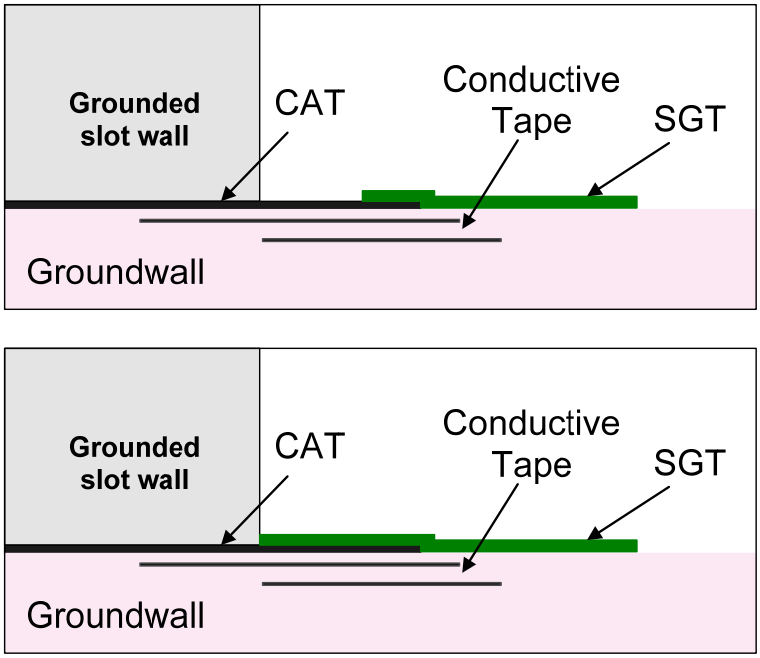

Figure 5-1: Two designs suggested for combining resistive and capacitive SG systems. Note that in (a) the SGT overlaps the end of the CAT while in (b) the SGT overlaps the CAT from the slot exit.

IEC/TS 60034-18-42 does not recommend a diagnostic test during qualification of the stress grading system subjected to repetitive fast pulses. However, PD measurement under pulse application is suggested to identify the source of PD and any surface discharges that develop during the test and may not be observed with a PD measurement at power frequency [146, 147].

This study, evaluated the performance of the developed capacitive SG system on 13.8 kV motor bar samples through short- and long-term tests, and it was shown that the developed SG system can be an alternative to the conventional SG system for the form-wound coils of inverter fed motors. However, the recommendation time (100 h) for performing the qualification test is not enough to age the insulation system. It is recommended to perform a long term multi-stress (elevated temperature with mechanical vibration) ageing test at pulse voltage to find the life curves. In addition, according to the acceptance test procedure recommended by IEC/TS 60034-18-42, complete 13.8 kV motor coils with actual dimensions and shapes and with all the insulation components and with the developed SG system must be evaluated with respect to long-term aging, or a voltage endurance test at 60 Hz.

The effects of a long-term aging test on the surface potential profile, the corresponding electric field profile, and the dc and ac dielectric properties of the CAT and the SGT could be investigated and compared with the results of prior aging tests.

References

[1] The NewsRoom, Natural Resources Canada's News Source, http://www.nrcan.gc.ca /media/ newsreleases/2004/200458a_e.htm.

[2] Ali Emadi, Energy-efficient Electric Motors, ISBN: 0-8247-5735-1, 2005.

[3] T. C. Huang and M. A. El-Sharkawi, "High Performance Speed and Position Tracking of Induction Motors Using Multi-Layer Fuzzy Control," IEEE Transactions on Energy Conversion, Vol. 11, No. 2, pp. 353 – 358, June 1996.

[4] Qualification and Acceptance Tests for Type II Electrical Insulation Systems used in Rotating Electrical Machines Fed from Voltage Converters, IEC/TC 60034-18-42, Ed. 1.0, 2008.

[5] G. C. Stone, E. A. Boulter, I. Culbert, and H. Dhirani, "Electrical Insulation for Rotating Machines," IEEE Press, 2004.

[6] S. Ul Haq, PhD thesis, "A Study on Insulation Problems in Drive Fed Medium Voltage Induction Motors," University of Waterloo, Waterloo, Ontario, Canada, 2007.

[7] R. H. Rehder, R. E. Draper, and B. J. Moore: "How Good is You Motor Insulation System?," IEEE Electrical Insulation Magazine, Vol. 12, No. 4, pp. 8-13, July/August 1996.

[8] IEEE Std 1-2000 IEEE Recommended Practice - General Principles for Temperature Limits in the Rating of Electrical Equipment and for the Evaluation of Electrical Insulation, December 2000.

[9] A. Bock, R. Joho, T. Baumann, and C-E. Stephan, "Trends in Insulation Systems for Generator HV-Windings," CIGRE Session, 11-102, 2002.

[10] T. Weege, "Basic Impregnation Techniques," Electrical Insulation Conference, and Electrical Manufacturing & Coil Winding Conference, pp. 709-715, September 1997.

[11] A. Roberts, "Stress Grading for High Voltage Motor and Generators Coils," IEEE Electrical Insulation Magazine, Vol. 11, Num. 4, pp. 26-31, 1995.

[12] D.J. Conley and N. Frost, "Fundamentals of Semi-Conductive Systems for High Voltage Stress Grading," IEEE Electrical Insulation Conference and Electrical Manufacturing Expo, October 2005.

[13] M.K.W Stranges, G.C. Stone, and D.L. Bogh, "New Specs for ASD Motors," IEEE Industry Applications Magazine, Vol. 13, Issue 1, pp. 37-42, January-February 2007.

[14] F. P. Espino Cortés, PhD thesis, “A Study of Field-Dependent Stress Grading Systems Working under Fast Rise Time Pulses,” University of Waterloo, Waterloo, Ontario, Canada, 2006.

[15] F.T. Emery, “The Application of Conductive and Stress Grading Tapes to Vacuum Pressure Impregnated, High Voltage Stator Coils,” IEEE Electrical Insulation Magazine, Volume: 12, Issue: 4, pp. 15-22, July/August 1996.

[16] H. Brandes, T. Hillmer, M.R. Levit, W.E. Corbett, and N.E. Frost, "New Generation of Conductive Tapes for High Voltage Applications," IEEE International Symposium on Electrical Insulation (ISEI), pp. 376-379, June 2006.

[17] J.A. Allison, “Understanding the Need for Anti-Corona Materials in High Voltage Rotating Machines,” 6th IEEE International Conference on Properties and Applications of Dielectric Materials, June 2000.

[18] M.K.W. Stranges, J.E. Hayward, R. Omranipour, and J.H. Dymond, “Comparative Evaluation of Glass Conducting Armour Materials for Form-Wound Stator Coils,” IEEE International Symposium on Electrical Insulation, pp. 216- 221, September 2004.

[19] F. Senn, W. Ladstaetter, and W. Grubelnik, ”Challenges and Current Approaches in enhancing insulation systems for more efficient high voltage rotating machines,” Isovolta AG, A-8402 Werndorf, Austria, Presented in INSULEC, Bangalore India, 2009.

[20] V. Warren and G. Stone, “Recent Developments in Diagnostic Testing of Stator Windings,” IEEE Electrical Insulation Magazine, Vol. 14, No: 5, pp. 16-21, 24 Sep/Oct 1998.

[21] G. Jiang, J. Kuang, and S. Boggs, “Evaluation of High Field Conduction Models of Polymeric Dielectrics,” IEEE Conference on Electrical Insulation and Dielectric Phenomena (CEIDP), October 2000.

[22] S. Boggs and J.Y. Zhou, “Dielectric Property Measurement of Nonlinear Grading Materials,” IEEE Conference on Electrical Insulation and Dielectric Phenomena (CEIDP), pp. 764-767, October 2000.

[23] E. Kuffel, W.S. Zaengl, and J. Kuffle, “High Voltage Engineering Fundamentals,” Second Edition 2000, published by Butterworth-Heinemann.

[24] K. Kimura and S. Hirabayashi, "Improved Potential Grading Methods with Silicon Carbide Paints for High Voltage Coils," IEEE Transaction on Electrical Insulation, Vol. EI-20, No.3, pp.511-517, June 1985.

[25] L.L. Alston, "High-voltage technology," Oxford University Press 1968.

[26] R.A. Hanna and S.W. Randall, "Medium Voltage Adjustable-Speed Drive Retrofit of an Existing Eddy-Current Clutch Extruder Application," IEEE Transactions on Industry Applications, Vol. 36, pp. 1750-1755, November/December 2000.

[27] The Worldwide Market for Medium Voltage Motor Drives. Research Report # IMS3542, IMS Research Group, November 2005.

[28] R. H. Engelmann and W. H. Middendorf, Handbook of Electric Motors. Marcel and Dekker NY. 1995.

[29] Y. Shakweh, "MV Inverter Stack Topologies," IEE Power Engineering Journal, Vol. 15, pp 139-149, June 2001.

[30] Bin Wu, High-Power Converters and AC Drives. IEEE Press, John Wiley Publication, 2006.

[31] B.K. Bose, Modern Power Electronics and AC Drives. Upper Saddle River, NJ: Prentice Hall, 2002.

[32] R. Teodorescu, F. Blaabjerg, J.K. Pedersen, and E. Cengelci, "Multilevel Inverter by Cascading Industrial VSI," IEEE Transactions on Industrial Electronics, Vol. 49, pp. 832-838, August 2002.

[33] Y. Montasser and MSc Thesis, "Design and Development of a Power Modulator for Insulation Testing," University of Waterloo, Waterloo, Ontario, Canada, 2006.

[34] Lecture notes, ECE663 - Energy Processing, ECE Department, University of Waterloo, Canada, Spring 2007.

[35] N. Mohan, T.M. Underland, and W. Robbins, "Power Electronics, Converters, Applications, and Design," John Wiley and Sons, Inc. 2003.

[36] S. Ul Haq, Shesha H. Jayaram, and Edward A. Cherney "Insulation Problems in Medium Voltage Stator Coils under Fast Repetitive Voltage Pulses," 53rd IEEE Pulp and Paper Industry Technology Conference, June 2007.

[37] J.C.G. Wheeler, "Effects of Converter Pulses on the Electrical Insulation in Low and Medium Voltage Motors," IEEE Electrical Insulation Magazine, Vol. 21, No. 2, pp. 22 – 29, March/April 2005.

[38] S. Bell, et al., "Experience With Variable-Frequency Drives and Motor Bearing Reliability," IEEE Transactions on Industry Applications, Vol. 37, no. 5, pp. 1438-1446 September/ October 2001.

[39] Rotating Electrical Machines – Part 17: Cage Induction Motors when Fed from Converters – Application Guide, IEC/TS 60034-17, Ed. 4.0, 2006.

[40] Rotating Electrical Machines – Part 25: Guide for the Design and Performance of Cage Induction Motors Specifically Designed for Converter Supply, IEC/TS 60034-25, Ed. 1.0, 2004.

[41] A. Cavallini, D. Fabiani, G.C. Montanari, "Power Electronics and Electrical Insulation Systems - part 2: Life Modeling for Insulation Design," IEEE Electrical Insulation Magazine, Vol. 26, No. 4, pp.33-39, July-August 2010.

[42] M. T. Tsal, "Efficient Technique for Suppression of Motor Transient Voltage," IEEE Transaction on Aerospace and Electronic Systems, Vol. 39, No. 2, April 2003.

[43] A. V. Jouanne, D. A. Rendusara, P. N. Enjeti, and J. W. Gray, "Filtering Techniques to Minimize the Effect of Long Motor Leads on PWM Inverter-Fed AC Motor Drive Systems," IEEE Transaction on Industry Application, Vol. 32, No. 4, pp. 919–926, July/August 1996.

[44] E. Sharifi, "Over-voltage Transient on Motor Terminal Fed by PWM-Voltage Source Converter and Long Cable (Factors, Suppression Methods & Simulation)," Course project for ECE 663, University of Waterloo, Waterloo, Ontario, Canada, Spring 2007.

[45] S. Ul Haq, Shesha H. Jayaram, and Edward A. Cherney, "Evaluation of Medium Voltage Enamelled Wire Exposed to Fast Repetitive Voltage Pulses," IEEE Transactions on Dielectrics and Electrical Insulation, Vol. 14, No. 1, pp. 194-903, 2007.

[46] H. Zois, L. Apekis, and M. Omastova, "Electrical Properties and Percolation Phenomena in Carbon Black Filled Polymer Composites," International Symposium on Electrets (ISE), pp. 529-532, 1999.

[47] R. Strumpler and J. Glatz-Reichenbach, "Conducting polymer composites," Journal of Electroceramics, Vol. 3, No. 4, pp. 329-346, 1999.

[48] E. Martensson, B. Nettelbled, U. Gafvert, and L. Palmqvist, "Electrical Properties of Field Grading Materials with Silicon Carbide and Carbon Black," IEEE 6th International Conference on Conduction and Breakdown in Solid Dielectrics, pp. 548-552, June 1998.

[49] C. Onneby, E. Martensson, U. Gafvert, A. Gustafsson, and L. Palmqvist, "Electrical Properties of Field Grading Materials Influenced by the Silicon Carbide Grain Size," IEEE 7th International Conference on Solid Dielectrics, pp. 43-45, 2001.

[50] F. P. Espino-Cortes, S. Jayaram, and E.A. Cherney, “Stress Grading Materials for Cable Terminations under Fast Rise Time Pulses” IEEE Transaction on Dielectric and Electrical Insulation, Vol. 13, No. 2, pp. 430 – 435, April 2006.

[51] F. P. Espino-Cortes, E.A. Cherney, and S. Jayaram, “Impact of Inverter Drives Employing Fast-Switching Devices on Form-Wound AC Machine Stator Coil Stress Grading,” IEEE Electrical Insulation Magazine, Vol. 23, No. 1, pp. 16-28 January-February 2007.

[52] N. Taylor, “Diagnostics of Stator Insulation by Dielectric Response and Variable Frequency Partial Discharge Measurements,” Licentiate Thesis, KTH University, Stockholm, Sweden 2006.

[53] J. Rivenc, T. Lebey, A. Loubiere, M. Biron, and J. Warnant, “A Discussion of Current-Voltage and Surface Potential Measurements to Test Stress Grading Materials,” Journal of Physics D: Applied Physics, Vol. 31, pp. 2612-2621, October 1998.

[54] X. Qi, Z. Zheng, and S. Boggs, “Engineering with Nonlinear Dielectrics,” IEEE Electrical Insulation Magazine, Vol. 20, No. 6, pp. 27-34, 2004.

[55] S. H. Hagen, “The Conduction Mechanism in Silicon Carbide Voltage-Dependent Resistors,” Philips Research Reports, Vol. 26, pp. 486-518, 1971.

[56] E. Martensson, U. Gäfvert, and C. Önneby, “Alternate Current Characteristics of SiC Powders,” Journal of Applied Physics, Vol. 90, No 6, pp. 2870-2878, 2001.

[57] L. S. Schadler, X. Wang, J. K. Nelson and H. Hillborg, “Non-linear Field Grading Materials and Carbon Nanotube Nanocomposites with Controlled Conductivity,” Chapter 9, Dielectric Polymer Nanocomposites, Springer US, pp. 259-284, 2010.

[58] L. S. Schadler, X. Wang, J. K. Nelson and H. Hillborg, “Non-linear Field Grading Materials and Carbon Nanotube Nanocomposites with Controlled Conductivity,” Chapter 9, Dielectric Polymer Nanocomposites, Springer US, pp. 259-284, 2010.

[59] Eva Martensson, “Modelling Electrical Properties of Composite Materials,” PhD Thesis, KTH University, Stockholm, Sweden, 2003.

[60] R. Strumpler , J. Rhyner , F. Greuter, and P. Kluge-Weiss, “Nonlinear Dielectric Composites,” Smart Materials and Structures Magazine, Vol. 4, No. 3, pp. 215- 222, 1995.

[61] B.R. Varlow, K. Li, "Non-linear AC Properties of Filled Resins," IEE Proceedings on Science, Measurement, and Technology, Vol. 150, No.2, pp. 75- 82, March 2003.

[62] J.C.G. Wheeler, A.M. Gully, A.E. Baker, and F.A. Perrot, "Thermal Performance of Stress Grading Systems for Converter-Fed Motors," IEEE Electrical Insulation Magazine, Vol.23, No.2, pp.5-11, March-April 2007.

[63] G. Lupo, C. Petrarca, L. Egiziano, V. Tucci, and M. Vitelli, "Numerical Evaluation of the Electric Field in Cable Terminations Equipped with Nonlinear Grading Materials," IEEE Conference on Electrical Insulation and Dielectric Phenomena, pp. 585-588, October 1998.

[64] B.S. Nindra and A. Khazanov, "Semi-Conducting Corona Suppression System for High Voltage Windings," Iris Rotating Machine Conference, San Antonio, TX, pp. 1-8, June 2002.

[65] J.Y. Zhou and S. Boggs, "Dielectric Properties of Three Component Mixtures of Nonlinear, Resistive, and Non-Conducting Grains," IEEE Conference on Electrical Insulation and Dielectric Phenomena, pp. 112- 115, October 2003.

[66] J. Speck, S. Grobmann, and F. Kielmann, "Behaviour of the Stress Grading System in Converter Operated H.V. Machines," XVth International Symposium on High Voltage Engineering. (ISH), T3-116, August 2007.

[67] K. P. Donnelly and B. R. Varlow, "Nonlinear dc and ac conductivity in electrically insulating composites," IEEE Transactions on Dielectrics and Electrical Insulation, Vol. 10, No. 4, pp. 610- 614, August 2003.

[68] T. Okamoto, I. Yoshiyuki, M. Kawahara, T. Yamada, and S. Nakamura, "Development of Potential Grading Layer for High Voltage Rotating Machine," IEEE International Symposium on Electrical Insulation, pp. 210- 215, September 2004.

[69] G. Jiang, J. Rhyner, J. Oesterheld, R. Strumpler, and S. Boggs, "Measurement of Non-Linear Dielectric Properties - Theoretical Analysis," IEEE Conference on Electrical Insulation and Dielectric Phenomena (CEIDP), pp.206-209, October 1997.

[70] T. Tokoro, K. Tohyama, M. Nagao, and M. Kosaki, "High-Field Dielectric Properties of Polyethylene in the High-Temperature Region," Electrical Engineering in Japan, Vol. 112, No. 6, pp. 10–19, 1992.

[71] T. Tokoro, K. Tohyama, M. Nagao, and M. Kosaki, "Evaluation of High-Field Dielectric Properties of Polymers with Superposition of AC and DC field," IEEE Conference on Conduction and Breakdown in Solid Dielectrics, pp.428-432, July 1995.

[72] V. Tucci and M. Vitelli, “On the Effect of Anisotropy in Nonlinear Composite Materials for Stress Grading Applications- A Numerical Study,” IEEE Transaction on Dielectrics and Electrical Insulation, Vol. 7, No. 3, pp. 378-393, June 2000.

[73] T.P. Hong, O. Lesaint, P. Gonon, and H. Debruyne, "Anisotropy of the Dielectric Properties of Laminated Epoxy Insulation Subjected to Water Absorption,” IEEE Conference on Electrical Insulation and Dielectric Phenomena (CEIDP), pp. 258- 261, October 2004.

[74] S. Nakamura, K. Saito, G. Sawa, and K. Kitagawa, “Percolation Threshold of Carbon Black-Polyethylene Composites,” Japanese Journal of Applied Physics, Vol. 36, Part 1, No. 8, pp. 5163-5168, 1997.

[75] R. Malamud, “Development, Calculation and Research of Semi-Conducting System for Capacitive Currents Routing in High Power Turbo-Generator High Voltage Air-Gap Armature Winding,” IEEE Electrical Insulation Conference and Electrical Manufacturing & Coil Winding Conference, Sep. 1997.

[76] M.K.W. Stranges, J.E. Hayward, J.H. Dymond, R. Omranipour, "A Comparative Evaluation of Various Conducting Slot Armour Materials,” IEEE Electrical Insulation Conference and Electrical Manufacturing & Coil Winding Technology Conference, pp. 599-604, September 2003.

[77] R. Brütsch and T. Hillmer, “Corona Protection in Rotating High Voltage Machines,” INDUCTICA Conference, 2006.

[78] M. Liese and M. Brown, "Design-Dependent Slot Discharge and Vibration Sparking on High Voltage Windings," IEEE Transactions on Dielectrics and Electrical Insulation, Vol. 15, No. 4, pp. 927-932, August 2008.

[79] G.C. Stone, C.V. Maughan, D. Nelson, and R.P. Schultz, "Impact of Slot Discharges and Vibration Sparking on Stator Winding Life in Large Generators," IEEE Electrical Insulation Magazine, Vol. 24, No. 5, pp. 14-21, September-October 2008.

[80] H. El-Kishky, R. Hebner, and M. Abdel-Salam, “Minimization of Local Field Enhancement Along Stress-Grading Systems of HV Large Rotating Machines,” IEEE Conference on Electrical Insulation and Dielectric Phenomena, October 2006.

[81] R. Malamud and I. Cheremisov; “Anti-Corona Protection of the High Voltage Stator Windings and Semi-Conductive Materials for its Realization” IEEE Electrical Insulation Conference (EIC), pp. 32-35, April 2000.

[82] L. Yingyan and X. Chuanxiang “Optimal Design on Anti-Corona Coating of High Voltage Generator Coil Ends,” IEEE International Conference on Properties and Applications of Dielectric Materials, 2000.

[83] V. Kogan, F. Dawson, G. Gao, and B. Nindra, "Surface Corona Suppression in High Voltage Stator Winding End Turns,” Electrical Electronics Insulation Conference and Electrical Manufacturing & Coil Winding Conference, pp. 411-415, September 1995.

[84] B. Marusic, "Efficiency Evaluation of the Semi-conductive Stress-Control Systems,” 7th BEAMA International Electrical Insulation Conference, pp. 56-60, 1994.

[85] H. El-Kishky, B. S. Nindra, M.A. Salam, and E. Williams, "Experience with Development and Evaluation of Corona-Suppression Systems for HV Rotating Machines," IEEE Transactions on Dielectrics and Electrical Insulation, Vol. 9, No. 4, pp. 569- 576, August 2002.

[86] S.U. Haq and R. Omranipour, “Comparative Evaluation of Various Grading Systems for Electric Machinery Stator Windings,” IEEE International Symposium on Electrical Insulation (ISEI), June 2010.

[87] J. C. G. Wheeler, A. M. Gully, A. E. Baker, and F. A. Perrot, “Novel Stress Grading Systems For Converter-Fed Motors” IEEE Electrical Insulation Magazine, Vol. 23, No. 1 pp. 29-35 January-February 2007.

[88] L. Ming, F. Salen, K. Johansson, E. Martensson, H. Eriksson, O. Koponen, and S. Paakkonen, “Effects of Repetitive Pulse Voltages on Surface Potential Distribution at End Corona Protection Region of High Voltage Motors,” 15th International Symposium on High Voltage Engineering (ISH 2007), T2-68, August 2007.

[89] R. Merte, “Measurement of Electric Fields with an Electro-Optic Miniature Probe,” 15th International Symposium on High Voltage Engineering (ISH 2007), T2-505, August 2007

[90] C. Staubach, S. Kempen, and F. Pohlmann, "Calculation of Electric Field Distribution and Temperature Profile of End Corona Protection Systems on Large Rotating Machines by Use of Finite Element Model,” IEEE International Symposium on Electrical Insulation (ISEI), pp. 1-6, June 2010.

[91] F. Long, J. Zhang, C. Xie, and Z. Yuan, "Application of the Pockels Effect to High Voltage Measurement,” International Conference on Electronic Measurement and Instruments, pp. 4-495-4-499, 2007.

[92] S. Kempen, F. Pohlmann, and K. Pinkert, “Comparison of Low-Interaction Methods of Measurement for Determining the Distribution of Surface Potential on End Corona Protection Configurations,” 11th International Conference on Electrical Insulation (INSUCON), May 2009.

[93] E. Sharifi, S. Jayaram and E. A. Cherney, “Temperature and Electric Field Dependence of Stress Grading on Form-wound Motor Coils,” IEEE Transaction on Dielectric and Electrical Insulation, Vol. 17, No. 1, pp. 264-270, February 2010.

[94] R.J. Jackson and A. Wilson, "Slot-Discharge Activity in Air-Cooled Motors and Generators,” IEE Proceedings- Electric Power Applications, Vol. 129, No. 3, pp. 159-167, May 1982.

[95] A. Basu, "Prevention of Slot Discharge and On-Line Condition Monitoring of High Voltage Machine Insulation,” Electrical Electronics Insulation Conference, EEIC/ICWA Exposition., pp. 305-309, September 1989.

[96] S. M. Cargill and D. G. Edwards, “Corona Screen Effectiveness in Large Machines under high Voltage, High Frequency Transient conditions,” IEE Proceedings- Electric Power Applications, Vol. 145, No. 5, pp. 469-474, September 1998.

[97] G.C. Stone, M. Sasic, D. Dunn, and I. Culbert, "Recent Problems Experienced with Motor and Generator Windings,” IEEE Industry Applications Society- Petroleum and Chemical Industry Conference, pp. 1-9, September 2009.

[98] R.H. Rehder, "Preliminary Evaluation of Motor Insulation for Variable Speed Applications,” Electrical Electronics Insulation Conference and Electrical Manufacturing & Coil Winding Conference, EEIC/ICWA Exposition, pp. 333-336, October 1993.

[99] A. Seki, S. Miyamoto, A. Okitani, Y. Ohki, S. Sakuma, S. Fukuyama, and H. Miyauchi, "Insulation Characteristics of XLPE Cables and Their Accessories for High Frequency Voltage with PWM Inverter,” IEEE Power Engineering Society- Transmission and Distribution Conference, pp. 560-566, April 1994.

[100] J.A. Oliver and G.C. Stone, “Implications for the Application of Adjustable Speed Drive Electronics to Motor Stator Winding Insulation,” IEEE Electrical Insulation Magazine, Vol. 11, No. 4, pp. 32-36, July-August 1995.

[101] A.E. Baker, A.M. Gully, G.J. Malkin, and J.C.G. Wheeler, “Insulation Systems for Inverter Fed Motors,” 9th International Conference on Electrical Insulation (INSUCON), pp. 143–147, June 2002.

[102] J.C. G. Wheeler and F.A. Perror, “Evaluation of a Novel Stress Grading System for Converter-Fed Motors,” 10th International Conference on Electrical Insulation (INSUCON), pp. 93-98, May 2006.

[103] F.P. Espino-Cortes, E.A. Cherney, and S. Jayaram, "Effectiveness of Stress Grading Coatings on Form Wound Stator Coil Groundwall Insulation Under Fast Rise Time Pulse Voltages,” IEEE Transactions on Energy Conversion, Vol. 20, No. 4, pp. 844- 851, December 2005.

[104] L. Ming, E. Martensson, F. Salen, K. Johansson, H. Eriksson, O. Koponen, and S. Paakkonen, “Effects of Repetitive Voltages on Surface Temperature Increase at End corona Protection Region of High Voltage Motors,” 10th International Conference on Electrical Insulation (INSUCON), pp. 105–108, May 2006.

[105] L. Ming, F. Sahlen, K. Johansson, E. Martensson, and O. Koponen, “Investigations on End Corona Protection System for Converter-fed HV Motors,” 11th International Conference on Electrical Insulation (INSUCON), 2009.

[106] W. Chen, G. Gao, and C. A. Mouton, “Stator Insulation System Evaluation and Improvements for Medium Voltage Adjustable Speed Drive Applications,” IEEE Petroleum and Chemical Industry Technical Conference (PCIC), pp. 241–248, September 2008.

[107] A. E. Baker, A.M. Gully, and J.C.G. Wheeler, “Finite Element Modeling of Nonlinear Stress Grading Materials for Machine End-Windings” IEEE Conference on Power Electronics, Machines and Drives, June 2002.

[108] H. El-Kishky, M. Abdel-Salam, H. Wedaa, and Y. Sayed, “Time-Domain Analysis of Nonlinear Stress-Grading Systems for High Voltage Rotating Machines” IEEE Conference on Electrical Insulation and Dielectric Phenomena, pp. 482- 485, October 2003.

[109] H. El-Kishky, A. El-Said, and F. Brown, "Performance of Non-Linear Stress-Grading Systems at Non-Sinusoidal Voltages,” IEEE International Power Modulators and High Voltage Conference, pp. 307-310, May 2008.

[110] H. El-Kishky, A. El-Said, and F. Brown, "High Frequency Performance of Nonlinear Stress Grading Systems,” IEEE International Power Modulators and High Voltage Conference, pp. 584-587, May 2008.

[111] Z. Zheng and S. A. Boggs, “Efficient Solution of Transient Nonlinear Field Problems,” IEEE Conference on Electrical Insulation and Dielectric Phenomena (CEIDP), pp. 130-133, 2002.

[112] E. Gockenbach, “Review of Material Advances for High Voltage Electrical Machines,” 9th International Electrical Insulation Conference, INSUCON 2002, pp. 203-208, 2002.

[113] Standard Test Methods for DC Resistance or Conductance of Insulating Materials, ASTM D257-07, 2007.

[114] Standard Test Method for D-C Resistance or Conductance of Moderately Conductive Materials, ASTM D4496-04e1, 2004.

[115] Q. Li, T. Zhao, W.H. Siew, "Definition and Digital Algorithms of Dielectric Loss Factor for Condition Monitoring of High-Voltage Power Equipment with Harmonics Emphasis," IEE Proceedings Generation, Transmission and Distribution, Vol. 152, No.3, pp. 309- 312, 2005.

[116] E. Sharifi, S. Jayaram and E. A. Cherney, “AC Modeling and Anisotropic Dielectric Properties of Stress Grading of Form-wound Motor Coils,” IEEE Transaction on Dielectrics and Electrical Insulation, Vol. 17, No. 3, pp. 694 – 700, June 2010.

[117] E. Sharifi, E. A. Cherney and S. H. Jayaram, “Anisotropic Dielectric Properties of Stress Grading Materials in Medium Voltage Form-Wound Motor Coils to Study Thermal Effects of Repetitive Fast Pulses,” IEEE Electrical Insulation Conference (EIC), pp 333-337, Canada, June 2009.

[118] S. Banerjee and S. H. Jayaram, “Thermal Effects of High-Frequency Voltage on Medium Voltage Cable Terminations,” IEEE Inter. Conf. Solid Dielectr., pp 669-672, 2007.

[119] Standard Test Method for Thermal Transmission Properties of Thermally Conductive Electrical Insulation Materials, ASTM D5470, 2006.

[120] J. Culham, P. Teertstra, A. Savija, M. Yovanovich, “Design, Assembly and Commissioning of a Test Apparatus for Characterizing Thermal Interface Materials,” 8th Conf. on Thermal and Thermomechanical Phen. in Electronic Systems, San Diego, CA, pp. 128-135, 2002.

[121] E. Sharifi, S. Jayaram and E. A. Cherney, “Capacitive Grading of 13.8 kV Form-Wound Motor Coil Ends for Pulse Width Modulated Drive Operation,” IEEE International Symposium on Electrical Insulation (ISEI), pp. 632-635, 2008.

[122] Maciej A. Noras, “Non-contact Surface Charge/Voltage Measurements Field-meter and Voltmeter Methods,” Trek Application Note, Number 3002.

[123] Operator's Manual, Treck Model 341A, electrostatic voltmeter.

[124] ThermaCAM^{TM} SC500, Operator's Manual, FLIR Systems.

[125] M.K.W. Stranges, G.C.Stone, D.L. Bogh, "Progress on IEC 60034-18-42 for Qualification of Stator Insulation for Medium-Voltage Inverter Duty Applications," IEEE Petroleum and Chemical Industry Technical Conference, PCIC '07, pp. 1-7, 2007.

[126] PowerModTH HVPM 30kV-30A, Operating Manual, Diversified Technologies, Inc., 2006.

[127] Y. Shakweh, "Power Devices for Medium Voltage PWM Converters," Power Engineering Journal, pp. 297-307, Vol. 13, No. 6, December 1999.

[128] IEC/TS 60034-18-41, "Rotating electrical machines - Part 18-41: Qualification and type tests for Type I electrical insulation systems used in rotating electrical machines fed from voltage converters," First edition, 2006-10.

[129] M.K.W. Stranges, G.C. Stone, D.L. Bogh, "IEC 60034-18-41: A new Draft Technical Specification for Qualification and Acceptance Tests of Inverter Duty Motor Insulation," Petroleum and Chemical Industry Conference, pp. 297- 302, September 2005.

[130] High-Voltage Test Techniques - Partial Discharge Measurements, IEC 60270, Ed. 3.0, 2000.

[131] Standard Test Method for Detection and Measurement of Partial Discharge (Corona) Pulses in Evaluation of Insulation Systems, ASTM D1868, 2007.

[132] Rotating Electrical Machines- Part 27: Off-line Partial Discharge Measurements On the Stator Winding Insulation of Rotating Electrical Machines, IEC/TS 60034-27, Ed. 1.0 2006.

[133] A.J.M. Pemen, "Detection of Partial Discharges in Stator Windings of Turbine Generators," PhD Thesis, Eindhoven University of Technology, Netherland, 2000.

[134] K. Kimura, "Progress of Insulation Aging and Diagnostics of High Voltage Rotating Machine Windings in Japan," IEEE Electrical Insulation Magazine, Vol.9, No.3, pp.13-20, May-June 1993.

[135] IEEE Trial-Use Guide to the Measurement of Partial Discharges in Rotating Machinery, IEEE Std. 1434, 2000.

[136] M. Pompili, C. Mazzetti, and R. Bartnikas, "Partial Discharge Inception Voltage Measurements in Dielectric Liquids," IEEE International Conference on Dielectric Liquids (ICDL), pp. 1-4, July 2008.

[137] M. Clark, et al., “Changing Insulation Systems - Benefits and Problems,” IEEE International Symposium on Electrical Insulation (ISEI), pp. 148-156, April 2000.

[138] L. Engiziano, V. Tucci, C. Petrarca, and M. Vittelli, “A Galerkin Model to Study the Field Distribution in Electrical Components Employing Nonlinear Stress Grading Materials,” IEEE Transactions on Dielectrics and Electrical Insulation, Vol. 6 , No. 6 , pp 765-773, 1999.

[139] User’s Guide, COMSOL® Multiphysics 3.5.

[140] B. Sonerud, T. Bengtsson, J. Blennow, and S. M. Gubanski, “Dielectric Heating in Insulating Materials Subjected to Voltage Waveforms with High Harmonic Content,” IEEE Transactions on Dielectrics and Electrical Insulation, Vol. 16, pp. 926-933, 2009.

[141] B. P. Lathi, Signal Processing and Linear Systems, Oxford University Press, 2001.

[142] E. Sharifi, S. H. Jayaram, and E. A. Cherney, “Analysis of Thermal Stresses in Medium Voltage Motor Coils under Repetitive Fast Pulses,” IEEE Conference on Electrical Insulation and Dielectric Phenomena (CEIDP), pp 339-342, 2009.

[143] Y.T. Yu, S.H. Jayaram, “Form Wound Stator Insulation System under Different Voltage Waveform Stresses,” IEEE Electrical Insulation Conference (EIC), pp. 425-429, June 2009.

[144] E. Sharifi, S. Jayaram and E. A. Cherney, “Analysis of Thermal Stresses in Medium-Voltage Motor Coils under Repetitive Fast Pulse and High-Frequency Voltages,” IEEE Transactions on Dielectrics and Electrical Insulation, Vol. 17, No. 5, pp. 1378-1384, October 2010.

[145] S.A. Boggs, “Theory of a Field-Limiting Dielectric,” IEEE Transactions on Power Delivery, Vol. 9, No. 3, pp. 1391-1397, July 1994.

[146] Electrical Insulating Materials and Systems – Electrical Measurement of Partial Discharges (PD) under Short Rise Time and Repetitive Voltage Impulses, IEC/TS 61934, Ed. 1.0, 2006.

[147] A. Cavallini, D. Fabiani, G.C. Montanari, "Power Electronics and Electrical Insulation Systems - part 3: Diagnostic Properties," IEEE Electrical Insulation Magazine, Vol. 26, No. 5, pp.30-40, September-October 2010.

[148] John R. Taylor, An Introduction to Error Analysis: The Study of Uncertainties in Physical Measurements, University Science Books, 1999.

Appendix A: Derivation of the Qualification Test Voltage

Figure A-1 illustrates a schematic diagram of a pulse width modulated (PWM), three-phase, voltage source, switch-mode inverter (VSI). Based on the inverter configuration, the voltage between each phase and the inverter common point (N) and the voltage between two phases are shown in Figure A-2.

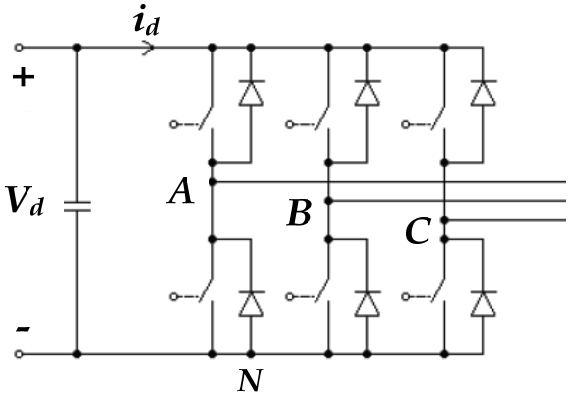

Figure A-1: Schematic diagram of a three-phase, PWM voltage source inverter (PWM-VSI).

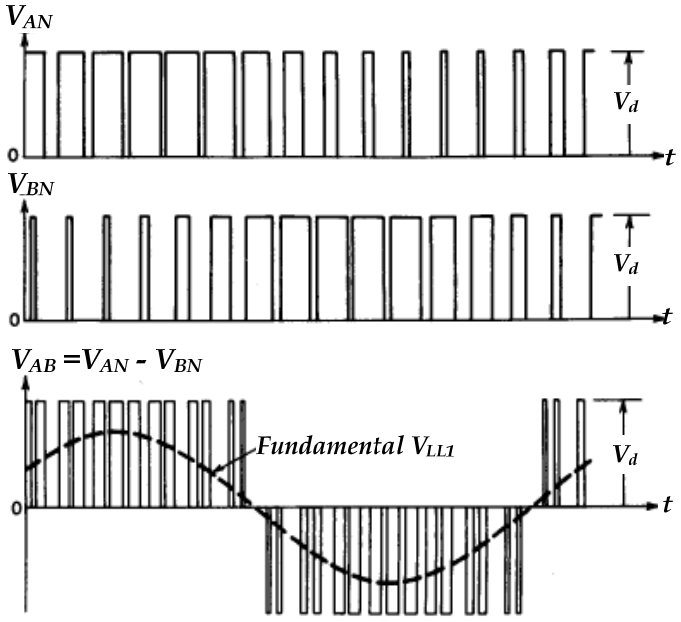

Figure A-2: The voltage waveform of a typical three-level PWM-VSI [35].

When this inverter supplies a three-phase load, such as a three-phase induction motor shown in Figure A-3, the phase-to-phase voltage at the output of the inverter is exactly identical to the phase-to-phase voltage at the terminal of the motor.

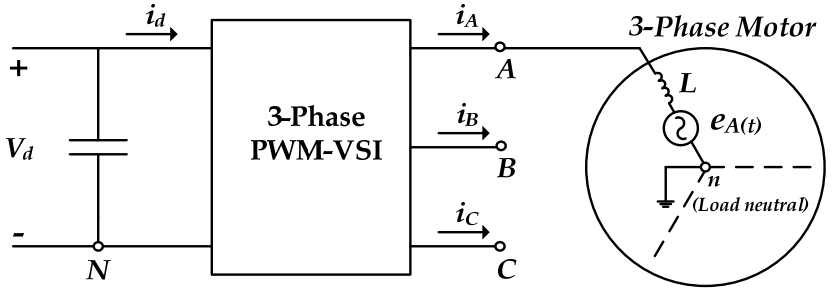

Figure A-3: Circuit diagram of a 3-phase PWM-VSI that supplies a 3-phase motor [35].

Since the inverter common point is generally isolated from the load star-point or load neutral (n), which is normally grounded, the phase-to-ground voltages of the motor (v_{An}, v_{Bn}, v_{Cn}) or the voltage across the insulation system can be calculated as follows [35]:

By Kirchloff's voltage law,

$$\begin{cases} v_{AN} = v_{An} + v_{nN} \\ v_{BN} = v_{Bn} + v_{nN} \\ v_{CN} = v_{Cn} + v_{nN} \end{cases} \Rightarrow \left(v_{AN} + v_{BN} + v_{CN}\right) = \left(v_{An} + v_{Bn} + v_{Cn}\right) + 3v_{nN}$$

but, $\left(i_A + i_B + i_C\right) = 0 \Rightarrow \left(v_{An} + v_{Bn} + v_{Cn}\right) = 0$

$$\therefore v_{nN} = \frac{\left(v_{AN} + v_{BN} + v_{CN}\right)}{3} \text{ and } \begin{cases} v_{An} = v_{AN} - v_{nN} = \frac{2}{3}v_{AN} - \frac{1}{3}\left(v_{BN} + v_{CN}\right) \\ v_{Bn} = v_{BN} - v_{nN} = \frac{2}{3}v_{BN} - \frac{1}{3}\left(v_{AN} + v_{CN}\right) \\ v_{Cn} = v_{CN} - v_{nN} = \frac{2}{3}v_{CN} - \frac{1}{3}\left(v_{AN} + v_{BN}\right) \end{cases} \quad \textbf{(A-1)}$$

With respect to Figure A-2 and according to (A-1), the voltage between each phase and the ground, such as V_{An}, can be extracted as shown in Figure A-4 (a). Equation (A-1) is independent of the waveform of the phase-to-phase voltage in a balance three-phase system. Figure A-4 (b) shows the phase-to-ground voltage of a three-phase balanced load supplied by a square wave VSI. Both PWM and square wave inverters have identical magnitude of the fundamental-frequency component of phase-to-ground voltage, which requires a higher dc voltage level (V_d) in the PWM operation [35].

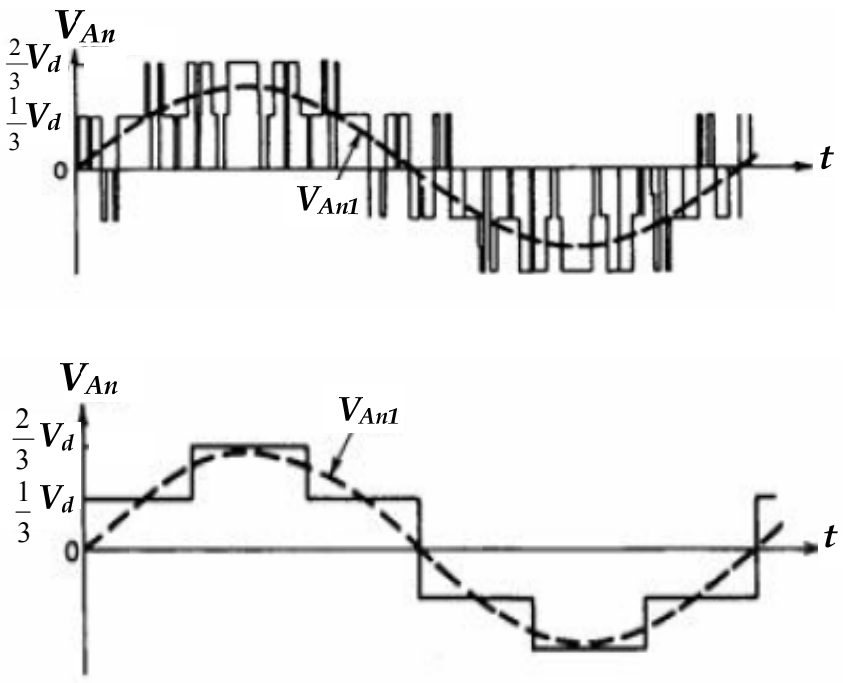

Figure A-4: Phase-to-ground voltage at a three-phase motor supplied from (a) a PWM-VSI and (b) a square wave VSI [35].

The fundamental-frequency component of the PWM-VSI in the output voltage (V_{AN1}) varies linearly with the amplitude modulation ratio (m_d), and if the switching harmonics are ignored, the fundamental-frequency component of the phase-to-ground voltage of the load (V_{An1}) is almost equal to (V_{AN1}) as (A-2) [34].

$$V_{AN1} = m_a . \frac{V_d}{2} \approx V_{An1} \qquad \text{(A- 2)}$$

For a 13.8 kV motor, $V_{An1} \approx 11.26 kV$; if $m_a = 1$, the magnitude of the dc link voltage is $V_d \approx 22.5 kV$. With respect to Figure A-4, it is therefore concluded that the peak of the phase-to-ground voltage ($V_{An\text{-}peak}$) for a 13.8 kV PWM-VSI is about 15 kV ($=2/3\ V_d$) and the peak-to-peak value is 30 kV. In this calculation, pulse waveform is assumed to be perfect with no overshoot. However, the actual pulses at the motor terminal have overshoots that can be taken into account in the previous calculation.

Appendix B: Thermal Stress at the Corner Edge

Figure B-1 (a, b) shows a cross-section of one of the samples used in this study.

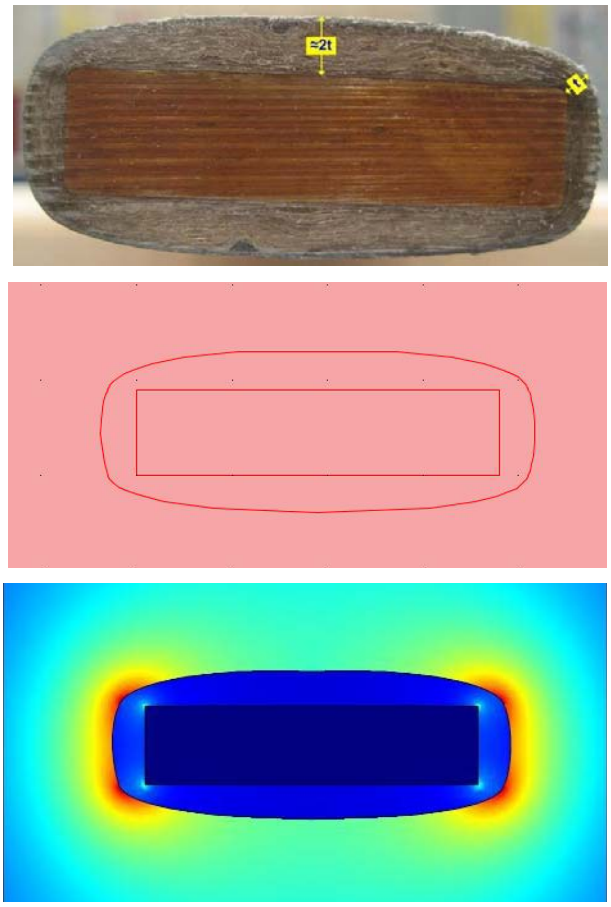

(a)

(b)

(c)

Figure B-1: (a) A cross-section of the samples with the conventional SG used in this study; (b) the geometry of the cross-section developed in COMSOL® Multiphysics; (c) the electric field distribution.

In the samples, copper bars with rectangular cross-section were used as the main conductor. With this geometry, the insulation thickness decreases from the middle of the bar toward the edges. Using finite element simulation, the electric field profile is shown Figure B-1 (c). It is evident that the electric field is concentrated at the edges. It must be noted that for actual form-wound motor coils, current-carrying conductors are in the form of strands, and the electric field distribution is therefore expected to be different from that shown in Figure B-1 (c).

Appendix C: Experimental Errors

Experimental errors are always in the nature of scientific measurement that uncertainties are associated with every quantitative result. This may because of inherent limitations in the measuring equipment, or of the measuring techniques, or perhaps the experience and skill of the experimenter. There are two types of errors associated with an experimental result: the "precision" and the "accuracy". In the fields of science, engineering, industry and statistics, the accuracy of a measurement system is the degree of closeness of measurements of a quantity to its actual (true) value. The precision of a measurement system, also called reproducibility or repeatability, is the degree to which repeated measurements under unchanged conditions show the same results [148]. In Table C-1, the accuracy of the main measuring equipment used in the experimental works is presented.

Table 0C-1: The accuracy of the measuring equipment used in experiments

Equipment	**Accuracy**
IR Camera, Flir SC 500	2% or ± 2 °C
Electrostatic voltmeter, TREK 341A	Better than ±0.1% of full scale
Electometer (Pico Ammeter), 6514 Keithley	@ 200 pA: ±(1 + 5) (%rdg+counts), 18-28°C @ 200 μA: ±(0.1 + 5) (%rdg+counts), 18-28°C
Oscilloscope, TDS 2024B, Tektronix	DC Vertical: ±3% Time Base: 50 ppm
Oscilloscope, WaveJet 312 LeCroy	DC Vertical: ± (1.5% + 0.5% of full scale) Time Base: 10 ppm

Appendix D: List of Publications

Papers in Refereed Journal

1. E. Sharifi, S. Jayaram and E. A. Cherney, "Analysis of Thermal Stresses in Medium-Voltage Motor Coils under Repetitive Fast Pulse and High-Frequency Voltages," IEEE Transactions on Dielectrics and Electrical Insulation, Vol. 17, No. 5, pp. 1378-1384, Oct. 2010.
2. E. Sharifi, S. Jayaram and E. A. Cherney, "AC Modeling and Anisotropic Dielectric Properties of Stress Grading of Form-wound Motor Coils," IEEE Transaction on Dielectric and Electrical Insulation, Vol. 17, No. 3, pp. 694 – 700, Jun. 2010.
3. E. Sharifi, S. Jayaram and E. A. Cherney, "Temperature and Electric Field Dependence of Stress Grading on Form-wound Motor Coils," IEEE Transaction on Dielectric and Electrical Insulation, Vol. 17, No. 1, pp. 264-270, Feb. 2010.

Papers in Refereed Conferences

1. E. Sharifi, S. Jayaram, E. A. Cherney, S. Ul Haq, and R. Omranipour, "IEC Qualification Test applied to Capacitively Graded 13.8 kV Motor Coils Energized with Repetitive Fast Pulses," Accepted for IEEE Electrical Insulation Conference (EIC), Annapolis, MD, USA, Jun. 2011.
2. E. Sharifi, S. Jayaram and E. A. Cherney, "A Study of Stress Grading of MV Motor Coils Energized by Repetitive Fast Pulses," Power System Conference (PSC), No. 10-E-ELM-2267, Tehran, Iran, Nov. 2010.
3. E. Sharifi, S. Jayaram and E. A. Cherney, "A Coupled Electro-thermal Study of the Stress Grading System of Medium Voltage Motor Coils when Energized by Repetitive Fast Pulses," IEEE International Symposium on Electrical Insulation (ISEI), pp. 1-4, San Diego, CA, USA, June 2010.
4. E. Sharifi, S. Jayaram and E. A. Cherney, "Analysis of Thermal Stresses in Medium Voltage Motor Coils under Repetitive Fast Pulses," IEEE Conference on Electrical Insulation and Dielectric Phenomena (CEIDP), pp 339-342, Virginia Beach, USA, Oct. 2009.
5. E. Sharifi, E. A. Cherney and S. H. Jayaram, "Anisotropic Dielectric Properties of Stress Grading Materials in Medium Voltage Form-Wound Motor Coils to Study Thermal

Effects of Repetitive Fast Pulses," IEEE Electrical Insulation Conference (EIC), pp 333-337, Montreal, Canada, Jun. 2009.

6. E. Sharifi, S. Jayaram and E. A. Cherney, "Capacitive Grading of 13.8 kV Form-Wound Motor Coil Ends for Pulse Width Modulated Drive Operation," IEEE International Symposium on Electrical Insulation (ISEI), pp. 632-635, Vancouver, Canada, Jun. 2008.
7. E. Sharifi, E. A. Cherney and S. Jayaram, "Grading of Electric Field in Medium Voltage Motors Using Embedded Metallic Foils in Stator Ground-Wall Insulation," COMSOL Conference, Boston, USA, Oct. 2007.

Non-refereed Presentations

1. E. Sharifi, "Analysis of Electrical and Thermal Stresses in Stress-Relief-System of Inverter Fed Medium Voltage Induction Motors," Presented at General Electric Peterborough, ON, Canada, December, 2010.
2. E. Sharifi, "Analysis of Electrical and Thermal Stresses in Stress-Relief-System of Inverter Fed Medium Voltage Induction Motors," PhD seminar, Department of Electrical and Computer Engineering, University of Waterloo, Waterloo, ON, November, 2010.
3. E. Sharifi, S. Jayaram, and E. A. Cherney, "DC and AC Modelling of Stress Grading System on Medium Voltage Motor Coils – a Case Study," CAGE Club Student Conference on High Voltage Engineering and Electrostatics, McMaster University, Hamilton, ON, August 2009.
4. E. Sharifi, "Electrical and Thermal Characterization of Materials Used in SG of Form-Wound Coils, Analysis of Conventional SG Grading by Transient FEM, and the Design and Verification of a Capacitive SG System," Presented at General Electric Peterborough, ON, Canada, October, 2008.
5. E. Sharifi, "Grading of Electric Field in MV Inverter-Fed Motors," Graduate Student Research Talks, Department of Electrical and Computer Engineering, University of Waterloo, Waterloo, ON, June 2008.
6. E. Sharifi, S. Jayaram and E. A. Cherney, "Stress Grading of Form-Wound Motor Coil Ends when Fed from Voltage Source Converters," CAGE Club Student Conference on High Voltage Engineering and Electrostatics, University of Waterloo, Waterloo, ON, August 2007.